

Max-Planck-Institut
für Physik komplexer Systeme



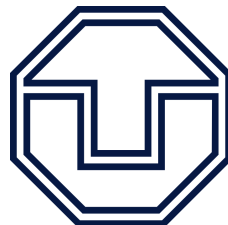
Hydrodynamics of flagellar swimming and synchronization

Dissertation
zur Erlangung der akademischen Grades
Doctor rerum naturalium

vorgelegt von
Gary Steven Klindt
Geboren am 13. Juni 1984 in Rottweil

Dresden, 2017

Institut für Theoretische Physik
Fakultät für Mathematik und Naturwissenschaften
Technische Universität Dresden





Abstract

What is flagellar swimming? Cilia and flagella are whip-like cell appendages that can exhibit regular bending waves. This active process emerges from the non-equilibrium dynamics of molecular motors distributed along the length of cilia and flagella. Eukaryotic cells can possess many cilia and flagella that beat in a coordinated fashion, thus transporting fluids, as in mammalian airways or the ventricular system inside the brain. Many unicellular organisms possess just one or two flagella, rendering them microswimmers that are propelled through fluids by the flagellar beat including sperm cells and the biflagellate green alga *Chlamydomonas*.

Objectives. In this thesis in theoretical biological physics, we seek to understand the nonlinear dynamics of flagellar swimming and synchronization. We investigate the flow fields induced by beating flagella and how in turn external hydrodynamic flows change speed and shape of the flagellar beat. This flagellar load-response is a prerequisite for flagellar synchronization. We want to find the physical principals underlying stable synchronization of the two flagella of *Chlamydomonas* cells.

Results. First, we employed realistic hydrodynamic simulations of flagellar swimming based on experimentally measured beat patterns. For this, we developed analysis tools to extract flagellar shapes from high-speed videoscropy data. Flow-signatures of flagellated swimmers are analysed and their effect on a neighboring swimmer is compared to the effect of active noise of the flagellar beat. We were able to estimate a chemo-mechanical energy efficiency of the flagellar beat and determine its waveform compliance by comparing findings from experiments, in which a clamped *Chlamydomonas* is exposed to external flow, to predictions from an effective theory that we designed. These mechanical properties have interesting consequences for the synchronization dynamics of *Chlamydomonas*, which are revealed by computer simulations. We propose that direct elastic coupling between the two flagella of *Chlamydomonas*, as suggested by recent experiments, in combination with waveform compliance is crucial to facilitate in-phase synchronization of the two flagella of *Chlamydomonas*.



List of publications

- Gary S. Klindt, Christian Ruloff, Christian Wagner, and Benjamin M. Friedrich. In-phase and anti-phase flagellar synchronization by basal coupling. arXiv, arXiv:1703.03355, 2017.
- Gary S. Klindt, Christian Ruloff, Christian Wagner, and Benjamin M. Friedrich. Load response of the flagellar beat. *Physical Review Letters*, 117:258101, Dec 2016.
- Gary S. Klindt and Benjamin M. Friedrich. Flagellar swimmers oscillate between pusher-and puller-type swimming. *Physical Review E*, 92(6):063019, 2015.
- Rui Ma, Gary S. Klindt, Ingmar H. Riedel-Kruse, Frank Jülicher, and Benjamin M. Friedrich. Active phase and amplitude fluctuations of flagellar beating. *Physical Review Letters*, 113(4):048101, 2014.



Acknowledgement

First of all, I want to thank Benjamin Friedrich for the versatile project and the opportunity to work with him. His somewhat unusual thinking trained my mind in unforeseen ways. I received continuous support from him, and he patiently took me back to the relevant scientific questions. I also want to thank him for an open and trustful relation. I thank Frank Jülicher for providing me with the opportunity to do my PhD at the Max-Planck institute and for allowing me to get to know such a rational and sharp communicator.

I am grateful for the very friendly and fruitful collaboration that we had with Christian Ruloff and Christian Wagner from the Saarland University. Christian Ruloff and I had a very direct exchange on our research. Christian Wagner invited me to a workshop in which we had very motivating discussions.

Of course, I am very thankful for all the physics as well as non-physics discussions I had with members of the Biological Physics group, specifically to the other PhD students. The discussions in the PhD-seminars were always helpful and sometimes even amusing. The most non-physics discussions I had with the “Einuhrgruppe” during lunch. Special thanks deserve (alphabetically) Samuel Krüger, Wolfram Pönisch, Christian Ruloff, André Scholich, Steffen Werner for proof-reading parts of this document.

I also want to thank the administration of the MPI-PKS for disburdening the scientific employees of the institute from bureaucratic obstacles, especially to the secretary of our Biological Physics Division Ulrike Burkert. The IT-department plays a special role at our institute, so thanks to its people as well. Special thanks are attributed to Hubert Scherrer-Paulus, who fixed all kinds of problems that occurred on the clusters within minutes. And thanks to Mike Richter, who fixed my laptop several times, when I had ruined my system.

I acknowledge the funding (grant number FR 3429/1-1) that I received from the DFG within the microswimmers priority program SPP 1726.

Finally, I want to thank my family for their support. It is calming, if there are places where you are unconditionally welcome, despite the fact of leaving. For their trust, love and believe I thank my siblings Robert Michael Klindt, Anke Maria Weiss, Thomas Jochan Weiss, Janine Charley Klindt, my mother Hildegard Klindt and my father Karl-Heinz Klindt.



Contents

1 — *Introduction*

1.1	Physics of cell motility: flagellated swimmers as model system	2
1.1.1	Tissue cells and unicellular eukaryotic organisms have cilia and flagella	2
1.1.2	The conserved architecture of flagella	3
1.1.3	Synchronization in collections of flagella	5
1.2	Hydrodynamics at the microscale	9
1.2.1	Navier-Stokes equation	10
1.2.2	The limit of low Reynolds number	10
1.2.3	Multipole expansion of flow fields	11
1.3	Self-propulsion by viscous forces	13
1.3.1	Self propulsion requires broken symmetries	13
1.3.2	Signatures of flowfields: pusher & puller	15
1.4	Overview of the thesis	16

2 — *Flow signatures of flagellar swimming*

2.1	Self-propulsion of flagellated swimmers	20
2.1.1	Representation of flagellar shapes	20
2.1.2	Computation of hydrodynamic friction forces	21
2.1.3	Material frame and rigid-body transformations	22
2.1.4	The grand friction matrix	23
2.1.5	Dynamics of swimming	23
2.2	The hydrodynamic far field: pusher and puller	26
2.2.1	The flow generated by a swimmer	26
2.2.2	Force dipole characterization	27
2.2.3	Flagellated swimmers alternate between pusher and puller	29
2.2.4	Implications for two interacting <i>Chlamydomonas</i> cells	31

2.3 Inertial screening of oscillatory flows	32
2.3.1 Convection and oscillatory acceleration	33
2.3.2 The oscilet: fundamental solution of unsteady flow	35
2.3.3 Screening length of oscillatory flows	35
2.4 Energetics of flagellar self-propulsion	36
2.4.1 Impact of inertial screening on hydrodynamic dissipation	37
2.4.2 Case study: the green alga <i>Chlamydomonas</i>	38
2.4.3 Discussion: evolutionary optimization and the number of molecular motors	38
2.5 Summary	39
3 — <i>The load-response of the flagellar beat</i>	
3.1 Experimental collaboration: flagellated swimmers exposed to flows	41
3.1.1 Description of the experimental setup	42
3.1.2 Computed flow profile in the micro-fluidic device	43
3.1.3 Image processing and flagellar tracking	43
3.1.4 Mode decomposition and limit-cycle reconstruction	47
3.1.5 Changes of limit-cycle dynamics: deformation, translation, acceleration	49
3.2 An effective theory of flagellar oscillations	50
3.2.1 A balance of generalized forces	50
3.2.2 Hydrodynamic friction in generalized coordinates	51
3.2.3 Intra-flagellar friction	52
3.2.4 Calibration of active flagellar driving forces	52
3.2.5 Stability of the limit cycle of the flagellar beat	53
3.2.6 Equations of motion	55
3.3 Comparison of theory and experiment	56
3.3.1 Flagellar mean curvature	57
3.3.2 Susceptibilities of phase speed and amplitude	57
3.3.3 Higher modes and stalling of the flagellar beat at high external load	59
3.3.4 Non-isochrony of flagellar oscillations	63
3.4 Summary	63
4 — <i>Flagellar load-response facilitates synchronization</i>	
4.1 Synchronization to external driving	65
4.2 Inter-flagellar synchronization in the green alga <i>Chlamydomonas</i>	67
4.2.1 Equations of motion for inter-flagellar synchronization	68
4.2.2 Synchronization strength for free-swimming and clamped cells	70
4.2.3 The synchronization strength depends on energy efficiency and waveform compliance	73

4.2.4 The case of an elastically clamped cell	74
4.2.5 Basal body coupling facilitates in-phase synchronization	75
4.2.6 Predictions for experiments	78
4.3 Summary	80
5 — <i>Active flagellar fluctuations</i>	
5.1 Effective description of flagellar oscillations	84
5.2 Measuring flagellar noise	84
5.2.1 Active phase fluctuations are much larger than thermal noise	84
5.2.2 Amplitude fluctuations are correlated	85
5.3 Active flagellar fluctuations result in noisy swimming paths	86
5.3.1 Effective diffusion of swimming circles of sperm cell	86
5.3.2 Comparison of the effect of noise and hydrodynamic interactions	87
5.4 Summary	88
6 — <i>Summary and outlook</i>	
6.1 Summary of our results	89
6.2 Outlook on future work	90
A — <i>Solving the Stokes equation</i>	
A.1 Multipole expansion	95
A.2 Resistive-force theory	96
A.3 Fast multipole boundary element method	97
B — <i>Linearized Navier-Stokes equation</i>	
B.1 Linearized Navier-Stokes equation	101
B.2 The case of an oscillating sphere	102
B.3 The small radius limit	103
B.4 Greens function	104
C — <i>Hydrodynamic friction</i>	
C.1 A passive particle	107

C.2 Multiple Particles	107
C.3 Generalized coordinates	108

D — *Data analysis methods*

D.1 Nematic filter	111
D.1.1 Nemat	111
D.1.2 Nematic correlation	111
D.2 Principal-component analysis	112
D.3 The quality of the limit-cycle projections of experimental data	113

E — *Adler equation*

F — *Sensitivity analysis for computational results*

F.1 The distance function of basal coupling	117
F.2 Computed synchronization strength for alternative waveform	118
F.3 Insensitivity of computed load-response to amplitude correlation time	118

List of Symbols

List of Figures

Bibliography

Introduction

*Motile cilia and flagella are hair-like cell organelles that perform a whip-like motion and are grown outward by many eukaryotic cells. Those hair-like structures are ubiquitous and evolutionary conserved structures. The continuum theory of fluids can be applied to understand the physics of cellular swimming in liquids, emergent synchronization of several cilia and flagella, as well as mechanical properties of the flagellar beat. The unicellular green alga *Chlamydomonas* allows us to study these phenomena in a single cell. *Chlamydomonas* lives in fresh water and has exactly two flagella that beat synchronously, which leads to straight swimming paths, despite of active fluctuations of the flagella. Since the size of *Chlamydomonas* and other microswimmers is at the scale of just tens of micrometers, inertia can be neglected, rendering hydrodynamic interactions to be virtually instantaneous. We review flagellar self-propulsion by viscous forces and its dependence on broken time-reversal symmetry.*

Chapter overview. First some systems that possess cilia and flagella are presented, specifically sperm cells and the green alga *Chlamydomonas* because they are the main actors of this thesis. The biological structure and function of flagella are discussed. Second, elements of fluid mechanics are presented. Third, some properties of swimming at the micro scale are exemplified. Last, the main questions that are addressed in this thesis are shown and the structure of the thesis is outlined.

1.1 Physics of cell motility: flagellated swimmers as model system

The flagellum is an active system whose motion emerges from the collective dynamics of thousands of microscopic constituents. Several cilia and flagella can synchronize, i.e. beat at a common frequency with fixed phase lag.

Section overview. First, biological systems that possess cilia and flagella and their functions are presented. Then, the molecular structure of flagella is presented and the onset of flagellar oscillations is explained. Last, biological examples with synchronizing cilia and flagella are shown and the theoretical basis for discussing synchronization of two oscillators is described.

1.1.1 Tissue cells and unicellular eukaryotic organisms have cilia and flagella

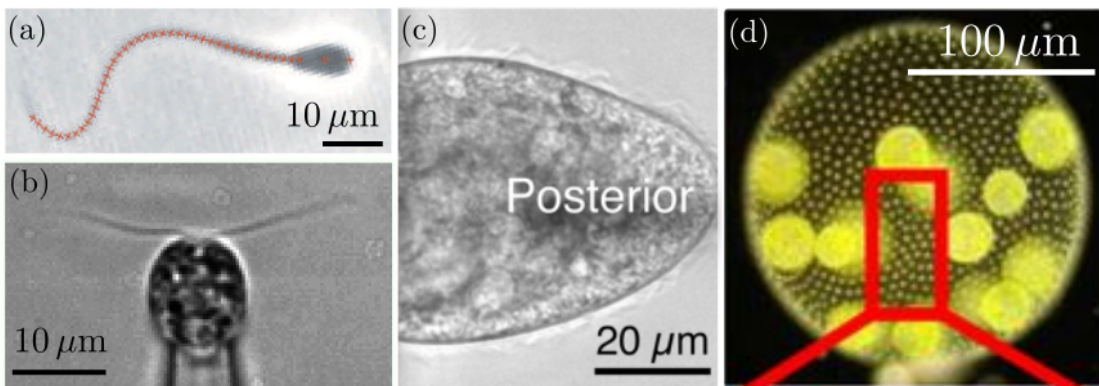


Figure 1.1: *Ciliated microswimmers.* (a) Sperm cell, image with modifications from [85] with permission. (b) *Chlamydomonas* cell, image recorded by Christian Ruloff. (c) The posterior part of a *Paramecium* cell, with modifications from [93], with permission. (d) *Volvox* organism, with modifications from [20].

Cells that possess cilia and flagella usually perform one of two features: self-propulsion and fluid pumping. Fluid pumping commonly happens due to cilia carpets on epithelial tissues that consist of many cells. Common examples of cilia carpets with about 50 cilia per cell in biological organisms are the cerebral ventricles inside the brain [102, 27, 115] and the airway found in many mammals [123]. A striking example is the ventral node of mouse embryos [19, 122] that contains primary whirling cilia whose beat break the left-right symmetry during vertebrate development. Another prevalent function of collections of cilia through fluid pumping is the increase in speed and sensitivity of sensing as at the olfactory sensory receptors in the nose of a Zebrafish embryo [106]. Biological model organisms for studying cilia carpets are the *paramecium* cell [93] and *Volvox* organism [20]. *Paramecium* is a single cell with hundreds of cilia and *Volvox* is

a green alga that consists of two types of cells, one of which form a shell structure and contain flagella on the outside, the other ones are germ cells, sitting in the interior. In the case of Paramecium and Volvox the cilia carpets function is not pumping fluid, but propelling the microswimmers through the fluid.

Usually, systems containing just a few cilia or flagella are self-propelling systems. Well-studied representatives include sperm cells and the unicellular green alga Chlamydomonas, the two main actors in this thesis. Those two as well as Paramecium and Volvox are shown in figure 1.1.

Sperm cells. Most sperm cells have a single flagellum with a typical length of about $50\ \mu\text{m}$ and an ellipsoidal cell body with semi axis lengths of about $5\ \mu\text{m}$. The flagellum performs a whip-like motion, which is similar to a traveling wave that propagates from the cell body to the tail. Although the beating happens to be approximately in a plane, a small out of plane component leads to helical swimming paths [30, 31]. This form of the trajectory supports the mechanism to perform chemotaxis [64], that means that the mean swimming path follows a chemical gradient of signaling molecules, which is established by diffusion from the egg.

Chlamydomonas. Chlamydomonas is a unicellular alga with two flagella that beat in synchrony in a breast stroke like manner. Each flagellum bends in a similar way as flagella of sperm cells, but the mean curvature is larger. This results in a motion that can be characterized in two phases: The power stroke, in which the flagella are rather straight and move from the front to the back, where front means the cell part in the direction of swimming motion, leads to forward motion of the cell body center. During the recovery stroke, the flagella move from back to front and slide very near to the cell body. This results in backward motion, which is about half the distance of the forward motion. As in the sperm cell, the flagellar beat has a small out of plane component, which leads to a screw like swimming path [111]. This allows Chlamydomonas to perform phototaxis, which means that it swims towards or away from light in a helical swimming path [8], which is possible due to a single eyespot on the cell body that acts as a light sensor. This eyespot is positioned asymmetrically thus the two flagella can be differentiated into a *cis*-flagellum, which is anchored at the same side as the eyespot, and the *trans*-flagellum, which is anchored at the other side.

1.1.2 *The conserved architecture of flagella*

Flagella and cilia are an evolutionary highly conserved structure that is present in cells of major eukaryotes groups, including plants, protists and animals. [26]. Eukaryotic flagella and cilia are basically the same structure. They are different mainly in size and function. Flagella are longer and are typically used for the propulsion of microswimmers, whereas many cilia grow out of a single cell, and fluid is pumped by so called cilia carpets. In the rest of this work, I will use both terms interchangeably. The eukaryotic flagellum used in this work is not to be confused with the bacterial flagellum, which is a passive protein structure, and is driven by a rotary motor at its basal end [129, 77].

Flagella are actively bending slender cell appendages that are found in many different

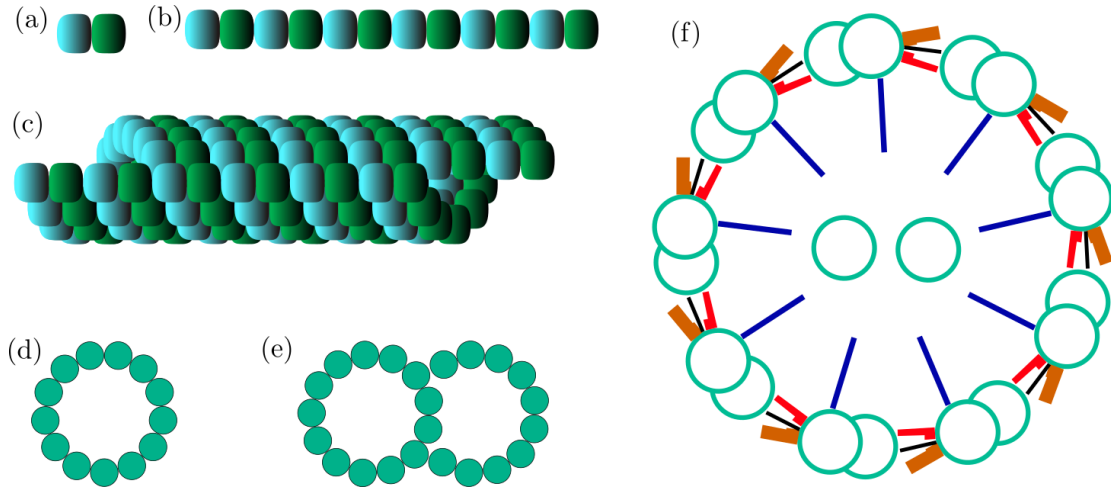


Figure 1.2: *The architecture of the axoneme.* (a) α -tubulin (●) and β -tubulin (●) form dipolar protein complexes, from which protofilaments (b) are built by successive bonding. (c) Thirteen protofilaments, circularly arranged form a microtubule. (d) Cross section of a microtubule. (e) Cross section of a microtubule doublet, consisting of ten more protofilaments than a microtubule. (f) The cross section of the axoneme shows a cylindrical arrangement of nine surrounding doublets (○) which are coupled to a commonly occurring central pair (⊙) by radial spokes (↖). Neighboring microtubule doublets are coupled by nexin linkers (↗), inner dynein arms (↘) and outer dynein arms (↙)

eukaryotic cells [49]. Besides the function of motility, they are able to perform signaling and sensory function [87]. We are interested in flagella that are used for self-propulsion of microswimmers, specifically in the two flagella of the green alga *Chlamydomonas* and the one of sperm cells. *Chlamydomonas* flagellar length is about $10\ \mu\text{m}$ in length, the sperm flagellum has about $50\ \mu\text{m}$. The processes involved in regulating the flagellar length are subject to current research [10, 11].

Now, the internal structure of flagella is presented and the origin of its oscillatory motion is discussed. Then the potential function of its central pair as well as *Chlamydomonas*'s basal bodies are discussed.

Internal structure. The membrane enclosed axoneme consists of a central pair of microtubules, that is surrounded by nine microtubule doublets [2]. In between the doublets, large proteins, called dynein motors, are present [94, 45]. These renders the flagellum an active, ATP-consuming organelle [86]. Each dynein motor changes its conformation upon hydrolysis, which generates bending forces inside the axoneme. Nexin linkers provide resistance against those torques. Along the axoneme, thousands of molecular motors and nexin linker are found [94]. The flagellum is a chiral structure with a definite handedness. Figure 1.2 shows the structure of the axoneme.

Oscillatory motion. The regular bending waves of cilia and flagella represent a self-organized phenomenon, that can prevail even in the absence of the cell body. This was shown by immersing a demembrated flagellum in a solution with enough ATP and observing that it reveals a beating pattern, comparable to what is found in the living

cell [42, 3, 14]. Spontaneous oscillations of a system with molecular motors and elastic filaments occur due to a dynamic instability [16, 24, 65], which arise in many different biological systems, such as mitotic spindle oscillations [51], sarcomere oscillations in insect flight muscle [63], spontaneous hair bundle oscillations in the ear [88], and the flagella, e.g. of sperm cell and *Chlamydomonas*. The oscillations occur due to the following process. Say a certain distribution of molecular motors inside the flagellum is attached to microtubules at both ends, all others are detached. The induced stresses due to the activity of attached motors lead to sliding of doublets with respect to each other [18, 125, 17, 2], which in turn leads to a bent shape due the boundary condition for sliding at the basal body as well as sliding resistance due to the nexin linkers. The resulting bent shape leads in turn to changes of the distribution of attached and detached motors. Again stresses are induced that change the shape. Figure 1.3 illustrates this process. The microscopic origin of the exact mechanism of motor control is still a matter of debate [117, 6, 82, 56]. Nevertheless it is possible to characterize the flagellar beat by a small number of waveform parameters.

For the systems of interest in this thesis, the periodic shape deformations happen to be approximately in a plane, which might be explained by an anisotropic bending rigidity [22]. The anisotropy could be due to the orientation of the central microtubules, that lie in the plane perpendicular to the beating plane [44]. Isolated flagella without the central pair may still beat, but only with special conditions fulfilled [137]. In comparison, the ciliary beat of *Paramecium* does not lie in a plane and it is found that the central fibers rotate during the beat [96].

In *Chlamydomonas*, the basal bodies are organelles, being the anchoring spots of flagella that are connected to them by so called stellate fibers [126]. They are connected by a distal fiber [109], which also seems to set the orientation of the plane in which deformations of the flagellum happen [61, 89]. Additional stability is given by a connection of basal bodies with the nucleus [126]. The basal bodies of *Chlamydomonas* can be reoriented by a photoshock [89], which changes the beating plane, as well.

It was reported that calcium has an effect on the mean curvature of the axoneme [15]. More recent studies highlight the role of the change of calcium concentration [64]. The phototactic reaction of *Chlamydomonas* is due to different reaction of its two flagella to calcium, which is triggered by its asymmetrically positioned light-sensitive eyespot [67].

1.1.3 *Synchronization in collections of flagella*

In this section, examples of flagellar synchronization and its functional implications are discussed. Then, the theoretical basis from a physical point of view is presented, in which flagella are treated as oscillators.

Synchronization of beating flagella

Several cilia and flagella can synchronize, i.e. adapt their beats with a fixed phase difference. This striking phenomenon has inspired a continuous interest of experimental and theoretical physicists alike.

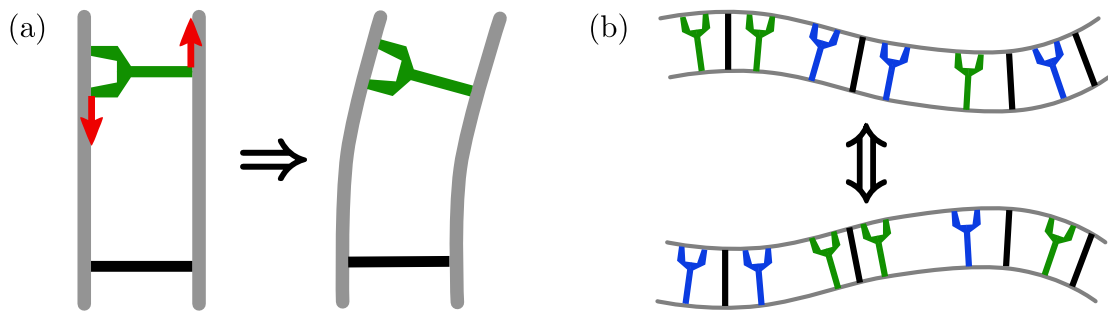


Figure 1.3: *Schematic of how the microscopic structure of the flagellar axoneme leads to bending oscillations.* (a) Two gray filaments are shown to the left which are connected by a cross linker (↙) and a molecular motor (↔). The motor exerts forces onto the filaments, resulting in an effective torque which finally leads to bending of the whole structure (right). (b) Two connected filaments are shown in gray along which several cross linkers and motors are distributed. The blue motors (↔) are detached from at least one of the gray filaments. Force balance leads to a bent shape, which again leads to attachment and detachment of motors, which leads to a different shape, and repeats the cycle.

Many cilia that are arranged on a surface and can interact hydrodynamically are called cilia carpets. They exist on epithelial tissues (lung), single cells (Paramecium) or simple multi-cellular organisms (Volvox). Synchronization of cilia carpets leads to metachronal waves, which is useful because fluid is pumped efficiently [97]. Spontaneous creation of metachronal waves through hydrodynamic interactions in model systems is observed [54]. A famous organism to study synchronization of cilia carpets is the green algal colony Volvox. Isolated ciliated cells from Volvox have been shown to synchronize by direct hydrodynamic interactions [21]. It has been proposed that likewise the cilia carpet on the surface of Volvox synchronizes [20].

As another example, the beat of multiple sperm cells can synchronize with each other through hydrodynamic interactions [110, 107] when swimming close to each other. High density sperm suspensions form self-organized vortices and in turn form a hexagonal lattice, which is due to hydrodynamic and steric interactions [138].

Chlamydomonas swims with a breast-stroke movement of its two flagella. Its flagella beat synchronously, which allows the cell to swim straight and fast [12]. Would its two flagella beat out of phase, rotational movement would be dominant and its net swimming speed would be tremendously reduced.

Putative mechanism for flagellar synchronization in Chlamydomonas. It has been suggested already by Gray in 1955 that direct hydrodynamic interactions could be the cause of flagellar synchronization [50]. The first direct demonstration of flagellar synchronization by hydrodynamic interactions was given by Brumley et al. [21], using two flagellated cells held by separate micro-needles at a distance. The synchronization strength decreased as a function of increasing separation distance. In these experiments, synchronization could only be mediated through the surrounding fluid. Later, a joint experimental and theoretical study suggested an alternative synchronization mechanism that is independent of direct hydrodynamic interaction and is operative in at least one

important model organism, the biflagellate green alga *Chlamydomonas* [41].

An additional question concerns whether a putative synchronization mechanism stabilizes in-phase or anti-phase synchronization in pairs of flagella. It was observed, that an isolated flagellar apparatus still leads to in-phase synchronization [61]. In contrast, the flagellar dominance mutant *ptx-1* of *Chlamydomonas* is non-phototactic and shows perfect anti-phase synchronization [80]. Interestingly, *Chlamydomonas* cells swimming in the dark were observed to switch between the in-phase synchronized state, in which the swimming path is straight, and the anti-phase synchronized state [99].

A recent experiment, in which the *Chlamydomonas* cell is exposed to oscillating external flow, suggests basal body coupling as the primary synchronization mechanism [104].

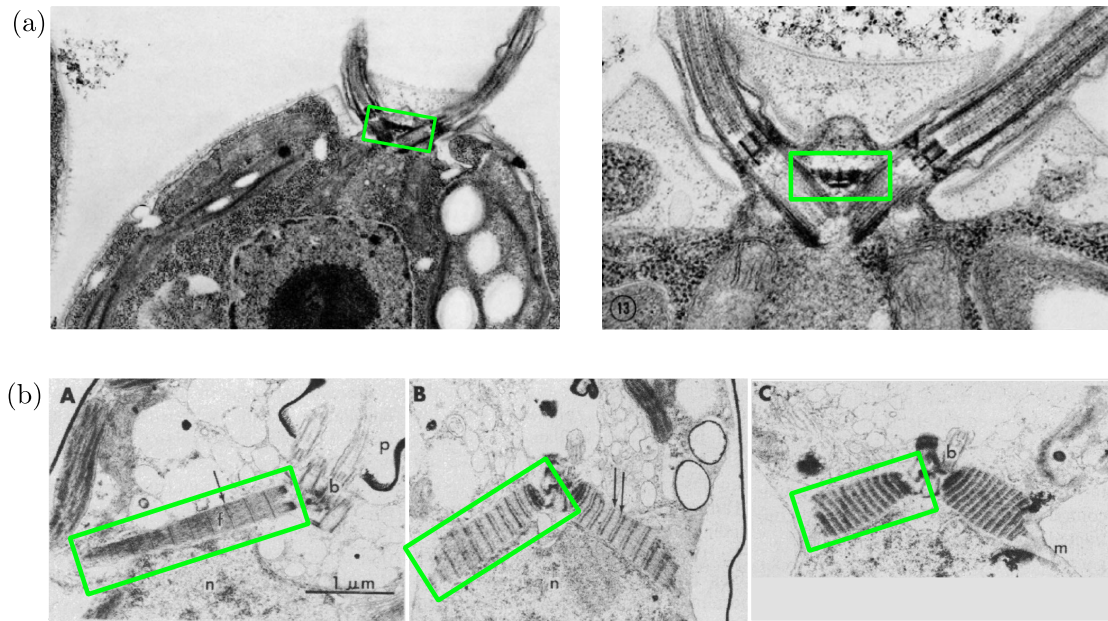


Figure 1.4: *Distal striated fiber in the basal apparatus of green alga is contractile.* (a) The distal striated fiber of *Chlamydomonas* connects its two basal bodies. Image with modifications from [109], with permission. (b) Electron micrographs of the rizoheplast of *Platymonas Subcordiformis*, a quadri-flagellate green alga for different concentrations of Calcium. With modifications from [113], with permission.

The basal body as explicit synchronization coupling. The basal bodies are the anchoring points of the flagellar axonemes. The same structures form the cores of the centrioles, which also serve as organizing centers of the mitotic spindle during cell division. In *Chlamydomonas* the basal bodies are connected by an ashlar-formed structure, known as distal striated fiber. Electron-micrographs of the basal apparatus with the distal striated fiber is shown in figure 1.4 (a). The distal striated fiber is approximately $0.3 \mu\text{m}$ long, $0.075 \mu\text{m}$ thick, and the out-of beating plane extension is about $0.25 \mu\text{m}$ [109]. The contractility of those fibers can be controlled by the intracellular Calcium concentration [58, 136, 113]. The contraction occurs in milliseconds, and is due to the Ca^{2+} -modulated contractile protein centrin [119]. Continuous cycles of contraction and reextension are observed with only in the presence of ATP, highlighting

the active nature of these contractions [114], see also figure 1.4. The vfl-1 mutant is centrin defective [135].

Recent experimental findings suggest, that the basal body apparatus may be a key prerequisite responsible for flagellar in-phase synchronization in *Chlamydomonas* [132].

Dynamics of coupled phase oscillators

We consider two generic oscillators that are coupled weakly. A single oscillator immersed in a medium is exposed to friction forces due to motion and is driven by a constant force. Thus, its phase φ propagates constantly in time with the frequency $\omega_0 = \dot{\varphi}$. Two coupled oscillators labeled L and R , with frequencies ω_i and phases φ_i for $i \in \{L, R\}$ are effectively described by the Adler equation [1], considering their phase lag $\delta = \varphi_L - \varphi_R$ and frequency mismatch $\Delta\omega = \omega_L - \omega_R$. The phase lag dependent coupling between the oscillator must be 2π -periodic, and is approximated by its first mode. Also, it is assumed that the coupling is weak, which means that the dynamics of the phases φ_i is much faster than the dynamics of the phase lag δ . The Adler equation writes as

$$\dot{\delta} = \Delta\omega - \lambda \sin(\delta). \quad (1.1)$$

For details, see the derivation in appendix E.

For the case of two identical oscillators with equal intrinsic frequencies, $\Delta\omega = 0$, we observe one stable fixed point at $\delta^* = 0$ and one unstable fixed point at $\delta^* = \pi$ for positive synchronization strength λ . If the two oscillators have different intrinsic frequencies, $\Delta\omega \neq 0$, phase locking still occurs if the synchronization strength λ is large enough, $|\lambda| > |\Delta\omega|$.

Synchronization in minimal models need broken symmetries. Any system of coupled oscillators must break the symmetry under parity- and time-reversal to achieve net synchronization. For seeing this, consider a system of two coupled oscillators, that is symmetric under parity- and time-reversal and has a fixed point with a Lyapunov exponent $-\lambda > 0$ for the phase difference. For the case of synchronizing systems, λ is called synchronization strength. A parity transformation does not change the physics and λ is unchanged. The time-reversion leads to a change of sign of $\lambda \rightarrow -\lambda$. So, if the system is symmetric under combined parity transformation and time-reversal, we have $\lambda = -\lambda$, which is only true for $\lambda = 0$, which is interpreted as a system that does not phase lock.

There is a multitude of possibilities to break that symmetry. Obviously, considering the time dependent Navier-Stokes equation breaks that symmetry and leads to synchronization [128]. But also physical constraints like a wall at one side in combination with hydrodynamic interactions [35, 131], front-back asymmetric beat patterns [34], phase dependent flagellar driving forces or energy dissipation rates [130] or elastic degrees of freedom with non-isochrone limit cycles [95] break that symmetry. The latter synchronization mechanism is presented in figure 1.5. Most portrayed mechanisms are embodied for *Chlamydomonas* which makes it a very interesting model organism. It prompts the question which synchronization mechanism dominates in this biological system.

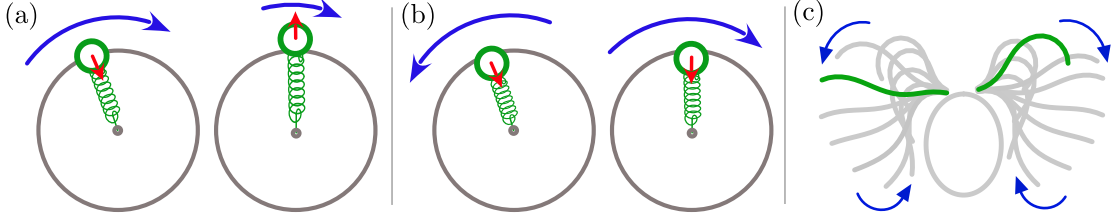


Figure 1.5: *Minimal model of hydrodynamic synchronization in the presence of amplitude compliance.* A sphere moves along a circular orbit. Its position in polar coordinates can be expressed by a phase φ and a radial component that we call amplitude A . Be the non-isochrony in this example in a way such that a larger distance from the center (amplitude) leads to a higher friction in the tangential direction (phase). The interactions of the rotating spheres are in a way, such that their amplitudes change due to the tangential speed of the coupled oscillator. (a) A small phase difference leads to a change in the distance to the center, which due to non-isochrony changes the velocities of the spheres such that phases adjust. In-phase synchronization is stable. (b) As (a) but one oscillator is mirrored horizontally, which effectively flips the rotational motion. This system does not show stable in-phase synchronization, because both oscillator change the phase speed in the same way. (c) The *Chlamydomonas* can be described similarly to (b), but the sign and the strength of the non-isochrony generally is a function of the phase, and the hydrodynamic interactions between the two 'flagellar oscillators' are much richer.

Active fluctuations blur the synchronization behavior. The bending of flagella is due to stochastic stepping of molecular motors with a preferred direction [59]. This is reflected by a characteristic level of active noise of the flagellar beat, which one can measure as the finite width of power spectra [107, 132]. We effectively describe active fluctuations by adding a noise term ξ in the Adler equation (1.1)

$$\dot{\delta} = \Delta\omega - \lambda \sin(\delta) + \xi. \quad (1.2)$$

In pairs of synchronized flagella active noise induced phase slips occur for a higher level of noise as well as for lower synchronization strength [47]. More generally, the probability for finding a system of coupled oscillators in a state with $\delta \approx \pi$ increases with noise [133]. The probability density p for finding a system at a particular phase difference δ is given by

$$p(\delta) \propto e^{(\Delta\omega + \lambda \cos \delta)/D}, \quad (1.3)$$

with phase diffusion D .

1.2 Hydrodynamics at the microscale

Section overview. The Navier-Stokes equation is derived from a balance of forces and mass conservation. Then the Stokes equation is presented, which is valid when the Reynolds number Re is small, applicable in the realm of microswimmers. Next, higher-order fundamental solutions are discussed based on the Green's function approach for solving the Stokes equation.

1.2.1 Navier-Stokes equation

This section follows closely the exposition in [55]. The continuum theory of fluids is given by two conditions, the conservation of mass and a force balance per volume element of the fluid. The volume element for the hydrodynamic theory to be applied must be much smaller than the system of interest, such that infinitesimal calculus can be applied, and it must be much larger than a single structural unit of the microscopic scale, which, in the case of water, would be a single water molecule. Throughout this thesis, we are interested in the hydrodynamics of water in three space dimensions.

First, we state that mass is conserved by stating the following continuity equation with mass density ρ , time t , and fluid flow \mathbf{u}

$$\frac{\partial \rho}{\partial t} = -\nabla \cdot (\rho \mathbf{u}). \quad (1.4)$$

The density ρ changes according to the gradient of density flux $\rho \mathbf{u}$.

Next, we state that all the forces arising from fluid movement are balanced by external forces

$$\frac{\partial(\rho \mathbf{u})}{\partial t} + \nabla \cdot (\rho \mathbf{u} \mathbf{u}) = \nabla \cdot \mathbf{\Pi} + \rho \mathbf{f}. \quad (1.5)$$

Here, \mathbf{f} denotes possible external body forces such as gravitational forces and $\mathbf{\Pi}$ denotes the stress tensor. We use the constitutive relation for Newtonian fluids for the stress tensor $\mathbf{\Pi}$ that consists of a diagonal term related to the pressure p and a symmetric term that couples to the strain rate via the viscosity μ ,

$$\mathbf{\Pi} = -p \mathbf{1} + \mu (\nabla \mathbf{u} + (\nabla \mathbf{u})^T). \quad (1.6)$$

Here, we neglect a bulk compressibility which would have to be included for compressible fluids. Throughout this thesis, we assume $\nabla \rho = 0$ and $\frac{\partial \rho}{\partial t} = 0$. With this, equations (1.4) and (1.5) simplifies to

$$\begin{aligned} \nabla \cdot \mathbf{u} &= 0 \\ \rho \left(\frac{\partial \mathbf{u}}{\partial t} + (\mathbf{u} \cdot \nabla) \mathbf{u} \right) &= -\nabla p + \mu \Delta \mathbf{u} + \rho \mathbf{f}. \end{aligned} \quad (1.7)$$

This is the well known Navier Stokes equation. The left hand side consists of inertial forces and the right hand side contains viscous and external forces.

1.2.2 The limit of low Reynolds number

This section follows closely the exposition in [55]. In microswimming, inertial effects can be usually neglected. This is because the relevant objects are small and slow, implying that viscous forces ($\propto \mu l U$) dominate over inertial forces ($\propto \rho U^2 l^2$). The value of the Reynolds number

$$\text{Re} = \frac{\rho U l}{\mu} \quad (1.8)$$

with length scale l and velocity scale U , is a measure for the importance of inertial effects to explain physical effects. We can see this by representing the incompressible Navier Stokes equation (1.7) in terms of rescaled dimensionless quantities $\tilde{\mathbf{u}} = \mathbf{u}U^{-1}$, $\tilde{\mathbf{r}} = \mathbf{r}l^{-1}$, other quantities are expressed analogously. The Navier-Stokes equation reads in rescaled variables

$$\text{Re} \left(\frac{\partial \tilde{\mathbf{u}}}{\partial \tilde{t}} + \tilde{\mathbf{u}} \cdot \tilde{\nabla} \tilde{\mathbf{u}} \right) = -\tilde{\nabla} \tilde{p} + \tilde{\Delta} \tilde{\mathbf{u}} + \tilde{\mathbf{f}}. \quad (1.9)$$

Thus, the Reynolds number Re is the ratio between viscous forces ($-\nabla p + \mu \Delta \mathbf{u}$) and inertial forces, consisting of a dynamic acceleration term $\partial \mathbf{u} / \partial t$ and a convective acceleration term $\mathbf{u} \cdot \nabla \mathbf{u}$.

Typical values for a Chlamydomonas cell are $U \approx 0.1 \text{ mm s}^{-1}$ and $l \approx 0.01 \text{ mm}$, which leads to $\text{Re} \approx 0.001$ in water. For a sperm cell, we find $\text{Re} \approx 0.01$.

We take the limit $\text{Re} = 0$ and obtain the Stokes Equations

$$\begin{aligned} \mu \nabla^2 \mathbf{u} &= \nabla p - \mathbf{f}, \\ \nabla \cdot \mathbf{u} &= 0. \end{aligned} \quad (1.10)$$

Note that the Stokes equation (1.10) does not possess any explicit time dependence and is linear. It can be solved by the following Greens function

$$T_{ij} = \frac{1}{8\pi\mu r} \left(\delta_{ij} + \frac{r_i r_j}{r^2} \right) \quad (1.11)$$

which is a rank 2 tensor with $r = |\mathbf{r}|$ and is called Oseen tensor. Note that the components of T decay with distance as $\propto r^{-1}$. The fundamental solution of the Stokes equation characterizes the flow field in response to a point force located at the origin. It can be used to compute flow fields from arbitrary force densities \mathbf{f} by superposition

$$\mathbf{u}(\mathbf{r}) = \int d^3 r' \mathbf{T}(\mathbf{r} - \mathbf{r}') \mathbf{f}(\mathbf{r}'). \quad (1.12)$$

The flow field $\mathbf{u}^{(1)} = \mathbf{T} \cdot \mathbf{F}_0$ that is due to a point force \mathbf{F}_0 is called Stokeslet and is the fundamental solution of the Stokes equation (1.10). An example of a Stokeslet is shown in Figure 1.6.

In the next section, I present a way to represent the flow field as a superposition of singularities, which requires a number of singularities for accurate representation of flow fields that is much smaller than the typical number of discretization points of a surface of a microswimmer used in hydrodynamic computations. These higher order singularities are called multipoles. Higher multipoles allow for a descriptive classification of flow fields.

1.2.3 Multipole expansion of flow fields

In electrostatics, the method of multipole decomposition is used to characterize electric potential fields in a compact way and approximate these efficiently. The electric charges

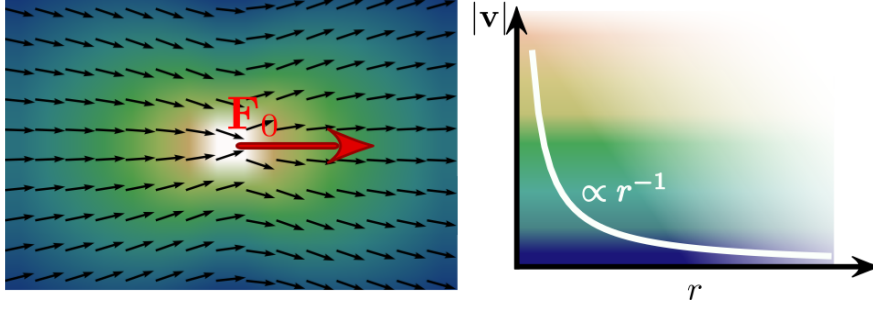


Figure 1.6: *Stokeslet: the fundamental solution of the Stokes equation.* The flow field that is induced by a point force (red arrow) is called Stokeslet. The black arrows depict the direction of flow. The color represents the flow strength $|\mathbf{u}|$, which diverges at the point force's origin, and declines with the distance as $1/r$.

are the source of the potential and are decomposed into so called multipoles, which can readily be superimposed. The same decomposition can be applied to the force density \mathbf{f} inside the fluid, with the difference, that it is a vector field, whereas the charges are a scalar field. We present a more thorough discussion on force multipoles in appendix A.1. For completeness, the definition of the force multipoles as they are used in this thesis are presented as in [118]

$$f_{\gamma_1 \dots \gamma_n, \alpha}^{(n+1)} = \frac{1}{n!} \int_S dS r_{\gamma_1} \dots r_{\gamma_n} f_{\alpha}(\mathbf{r}), \quad (1.13)$$

defining rank $(n + 1)$ tensors with components $f_{\gamma_1 \dots \gamma_n, \alpha}^{(n+1)}$. The flow field arising from a set of force multipoles is

$$u_{\alpha}(\mathbf{r}) = \sum_{n=0}^{\infty} u_{\alpha}^{(n+1)}(\mathbf{r}) = \sum_{n=0}^{\infty} (-1)^n \partial_{\gamma_1 \dots \gamma_n} T_{\alpha\beta}(\mathbf{r}) f_{\gamma_1 \dots \gamma_n, \beta}^{(n+1)}. \quad (1.14)$$

Consider the following example for seeing the descriptive nature of force multipoles. An object with a moving shape immersed in a viscous fluid induces a force density on its surface that generates flows. At a distance to that object the flow field has a simple structure, with just one direction of in-flow or out-flow. We call this flow field at a distance far-field and represent it by the second-order singularity $u_{\alpha}^{(2)} = -\partial_{\gamma} T_{\alpha\beta} f_{\gamma, \alpha}^{(2)}$, which is the second term of the flow field \mathbf{u} in equation (1.14). Note that if no external forces are applied, the first mode vanishes, since it just represents the net force acting on the object. With decreasing distance to the shape-changing object higher modes must be considered to faithfully represent the flow field it creates. The flow field at the immediate vicinity of the object is called near-field. Figure 1.7 shows the intricate near-field of three moving spheres and its generic far-field.

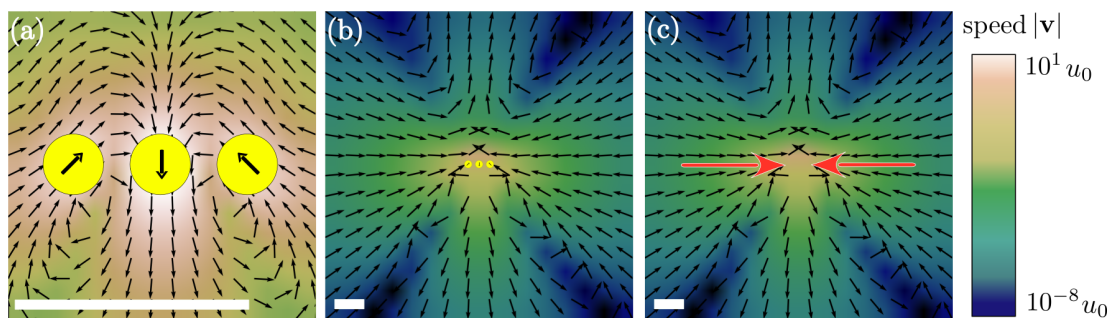


Figure 1.7: *Example of how the leading-order multipole dominates the far-field.* (a) Three equally sized spheres and their translational speeds are shown by the black arrows inside yellow circles. Note that the sum of forces is zero. The resulting flow field has an intricate structure. The net speed of a sphere is u_0 . (b) The same flow field as shown to the right, but at a much larger scale, see white scale bars. (c) The overall structure of the flow field has a very generic structure, which can be well approximated by the flow induced by a pair of forces (red arrows).

1.3 Self-propulsion by viscous forces

Microswimmers swim at low Reynolds number, thus friction forces due to viscosity are much larger than inertial forces. If a particle that changes its shape stops its motion in a sudden, the flow of the surrounding fluid would stop at an instant. Also, if a microswimmer swims with a certain swimming speed and then stops its shape changes, the swimming speed will be zero, instantly. To compare this situation to experiences that we are used to in our daily lives, one can imagine the situation of swimming in honey, and we are allowed to perform one breaststroke in days [101].

Section overview. The required non-reciprocal shape movements that are necessary for swimming are discussed for two toy-model swimmers, first. Then, the effect of swimming on the surrounding fluid is discussed.

1.3.1 Self propulsion requires broken symmetries

Swimming at low Reynolds number is very different from swimming at the human length scale. For single cells that swims in a fluid, inertia is negligible [76, 37]. Thus, propulsion is achieved through viscous forces only [127]. Non-reciprocal shape changes can overcome the time-reversibility of the Stokes equation, thus facilitating net propulsion [9, 120]. Flagellated cells achieve this in the form of a periodic flagellar bending waves [50, 111, 12]. Any swimmer that performs a cyclic motion or shape change must break the time-reversal symmetry [101]. This context is known as the Scallop theorem. Non-reciprocal shape changes can only be achieved by possessing more than one degree of freedom.

Another way to allow a reciprocal swimmer to propel, is to expose it to a non-

Newtonian fluid, because its elastic components provide memory to the system that breaks time-reversal symmetry [103].

Theoretical minimal models are developed to highlight the theoretical basis of swimming at the microscale and to suggest simple architectures for constructing nanomachines. A particularly simple example is the three-sphere swimmer first proposed by Najafi [92, 48], which has also been realized experimentally [52]. Another even simpler model is Vic's swimmer [33]. It is a system with two spheres of variable radius and variable mutual distance. Figure 1.8 shows the non-reciprocal shape changes of Vic's swimmer and the resulting trajectory.

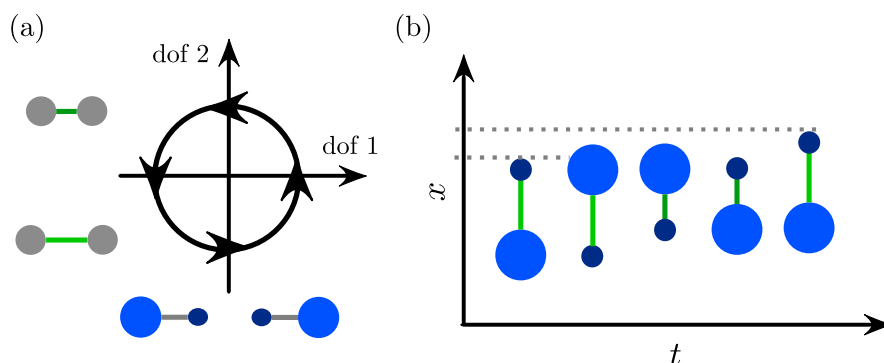


Figure 1.8: *Breaking time reversal symmetry with two degrees of freedom: The pushmepullyou stroke.* A schematics of Vic's swimmer [33] performing a pushmepullyou stroke [4] is shown. (a) The swimmer has one degree of freedom that increases the size of one of the two spheres while shrinking the other and one degree of freedom that sets the distance between the spheres. The shape changes time irreversible. (b) Changing the shape as depicted in panel (a), the swimmer can achieve net propulsion.

Net-propulsion by periodic shape changes is a second-order effect, implying that net displacement after one cyclic swimming stroke is proportional to the square of the amplitude of the swimming stroke [121, 100]. Thus, the propulsion speed of a microswimmer is quadratic in the amplitude of the shape changes. In particular, this is true for the Najafi's model swimmer [92] and Vic's model [33] that performs the so called pushmepullyou stroke [4].

Note that Vic's swimmer represents an exception to the general rule that hydrodynamic interactions are necessary for propulsion. Vic's swimmer does not necessarily need hydrodynamic interactions for propulsion, while Najafi's three sphere swimmer does. Swimming with flagella implement hydrodynamic interactions locally in terms of anisotropic friction coefficients for movement perpendicular or parallel to its surface, as well as globally, due to interactions of flagella with the cell body.

The role of anisotropic friction is highlighted in resistive-force theory [50]. Non-local hydrodynamic interactions are not considered there, but self-propulsion of shape changing object can occur due to local hydrodynamic interactions. These are encoded in the friction anisotropy, which means that the friction for motion parallel to the long axis of a slender object ζ_{\parallel} is different to the friction for motion perpendicular to the long axis ζ_{\perp} [38]. For a more complete description of resistive-force theory, see also

appendix A.2.

1.3.2 Signatures of flowfields: pusher & puller

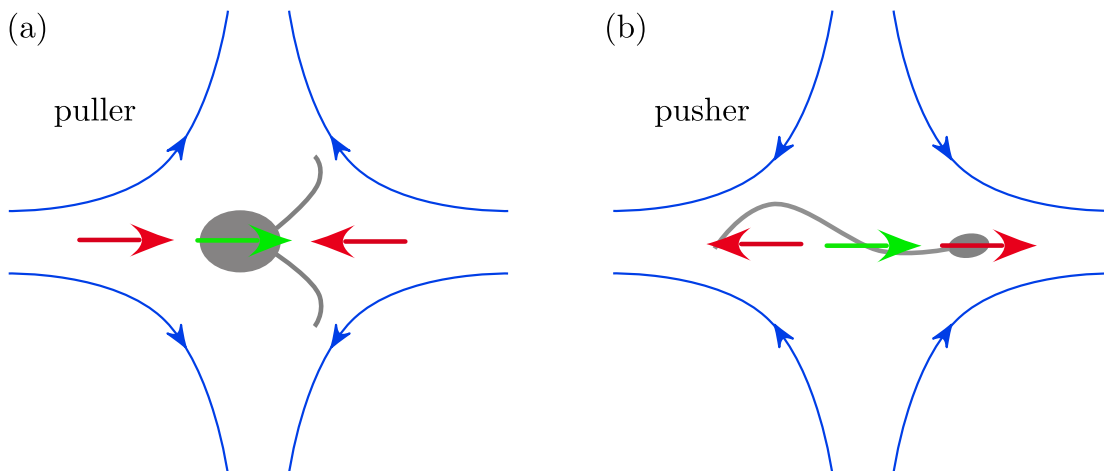


Figure 1.9: *Flow-signatures of puller- and pusher-type swimmers.* The microswimmer is shown in gray, and the surrounding mean flowfield is sketched as blue streamlines. (a) *Chlamydomonas* is a typical representative of puller-type swimming during the effective stroke of its flagellar beat. Its mean swimming direction (green arrow) is perpendicular to the mean outflow direction. (b) The sperm cell is a typical pusher type swimmer with its outflow direction in the same direction as its swimming direction.

While swimming, microswimmers generate flow fields whose far-field has a dipolar structure [62]. Microswimmers are commonly classified as either pusher- or puller-type swimmers, based on the sign of the hydrodynamic force dipole [76]. The character of the swimmer becomes important when considering hydrodynamic interactions with other objects like boundaries, passive particles or other swimmers. A pusher, for example, will experience inward fluid flow from the side, which leads to attraction by walls [76]. Figure 1.9 illustrates the simplified notion that the *Chlamydomonas* cell is a puller and the sperm cell is a pusher. We will present a refined notion in chapter 2.

The near field of swimmers cannot be described by the dipole field alone. At least third-rank tensors are necessary to describe features such as swirling flows around *Volvox* [32] or stagnation points near *Chlamydomonas* [53, 43]. Despite these limitations, in recent theoretical studies with many interacting microswimmers, the simple picture with constant force dipole is implemented [140], complying with the dilute limit.

Dense suspensions of microswimmers show active rheological responses, such as shear thinning, which can be attributed to the swimmer character [105, 46]. Qualitative differences in the swimmer density dynamics are observed, depending on whether the swimmers represent pushers, pullers or neutral swimmers [84]. Theoretic studies show that in viscoelastic fluids, the fluid elasticity has a small effect on a suspension of pullers, while it significantly affects the pushers [81]. Swimmers accumulate at boundaries [124, 36, 75], that means that simple, passive devices may be developed to catch

or transport active particles [66]. Since most of these effects depend on the flow signature of swimmers, a detailed understanding of its geometric and physical properties is crucial. We will explore those properties in chapter 2.

1.4 Overview of the thesis

In this thesis, we study the hydrodynamics of flagellar swimming and synchronization. We address the following questions.

- What are the dynamic features of the flow fields generated by beating cilia and flagella?
- In turn, how do external flows feed back on speed and shape of the flagellar beat?
- What are the physical mechanisms giving rise to hydrodynamic synchronization of beating flagella?

Thesis overview.

- In chapter 2, we present the computed swimming paths and flow fields of biological microswimmers. We find that the flow field oscillates with the period of the flagellar beat and describe the far-field as an oscillating dipole field. The distance at which inertial effects become important is determined.
- In chapter 3, we determine the load-response of the flagellar beat. This load-response describes how mechanical forces change the speed and shape of the flagellar beat. For this, we develop a theoretical description of *Chlamydomonas* that includes waveform compliance and intra-flagellar friction and compare its predictions to experimental data for the situation of a clamped cell that is exposed to external flows.
- In chapter 4, we address flagellar synchronization, utilizing the load-response determined in the previous chapter. We find that an elastic coupling between bases of the two flagella is needed in our theory to explain in-phase synchronized beating. Further, we suggest non-invasive ways to change the synchronization dynamics and to test that hypothesis.
- In chapter 5 we quantify the active fluctuations of the flagellar beat. Those flagellar fluctuations lead to noisy swimming paths. We compare these active motility fluctuations to the effect of hydrodynamic interactions and thermal noise.

Methods. We analyze experimental data of high-speed videomicroscopy to extract dynamic flagellar shapes. We reconstruct a limit cycle with a dimensionality reduction algorithm, describing the flagellar beat as a limit-cycle oscillator. Numerical calculations allow us to compute fluid motion and hydrodynamic friction forces of shape changing flagella and microswimmers. We develop a theoretical description of active microswimmers using a Lagrange formalism of dissipative systems. We employ tools of nonlinear dynamics to characterize flagellar swimming and synchronization.

Experimental data that is used in this thesis. Veikko Geyer measured flagellar shapes of *Chlamydomonas* [41] in the Howard Lab at MPI CBG, which are used in the discussions on the far-field in chapter 2 and section 5.3.2 on the comparison of the effect of flagellar noise and hydrodynamic interactions. High precision tracking data of swimming bull sperm [108] was recorded by Ingmar Riedel Kruse. This is used for obtaining results in chapter 2, and the measurement of active flagellar fluctuations and swimming paths, chapter 5. Further measurements on *Chlamydomonas* provided by Christian Ruloff in the Wagner lab at the Saarland University are used in chapter 3 and 4.

Flow signatures of flagellar swimming

Swimming of shape changing microswimmers in viscous fluids is an active process in which energy provided by internal processes is converted into shape changes of active structures such as cilia and flagella and ultimately converted into heat inside those structures and in the fluid. This leads to characteristic flow-fields of self-propelled microswimmers. Periodic shape changes generate oscillatory flow fields, which dominate the near field in the vicinity of the swimmer. Inertial effects subdue oscillatory flows beyond a characteristic length, the inertial screening radius.

Chapter overview. First, the physics of freely swimming cells that propagate by periodic shape changes is presented. Second, the dynamic nature of the hydrodynamic far field is characterized in terms of pusher- and puller-type swimming and its implications for multiple swimmers are discussed. Third, the effect of unsteady acceleration is investigated and the screening length at which inertial effects start dominating is computed. Lastly, the energetics of flagellar swimming is discussed.

Note that the formalism that is used in this chapter does not account for feedback of viscous forces on the speed and shape of the flagellar beat, which will be the topic of chapter 3.

This chapter is based on a publication, of which the author of this thesis is first author [70]. The flagellar shape dynamics of freely swimming *Chlamydomonas* cells were previously recorded by Veikko Geyer in the laboratory of Jonathan Howard at MPI CBG and Benjamin Friedrich at MPI PKS did image analysis for obtaining the positions of flagellar tracking points [41]. High precision tracking data of swimming bull sperm [108] was recorded by Ingmar Riedel Kruse.

2.1 Self-propulsion of flagellated swimmers

Section overview. First, the tangent angle representation of flagellar shapes is introduced. Then it is described, how the tangent angles of flagellar shapes used in this chapter are obtained from experiments and how hydrodynamic calculations are performed. Next, the notion of the material frame is introduced, that is comoving with a microswimmer. After the introduction of the grand friction matrix, that relates forces with swimming velocities, and the discussion of its realization for *Chlamydomonas*, the integration scheme for obtaining swimming trajectories is discussed.

2.1.1 Representation of flagellar shapes

A flagellar shape at a certain time t can be described by its time dependent tangent angle $\psi(s, t)$ along the arc length s for planar flagellar shapes, which is a valid approximation for the system we are focusing at [108].

The real space coordinates $\mathbf{r}(s, t)$ along the flagellar arc length s with the starting point $\mathbf{r}_0 = \mathbf{r}(0, t)$ can be reproduced from the tangent angle ψ

$$\mathbf{r}(s, t) = \mathbf{r}_0 + \int_0^s ds' \begin{pmatrix} \cos(\psi(s', t)) \\ \sin(\psi(s', t)) \end{pmatrix}. \quad (2.1)$$

Figure 2.1 (a) graphically shows a schematic of a flagellum depicting the tangent angle representation. Panels 2.1 (b) and (c) show our convention for the starting point \mathbf{r}_0 for the sperm cell and the *Chlamydomonas* cell, respectively. Panel (d) shows a typical kymograph of the tangent angle $\psi(s, t)$.

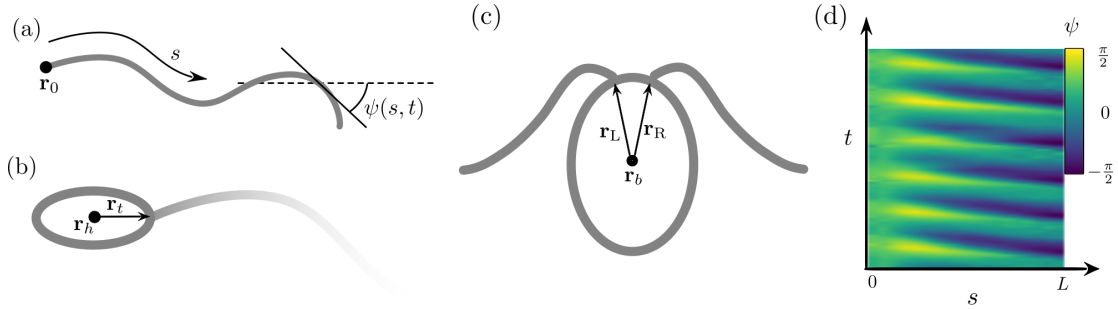


Figure 2.1: *Tangent angle representation of flagellar shapes.* (a) Tangent angle representation ψ of a schematic flagellum along its arc length s with starting point \mathbf{r}_0 . (b) For a sperm cell, the flagellar starting point is chosen at the long axis tip of the cell head $\mathbf{r}_0 = \mathbf{r}_h + \mathbf{r}_t$. (c) The *Chlamydomonas* has two flagella, thus $\mathbf{r}_{0,I} = \mathbf{r}_b + \mathbf{r}_I$ for $I \in \{L, R\}$. (d) Exemplary kymograph of processed experimental data of the tangent angle $\psi(s, t)$ measured by Christian Ruloff.

2.1.2 Computation of hydrodynamic friction forces

Underlying shape data. A Fourier analysis of the tangent angle $\psi(s, t)$ of Chlamydomonas shapes suggests, that only Fourier modes are sufficient to faithfully describe the flagellar shape changes [116], with arc length dependent Fourier coefficient $\psi_i(s)$

$$\psi(s, t) \approx \psi_0(s) + \sum_{n=1}^3 \psi_i(s) e^{i2\pi nft}. \quad (2.2)$$

Here, ψ_0 is constant in time and can be interpreted as the time averaged mean shape of the beat, which is approximately circular in real space. For simulations whose results are shown in this thesis, we use $f = 30$ Hz and a flagellar length $L = 10 \mu\text{m}$. The cell body is approximated as a prolate ellipsoid with semi axis lengths $b_{\text{long}} = 4.5 \mu\text{m}$ and $b_{\text{short}} = 3.5 \mu\text{m}$.

Similarly, a singular value decomposition of the tangent angle dynamics of sperm cells lets us conclude that two shape modes ψ_i are enough to retain about 95% of the flagellar shape variance. Thus, a good approximation for the tangent angle is

$$\psi(s, t) = \psi_0(s) + \beta_1(t)\psi_1(s) + \beta_2(t)\psi_2(s) \quad (2.3)$$

with the time dependent score functions β_i . For simulations we use $f = 50$ Hz, a flagellar length of $L = 50 \mu\text{m}$ and a cell body size of $b_{\text{long}} = 5 \mu\text{m}$ and $b_{\text{short}} = 2.5 \mu\text{m}$. We can define a phase by $\varphi(t) = \arctan2(\beta_2(t), \beta_1(t))$, implicitly making the tangent angle ψ , equation (2.3) phase dependent.

In both representations, shape changes are characterized by phase changes $\partial_t \varphi$.

Numerical calculation of friction forces. The computation of hydrodynamic friction forces is done by a fast multipole boundary element method [83], which is described in the appendix A.3. Within this approach the Stokes equation is solved, corresponding to a full treatment of hydrodynamic interactions. This is especially important for calculations with Chlamydomonas, since the mean curvature of flagella is rather large and they come very close to the cell body during the recovery stroke.

For using the fast multipole boundary element method for performing numeric, hydrodynamic calculations, the boundary conditions on the surface of the swimmer have to be provided in terms of a velocity profile on the surface. The surface itself is represented by a triangulated surface mesh. All swimmers used can be represented as a composition of an ellipsoid, such as the sperm cell head or the Chlamydomonas cell body, and curved cylinders, which represent the flagella. The former are generated by choosing coordinates in three dimensional space that lie on the surface of an ellipsoid, and then perform a Delaunay tessellation on it. A ready-made algorithm exists in the `scipy` library of the open source programming language `python` [5]. The triangulation of curved cylinders is generated by a custom procedure. See Figure 2.2 for example representations.

Note that the meshes of flagella and cell body are separated by a small gap. The relative position of the flagellar anchoring points and cell body centers are fixed realizing a physical connection with each other. The reason for meshes not to touch each other is

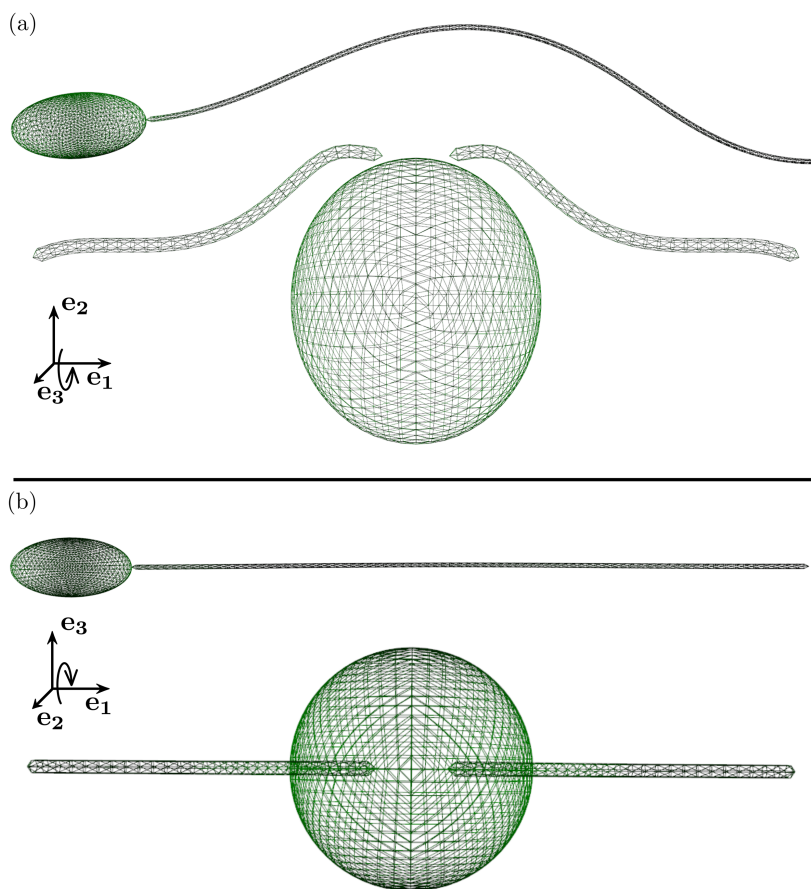


Figure 2.2: *Triangulated surface of microswimmers studied in this thesis.* Three dimensional meshes that are generated from the tangent angle description (2.1). Shown are the Chlamydomonas and a sperm cell from different views. (a) From the side view the shape changes can be observed. (b) From the top view we see the $\mathbf{e}_1\mathbf{e}_2$ mirror symmetry of the swimmer.

due to numerical issues. The results of the hydrodynamic calculations are not expected to change much if small surface parts are omitted, since the boundary conditions lead to flow velocities in the surrounding that match the omitted surface triangle's boundary conditions faithfully.

2.1.3 Material frame and rigid-body transformations

The flagellated swimmers that are treated in this chapter are Chlamydomonas cells and sperm cells. Both cells consist of an ellipsoidal cell body (or head, in the case of sperm), and one or two flagella. We can then introduce a coordinate system that is slowly comoving with the microswimmer, called material frame, with orthonormal basis vectors $\mathbf{e}_1, \mathbf{e}_2, \mathbf{e}_3$ that are defined as follows. The direction of the swimmer \mathbf{e}_1 is determined by the long axis direction of the ellipsoidally shaped cell body. The

swimming plane, which is the same plane in which the planar flagellar beat occurs, is spanned by \mathbf{e}_1 and \mathbf{e}_2 . We call \mathbf{e}_3 the binormal direction.

The material frame is embedded in the so called laboratory frame for which the fluid is at rest at infinity, $\mathbf{u}(r \rightarrow \infty) = \mathbf{0}$. The swimming path or trajectory of the microswimmer is described as the dynamics of the material frame $(\mathbf{e}_1(t), \mathbf{e}_2(t), \mathbf{e}_3(t))$ within the laboratory frame. In the laboratory frame the freely swimming cell is free from forces and torques. Note that in a system with many swimmers there is one material frame for each swimmer.

2.1.4 The grand friction matrix

Due to the linearity of the Stokes equation (1.10) the hydrodynamic friction can be represented as a linear relation between velocities \mathbf{v} (and angular velocities $\boldsymbol{\omega}$) and forces \mathbf{F} (and torques $\boldsymbol{\tau}$), which leads to the definition of the grand friction matrix $\boldsymbol{\zeta}$

$$\begin{pmatrix} \mathbf{F} \\ \boldsymbol{\tau} \end{pmatrix} = \begin{pmatrix} \boldsymbol{\zeta}_{tt} & \boldsymbol{\zeta}_{tr} \\ \boldsymbol{\zeta}_{rt} & \boldsymbol{\zeta}_{rr} \end{pmatrix} \begin{pmatrix} \mathbf{v} \\ \boldsymbol{\omega} \end{pmatrix}. \quad (2.4)$$

Block-matrix notation is used with sub-matrices $\boldsymbol{\zeta}_{ij}$ being 3×3 -matrices. $\boldsymbol{\zeta}_{tt}$ describes how translational velocities lead to translational forces, $\boldsymbol{\zeta}_{rr}$ describes the coupling of angular velocities to torques, $\boldsymbol{\zeta}_{tr}$ determines the effect of angular speeds on translational forces and $\boldsymbol{\zeta}_{rt}$ state the torques that arise from translational velocities.

Generally, for different shapes of a microswimmer the friction matrix is different resulting. Since the shape underlies a periodic motion, the components of the friction matrix are functions of the flagellar phase φ . For given phase φ , the friction matrix $\boldsymbol{\zeta}(\varphi)$ is calculated by the procedure described in appendices C.1 with the help of the fast multipole boundary element method (A.3).

The friction matrix $\boldsymbol{\zeta}$ for the Chlamydomonas cell with synchronously beating flagella oriented along the \mathbf{e}_2 -axis is shown in Figure 2.3. Note that most non-diagonal entries are zero, reflecting the symmetry of the swimmer. Specifically, there is no force velocity coupling between different frame axes in the material frame, for the translational ($\zeta_{tt,ij} = 0$ for $i \neq j$), as well as the rotational movements ($\zeta_{rr,ij} = 0$ for $i \neq j$). But there is a non-vanishing coupling $\zeta_{tr,31}$ which implies that a torque in \mathbf{e}_1 is imposed on the cell when it is translated in \mathbf{e}_3 . Note also the general property of the friction matrix $\boldsymbol{\zeta}$ to be symmetric. To see this, see equation (C.7) in the appendix.

From Figure 2.3 we observe that translational coupling $\boldsymbol{\zeta}_{tt}$ is nearly constant and positive as we would expect from a passive particle that does not change its shape. Rotational coupling $\boldsymbol{\zeta}_{rr}$ does not change its sign, but varies significantly with phase φ . The coupling between translation and rotation $\boldsymbol{\zeta}_{tr}$ and $\boldsymbol{\zeta}_{rt}$ becomes minimal in its absolute value during the recovery stroke, when the shape distance between the cell body center and the center of reaction are closest to each other.

2.1.5 Dynamics of swimming

Computation of hydrodynamic friction forces allows us to numerically determine the trajectory of a shape changing microswimmer. We assume the swimmer to deform its

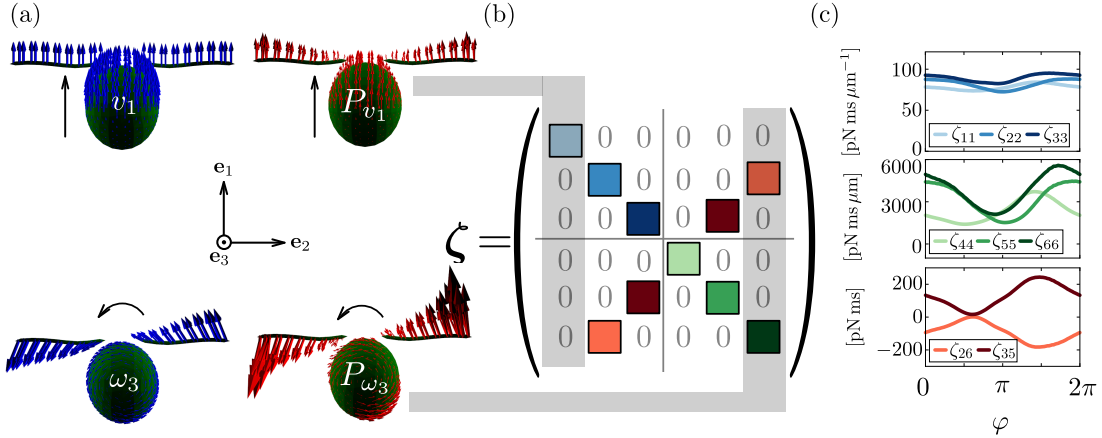


Figure 2.3: *Grand friction matrix of Chlamydomonas*. For a certain shape that is given by the phase φ , friction forces for translation and rotation in all three spatial dimensions are calculated, see panel (a). With this we capture the necessary information for constructing the grand friction matrix ζ , see equation (2.4). A schematic representation of ζ is shown in panel b. Symmetries of the swimmer dictate zero entries as shown. Non-zero entries are shown in panel (c) with color code as shown.

shape $S(\varphi)$ periodically with a phase φ . When the swimmer is restrained from moving, such that its translational and rotational speed are zero, constraining forces $\mathbf{F}^{\text{clamped}}$ and torques $\boldsymbol{\tau}^{\text{clamped}}$ have to be applied

$$\begin{aligned}\mathbf{F}^{\text{clamped}} &= \int_{S(\varphi)} dS(\mathbf{r}') \mathbf{f}(\mathbf{r}'), \\ \boldsymbol{\tau}^{\text{clamped}} &= \int_{S(\varphi)} dS(\mathbf{r}') (\mathbf{r}' - \mathbf{r}) \times \mathbf{f}(\mathbf{r}'),\end{aligned}\tag{2.5}$$

with the force surface density \mathbf{f} and the position \mathbf{r} of a reference point of the microswimmer. We use the composite force vector $\mathcal{P}^{\text{clamped}} = (\mathbf{F}^{\text{clamped}}, \boldsymbol{\tau}^{\text{clamped}})^T$ as a shorthand.

Rigid body motions $\mathbf{U}^{\text{mat}} = (\mathbf{v}^{\text{mat}}, \boldsymbol{\omega}^{\text{mat}})^T$ of the shape $S(\varphi)$ lead to forces $\mathcal{P}^{\text{rigid}} = \zeta \mathbf{U}^{\text{mat}}$, which are to be balanced by the active forces $\mathcal{P}^{\text{clamped}}$, in the case of force- and torque-free swimming.

$$\begin{aligned}\mathcal{P}^{\text{rigid}} &= -\mathcal{P}^{\text{clamped}} \\ \Rightarrow \mathbf{U}^{\text{mat}}(\varphi) &= -\zeta^{-1} \mathcal{P}^{\text{clamped}}\end{aligned}\tag{2.6}$$

Figure 2.4 shows the phase-dependent constraining force relative to the material frame of the swimmer.

The self-consistently determined translational and angular velocities \mathbf{U}^{mat} are given in the material frame and have to be integrated together with position \mathbf{r} and orientation $\boldsymbol{\Omega}$ of the microswimmer. The orientation of the swimmer is represented as a rotation

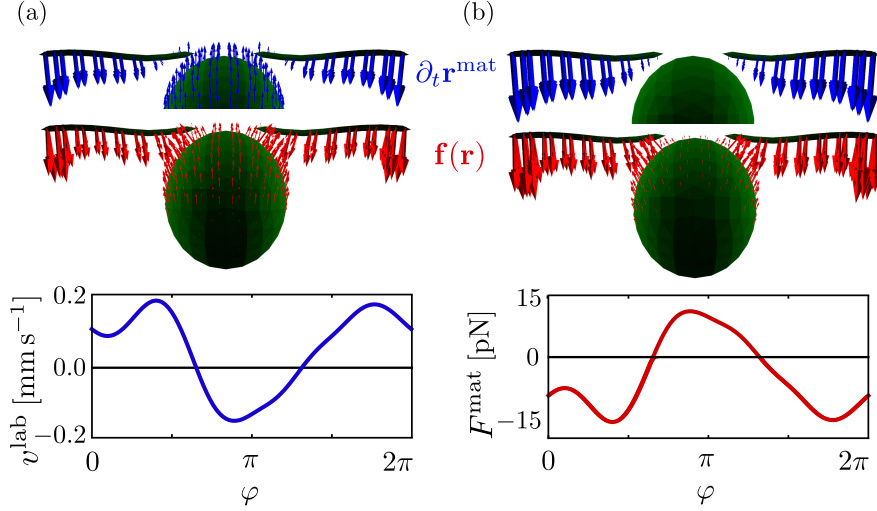


Figure 2.4: *Constraining forces and swimming velocity of Chlamydomonas.* The swimming speed v^{lab} during one beat cycle is shown as blue curve. During the power stroke, the cell translates forward, whereas during the recovery stroke it moves backward. For phase $\varphi = 0$, the velocity profile of the flagellar shape change (blue arrows) as well as its force surface density (red arrows) that is exerted onto the fluid are shown. Analogously, the constraining force that is needed for clamping a beating cell is shown as red curve, and the same shapes of Chlamydomonas in the clamped state are shown. Note, that the freely swimming cell experiences smaller forces on its flagella while the force density on the cell body is increased.

matrix, and is interpreted as the rotation that is necessary for bringing an object into the current orientation with respect to the initial orientation $\mathbf{\Omega}(\varphi=0) = \mathbf{1}$. We furthermore require $\mathbf{v}^{\text{lab}}(\varphi=0) = \mathbf{v}^{\text{mat}}(\varphi=0)$ and $\boldsymbol{\omega}^{\text{lab}}(\varphi=0) = \boldsymbol{\omega}^{\text{mat}}(\varphi=0)$. Thus, the directions are for all phases are known if the orientations are known.

$$\begin{aligned}\boldsymbol{\omega}^{\text{lab}}(\varphi) &= \mathbf{\Omega}(\varphi) \cdot \boldsymbol{\omega}^{\text{mat}}(\varphi=0) \\ \mathbf{v}^{\text{lab}}(\varphi) &= \mathbf{\Omega}(\varphi) \cdot \mathbf{v}^{\text{mat}}(\varphi=0)\end{aligned}\tag{2.7}$$

The swimmer positions and orientations are updated according to the following Euler scheme

$$\begin{aligned}\mathbf{\Omega}(\varphi + d\varphi) &= \mathfrak{R}(\mathbf{\Omega}(\varphi) \cdot d\boldsymbol{\omega}(\varphi)) \cdot \mathfrak{R}^{-1}(\mathbf{\Omega}(\varphi) \cdot d\boldsymbol{\omega}(\varphi)) \\ d\boldsymbol{\omega}(\varphi) &= \boldsymbol{\omega}^{\text{lab}}(\varphi) \cdot d\varphi \\ \mathbf{r}(\varphi + d\varphi) &= \mathbf{r}(\varphi) + \mathbf{v}^{\text{lab}}(\varphi) \cdot d\varphi.\end{aligned}\tag{2.8}$$

$\mathfrak{R}(\mathbf{a})$ is the rotation matrix that performs the rotation of a three dimensional vector around the axis \mathbf{a} . Figure 2.4 shows the computed phase-dependent velocity of the material frame of a swimming Chlamydomonas cell relative to the laboratory frame.

2.2 The hydrodynamic far field: pusher and puller

A shape-changing microswimmer exerts a distribution of forces at its surface onto the surrounding fluid, which generates flow and stress. Far away from the swimmer, the resultant flow field has a characteristic structure that can directly be mapped to a force dipole, the leading order singularity of the multipole expansion of the force field exerted by a self-propelled swimmer. We reveal a three dimensional fine structure of the character based on symmetries by introducing the concepts of symmetry and planarity, which capture time dynamics and reveals alternation between pusher and puller. The description is applicable to swimmers with a mirror symmetry, showing a planar beat.

2.2.1 The flow generated by a swimmer

In this section, the flow field that a microswimmer generates is shown and the relation to the force dipole is presented. This can be done for any shape changing swimmer and the swimming of *Chlamydomonas* is shown explicitly.

Given the force surface density \mathbf{f} that is obtained by numerical calculations of a shape changing swimmer, the flow-field \mathbf{u} of the surrounding fluid can be obtained by propagating \mathbf{f} with the Oseen tensor \mathbf{T} , see equation (1.11). Figure 2.5 shows the flow field for two different scales, the near field and the far field.

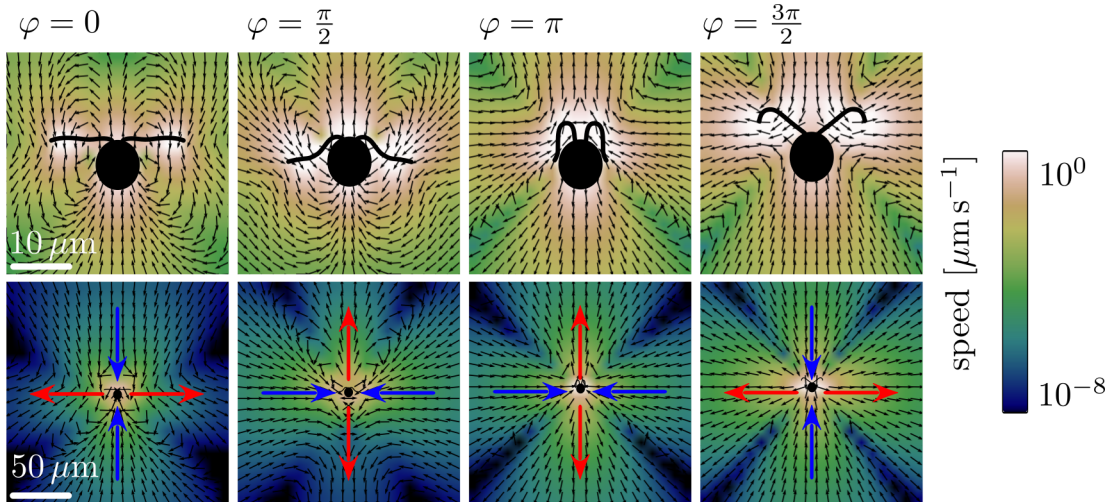


Figure 2.5: *Computed flow field exerted by a freely swimming Chlamydomonas cell.* The computed flow field that is exerted by shape changes of *Chlamydomonas* for four different values of the phase $\varphi \in \{0, \pi/2, \pi, 3\pi/2\}$ are shown. (top) The near field has an intricate structure with vortices. (bottom) The far field is very regular with two outflow zones and two inflow zones that are emphasized by red (out-flow) and blue (in-flow) arrows and can be well approximated by leading order singularities.

In the direct neighborhood of the *Chlamydomonas* cell, the flow field has an intricate structure and changes during the beat cycle. For larger distances, the structure becomes much more regular, but is still very different during the beat. Interestingly, the direction

of flow changes sign at least twice during the beat. A more subtle observation is, that at some phases (e.g. $\varphi = 0$) the amount of flow in the plane and flow out of the plane are different, which is explained by fluid flow in the binormal direction \mathbf{e}_3 , perpendicular to the plane of beating.

An approximation to the far field is the Stokes doublet, which is the flow field resulting from a force dipole exerted on the fluid. Schematics of those are shown in figure 2.5 as red (out flow direction) and blue (in flow direction) arrows. The doublet has no tangential contribution and is fully characterized by its radial part. The magnitude of flow vectors decreases as $\propto r^{-2}$ with distance r from the doublet source. Therefore, we use radial flow plots depicted in figure 2.6 to represent the dipole flow without losing information about the character of the flow. Since there is a bijective mapping between a force dipole and its Stokes doublet it also fully describes the character of the force dipole.

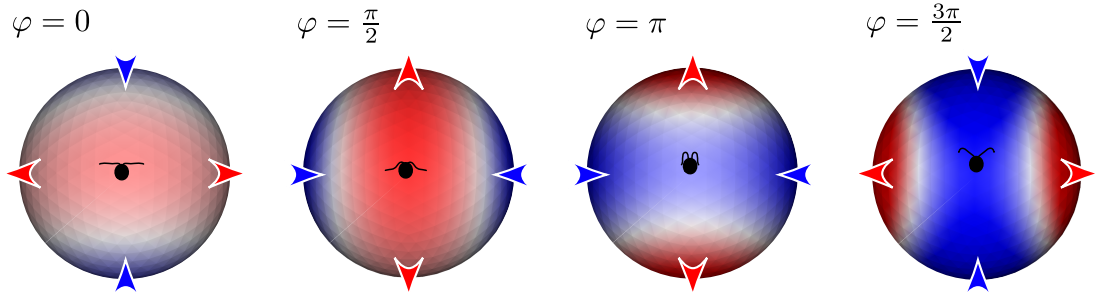


Figure 2.6: *Radial projection of the far field of a freely swimming Chlamydomonas cell.* The length of radially projected flow vectors of the far field around Chlamydomonas at a distance of $100 \mu\text{m}$ for different phases of the flagellar beat is shown. Red means outflow, away from its source, blue means inflow, towards its source, and white indicates zero radial flow. The tangential contributions are neglected but the three dimensional character of the flow is emphasized.

2.2.2 Force dipole characterization

Microswimmers do not exert forces and torques on the surrounding fluid when no external force or torque is applied. Thus, the leading order singularity of the multipole expansion of the force field exerted by the swimmer is a force dipole. The far field at distances of about $100 \mu\text{m}$ is faithfully reproduced by the second order singularity $\mathbf{u}^{(2)}$, called Stokes doublet, see the second term of equation (1.14).

$$u_k^{(2)}(\mathbf{r}, t) = \partial_i T_{jk}(\mathbf{r}) f_{ij}^{(2)}(t), \quad (2.9)$$

with the Oseen tensor T and the force dipole $\mathbf{f}^{(2)}$ from equation 1.13

$$f_{\gamma\alpha}^{(2)}(t) = \int_S dS(\mathbf{r}) r_\gamma f_\alpha(r). \quad (2.10)$$

Here, S is the surface of the swimmer and $\mathbf{f}(\mathbf{r})$ is the corresponding force surface density. We write the force dipole as a tensor $\mathbf{f}^{(2)}$ with nine components $f_{\gamma\alpha}^{(2)}$ for $\gamma, \alpha \in \{1, 2, 3\}$. Symmetries in the force dipole $\mathbf{f}^{(2)}$ due to physical and geometric constraints reduce the number of degrees of freedom from nine to three.

Physical conditions. No external torque is applied and the microswimmer itself does not exert a torque on the fluid, implying that the antisymmetric part of the dipole matrix has to vanish ($f_{ij} = f_{ji}$). Because of the incompressibility of Stokes flow, the trace of $\mathbf{f}^{(2)}$ does not result in any fluid flow. Without loss of generality, we can demand that $\mathbf{f}^{(2)}$ is a traceless symmetric tensor.

Geometric symmetry. Since the flagellar dynamics is restricted to planar beating in the $\mathbf{e}_1\mathbf{e}_2$ -plane, the surface of the swimmer is mirror symmetric to the $\mathbf{e}_1\mathbf{e}_2$ -plane, and r_3 as well as f_3 are antisymmetric in \mathbf{e}_3 and r_1 and r_2 are symmetric in \mathbf{e}_3 . Thus, (2.10) gives $f_{xz}^{(2)} = f_{yz}^{(2)} = 0$.

Since we are left with three degrees of freedom for describing the force dipole, we use a representation with the dipole strength f_s , planarity ϵ and the orientation α within the swimming plane

$$\mathbf{f}^{(2)} = f_s \mathfrak{R}^{-1}(\alpha) \left[\begin{pmatrix} 2 & 0 & 0 \\ 0 & -1 & 0 \\ 0 & 0 & -1 \end{pmatrix} + \begin{pmatrix} 0 & 0 & 0 \\ 0 & \epsilon & 0 \\ 0 & 0 & -\epsilon \end{pmatrix} \right] \mathfrak{R}(\alpha), \quad (2.11)$$

where \mathfrak{R} denotes a rotation around \mathbf{e}_3 by an angle α .

The dipole strength f_s is a direct measure for the speed of the velocity field in the direction enclosing an angle α with the swimming direction. The planarity parameter ϵ tells how in- and outflow from the $\mathbf{e}_1\mathbf{e}_2$ -plane are distributed. The planarity ϵ is confined between -3 to 3 . The higher its absolute value, the more planar the dipole flow is. For $\epsilon = 1$, the dipole plane is perpendicular to the swimming plane, for $\epsilon = -1$ the swimming plane and the dipole plane are the same. Consider now the case of $f_s > 0$ and $\alpha = 0$. Then the swimmer is pusher and there is out flow in swimming direction. For $|\epsilon| > 1$ there is outflow in an additional direction to the swimming direction. For $\epsilon = 3$ there is disk-like out flow in the swimming plane and for $\epsilon = -3$ there is ring-like outflow perpendicular to the swimming plane. Higher values of $|\epsilon|$ means that there is stronger outflow to a dimension other than the swimming direction, in which situation it is debatable, if the swimmer should still be treated as pusher, determined by the sign of f_s . Analogous interpretations are done for pullers ($f_s < 0$) swapping inflow for outflow. See figure 2.7 for a complete overview of flow signatures.

A useful quantity to define is the force dipole symmetry

$$\sigma = \frac{1 - |\epsilon|}{1 + |\epsilon|}. \quad (2.12)$$

We have $\sigma < 0 \Leftrightarrow |\epsilon| > 1$, $\sigma < -1/2 \Leftrightarrow |\epsilon| > 3$, which is used in figure 2.9 and 2.10.

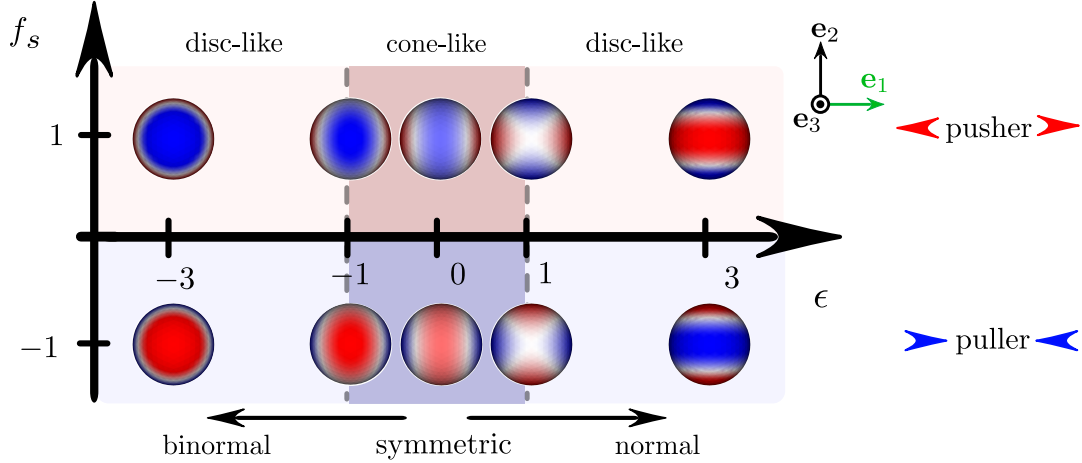


Figure 2.7: *Characterization of 3D Stokes doublet flow signatures.* The microswimmer is a pusher for $f_s > 0$ and a puller for $f_s < 0$ provided $|\epsilon| < 3$. For $\epsilon = 0$, the flow field is symmetric with respect to rotations around \mathbf{e}_1 . We then say that the swimmer has a cone-like flow signature. Larger values break that symmetry. For $1 < |\epsilon| < 3$ the signature is disc-like, which means either the swimming plane (normal) direction, or the direction perpendicular to it (binormal) has the same radial flow direction as the flow speed in swimming direction.

2.2.3 Flagellated swimmers alternate between pusher and puller

We discuss the force dipole dynamics for three different types of swimmers in the order of increasing complexity: Bacteria, Chlamydomonas and sperm cell. For all swimmers, the swimming path was determined as described in section 2.1.4 and 2.1.5 and the dipole dynamics computed with equation (2.10) and (2.11).

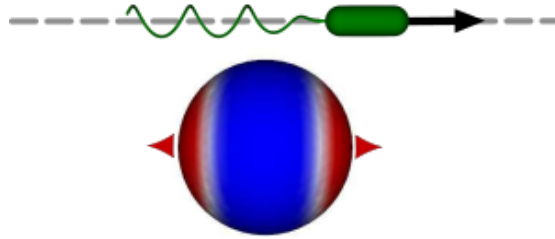


Figure 2.8: *Constant swimmer signature of a bacterium.* The bacterium exerts a constant force dipole in swimming direction, representing a symmetric pusher.

Bacterium. A particularly simple hydrodynamic force dipole signature characterizes the far field flow generated by a bacterium that propels by a single rotating bacterial flagellum. It is almost constant and consists of only small planar deformations from a symmetric pusher and does not change orientation, see figure 2.8. A bacterium with multiple flagella that are attached asymmetrically is also expected to represent a cone-like pusher with slightly larger planarity ϵ , because the main axis of the cell body

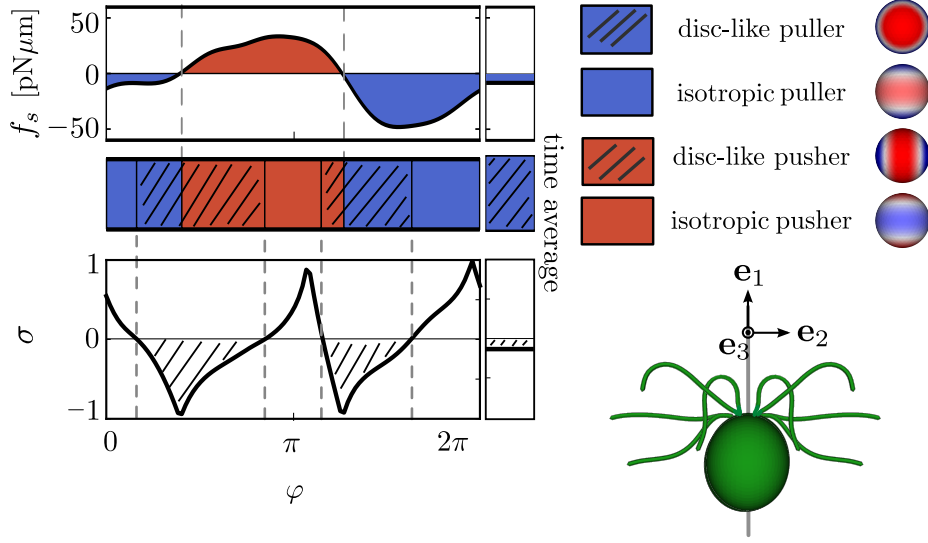


Figure 2.9: *Phase-dependent swimmer signature of a Chlamydomonas cell.* Chlamydomonas alternates between pusher- and puller-like swimming. The force dipole strength f_s oscillates and changes sign, similarly to the swimming speed, see figure 2.4. This determines if Chlamydomonas is in a pusher or puller state. The symmetry σ , equation (2.12), oscillates and passes two times extreme disc-like state, one of which binormal the other normal, see also figure 2.7.

generally rotates around the swimming direction and is not parallel to it [60].

Chlamydomonas. During the synchronous beat of Chlamydomonas, the force dipole orientation α , defined in equation (2.11), stays constant, but the dipole strength f_s varies similarly to the swimming speed. It even changes sign, which renders Chlamydomonas a pusher during the recovery beat, while being a typical representative of puller-type swimming during the power stroke. The time average of the force dipole is of puller-type character and is an order of magnitude lower as instantaneous values. The planarity is very dynamic and shows the importance of the orientation of cells when hydrodynamically interacting with each other or with boundaries. Comparing the flows, shown in figure 2.6 with the graphical representation of the terminology depicted in figure 2.7, we have, from left to right, a cone-like puller ($\varphi = 0$), a disc-like pusher ($\varphi = \frac{\pi}{2}$), a cone-like pusher ($\varphi = \pi$) and a disc-like puller ($\varphi = \frac{3\pi}{2}$). Thus, Chlamydomonas oscillates between pusher- and puller-type swimming during its beat cycle and is disc-like puller with low dipole strength in the time-average.

Sperm cell. While being similarly dynamic in dipole strength and planarity, additional complexity arises because the swimming direction of the sperm cell is already very complicated. Depending on our aim, we may choose among three different length scales for defining the mutual orientation of force dipole and swimming path. Considering the smallest scale is to express the orientation of the force dipole relative to the current orientation on the swimmers material frame Ω . For this analysis we choose the mean swimming path of the cell, which we approximate as a circular arc, connecting the

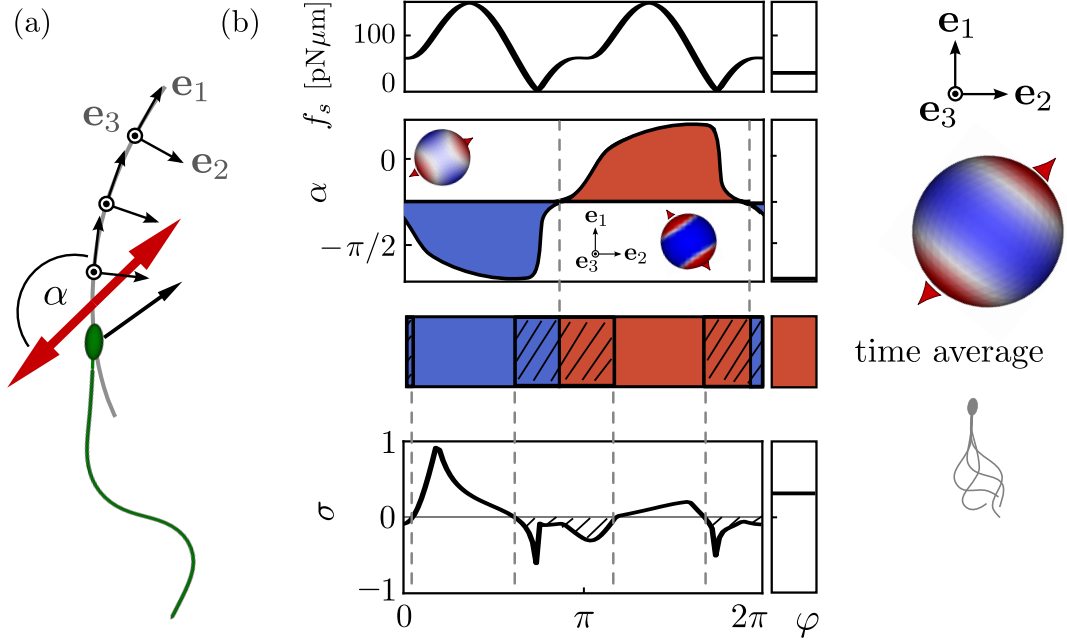


Figure 2.10: *Phase-dependent swimmer signature of a sperm cell.* (a) The sperm cell has a curved mean swimming path due to non-zero mean flagellar curvature. (b) The same quantities are shown as in figure 2.9. We dictate the relative orientation of the force dipole with respect to the swimmer orientation to be smooth. It follows that the dipole strength is always greater than zero. Thus, the swimmer signature is determined by the relative orientation. We observe that the sperm cell alternates between pusher- and puller-like swimming. The mean dipole is a cone-like pusher.

swimming directions from the beat at different points that are temporarily separated by multiples of the period $T = \frac{2\pi}{\omega}$ of the beat. For swimming of a sperm cell with a binormal component at larger time scales, we might have chosen an even larger length scale, which is the mean direction of the helical swimming path typically performed by sperm cells [38].

For a constant force dipole orientation ($\partial_t \alpha = 0$) the alternation between pusher and puller can only happen if either the strength is zero, $f_s(t_t) = 0$, at the transition time t_t , or by passing through the disc-like state with $\sigma < 0$.

2.2.4 Implications for two interacting *Chlamydomonas* cells

Results of computations of two *Chlamydomonas* cells that swim nearby are presented, briefly, for highlighting the profound consequences of the flow field oscillations on trajectories of hydrodynamically interacting microswimmers. Therefore an analogous approach was used, as described in the sections 2.1.4 and 2.1.5, but a friction matrix for multiple swimmers instead of a single swimmer was constructed, as described in appendix C.2.

Phase-dependent interactions. Hydrodynamic interactions between active elastic structures are mediated through fluid flow that is induced locally and exerts hydrodynamic friction forces at a distance. As we saw in section 2.2.1, the flow fields that is exerted by a swimming *Chlamydomonas* is dynamic and depends on the phase of its flagellar beat. Thus, hydrodynamic interactions between two *Chlamydomonas* cells depend on the respective phases, which is reflected by changing mutual velocities of the cells.

Figure 2.11 shows the time dynamics of the separation vector for three relative arrangement of two *Chlamydomonas* cells swimming in the same direction: next to each other, initially separated by $d\mathbf{e}_2$ with d being the net distance, behind each other (initial separation $d\mathbf{e}_1$) and above each other (initial separation $d\mathbf{e}_3$). A single *Chlamydomonas* would swim in \mathbf{e}_1 -direction, but generally, we observe a drag also in the mutual direction of the two swimmers. The drag position is varies within the flagellar beat, but has a much smaller net effect after full beat cycles. The relative phase difference $\varphi_L - \varphi_R$ affects the intra-beat dynamics, but coarse grained effects over a beat cycle are comparably small.

It is not shown in the figure that the mean speed of two *Chlamydomonas* cells swimming with each other in the same direction changes significantly. While two cells swimming next to each other (see configuration in figure 2.11 (a)) propel with a smaller speed than a single cell, in the other two situations (see configurations in figure 2.11 (b, c)), the mean swimming speed is increased, independent on the mutual phase difference.

Stability of relative arrangements. For two relative orientations of two *Chlamydomonas* cells, swimming against each other and swimming above each other, a perturbation analysis with respect to the mutual angle is performed, see figure 2.12. Simulations were performed with setting different initial orientations $\alpha_{1,2}$ and phases $\varphi_1 = 0$ and $\varphi_2 = \Delta\varphi$. We observe, that the stability of the mutual orientation changes with the phase difference $\Delta\varphi$.

For example, two *Chlamydomonas* cells swimming against each other with a phase difference of $\Delta\varphi = \pi$ is a stable configuration, while for all other phase differences $\Delta\varphi$ it is unstable. For $\Delta\varphi = \frac{\pi}{2}$ and $\Delta\varphi = \frac{3\pi}{2}$, the cells cross by swimming underneath each other and for $\Delta\varphi = 0$ they tend to change the configuration to the case in which the cells swim above each other. In this configuration, there is no stable orientation but a rich set of possible trajectories, depending on their mutual phase difference. For $\Delta\varphi = 0$ the cells reorientate such that they can swim away from each other. For $\Delta\varphi = \frac{3\pi}{2}$ both cells tend to swim a circular curve together on a circle with the radial direction being the mutual connection direction.

2.3 Inertial screening of oscillatory flows

While the Stokes equation for viscous flow well approximates fluid flow in the vicinity of a microswimmer, inertial effects become important at a distance for time-varying flows.

In this section, the use of the Navier Stokes equation (1.7) is motivated and the

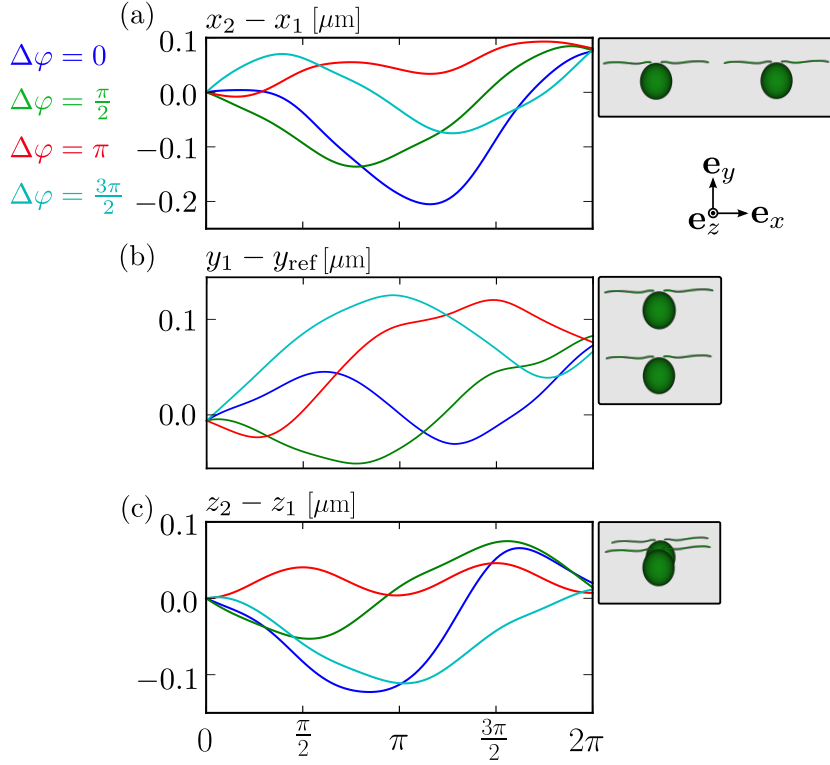


Figure 2.11: *Time dynamics of inter-swimmer distance for a pair of hydrodynamically interacting Chlamydomonas cells.* Two Chlamydomonas cells swimming together vary their distance due to hydrodynamic interactions. Three different configurations are shown: Two cells swimming next to each other (a), behind each other (b) and above each other (c). The interactions change between being attractive and repulsive during the beat. For different phase differences $\Delta\varphi$ of the flagellar beat of one cell with respect to the other interactions change accordingly. The mean change in distance is low compared to instantaneous values.

properties of its fundamental solution are described. Then this solution is applied to the dynamics of the Chlamydomonas cell and an interpretation of the screening length is given.

2.3.1 Convection and oscillatory acceleration

We discuss now the linearized Navier-Stokes equation for flow induced by a local, oscillating force dipole. We expect the dynamic acceleration $\rho\dot{\mathbf{u}}$ to play an important part, because it scales in the same way as the force dipole solution, $\propto r^{-2}$, whereas the convective acceleration $\mathbf{u} \cdot \nabla \mathbf{u}$ scales as r^{-5} and becomes negligible at a distance. With this we arrive at the linearized Navier Stokes equation, see also appendix B.

$$\rho\dot{\mathbf{u}} = -\nabla p + \Delta \mathbf{u}. \quad (2.13)$$

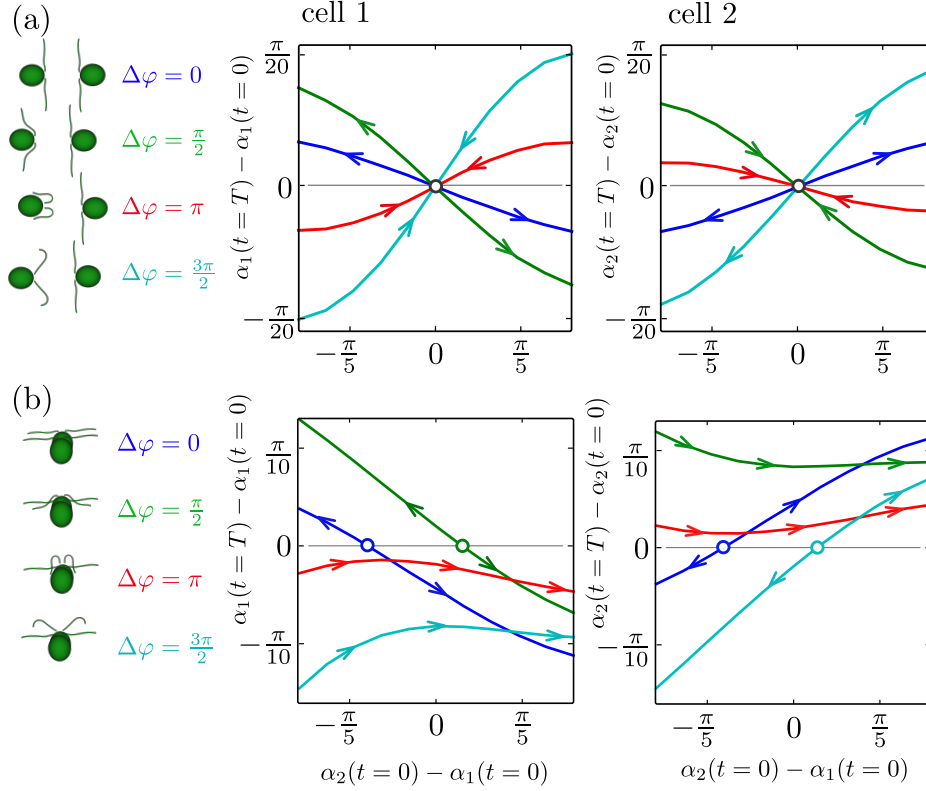


Figure 2.12: Stability diagram for the relative orientation of two *Chlamydomonas* cells in two different spatial arrangements. The swimming direction is perturbed by rotation around \mathbf{e}_2 . (a) *Chlamydomonas* are swimming in the same swimming plane with opposite swimming direction. This configuration is unstable with respect to rotation except for the case of $\Delta\varphi = \pi$. For $\Delta\varphi = 0$, the cells both change its direction in a way to end up in the configuration depicted in (b). For $\Delta\varphi = \frac{\pi}{2}$ and $\Delta\varphi = \frac{3\pi}{2}$, they pass one below the other. (b) Swimming planes are parallel and swimming is in the same direction. This configuration is very unstable. The cells might change direction into opposite directions away from each other, or both cell reorientate in the same direction, so to speak, make a turn in the same direction.

We expect that inertial effects become important at a distance δ_s from an oscillating force dipole with oscillation frequency ω_0 where

$$\delta_s = \sqrt{\frac{2\mu}{\rho\omega_0}}. \quad (2.14)$$

Next, we present the fundamental solution of (2.13).

2.3.2 The oscilet: fundamental solution of unsteady flow

The Greens function \mathcal{G} for linearized Navier Stokes flow is time dependent, or, for oscillatory motions, frequency dependent, as is the fundamental solution

$$\mathbf{u}(\mathbf{r}, t) = \int dS \mathcal{G}(\mathbf{r} - \mathbf{r}', \omega_0) \cdot \mathbf{f}(\mathbf{r}', t),$$

$$\mathcal{G}_{ij} = \frac{\mathcal{E}}{8\pi\eta r} \left[(1 - i\mathcal{D})\delta_{ij} + (1 + 3i\mathcal{D})\frac{r_i r_j}{r^2} \right], \quad (2.15)$$

$$\mathcal{E} = e^{(i-1)\frac{r}{\delta_s}},$$

$$\mathcal{D} = \left(\frac{\delta_s}{r}\right)^2 \left[\frac{1}{\mathcal{E}} - 1 - (1-i)\frac{r}{\delta_s} - (1-i)^2 \left(\frac{r}{\delta_s}\right)^2 \right].$$

For a derivation of \mathcal{G} , see appendix B. For large distances from the swimmer, we observe that the flow field propagated from the oscillating force in radial direction. For small distances much smaller than the screening length $r \ll \delta_s$, the Stokeslet is recovered, $\mathcal{G} \approx T$.

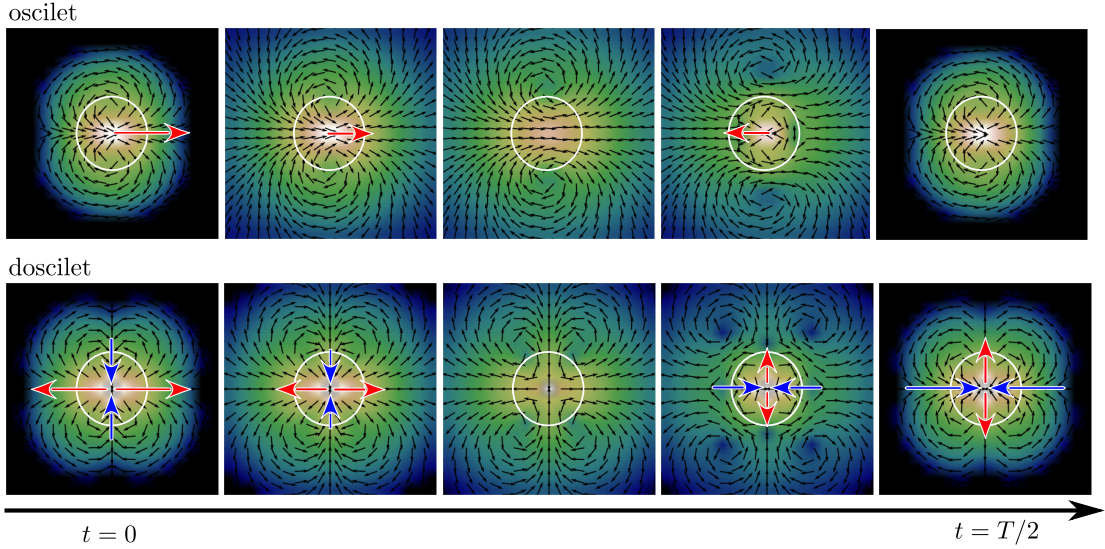


Figure 2.13: *Oscilet and doscilet dynamics.* The oscilet and doscilet are fundamental solutions of the Navier Stokes equation (2.13) and are shown for different times during half a period of the oscillating force dipole. The second half of the period looks identical with the exception that the sign of all direction of all vectors is flipped. The screening length δ_s is shown as the radius of the white circle.

2.3.3 Screening length of oscillatory flows

From equation (2.15), we can derive higher order multipole solutions for the linearized Navier Stokes equation. Note that the Green's function \mathcal{G} depends only on the difference $\mathbf{r} - \mathbf{r}'$, allowing us to exchange $\nabla \mathbf{r}$ for $-\nabla \mathbf{r}'$, see also the derivation of equation (A.5)

in the appendix. In particular, we have for an oscillating force dipole

$$\begin{aligned}\mathbf{f}^{(2)}(t) &= \mathbf{f}^{(2)}_0 e^{-i\omega t} \\ u_i^{\text{far}}(\mathbf{r}, t) &= \partial_k \mathcal{G}_{ij}(\mathbf{r}, \omega) f_{jk}^{(2)}(t).\end{aligned}\quad (2.16)$$

The dipole dynamics of the *Chlamydomonas* cell can be decomposed into Fourier modes $\mathbf{f}_n^{(2)}$, the zeroth mode is constant and corresponds to the time average $\mathbf{f}_0^{(2)}$ of the force dipole

$$\mathbf{f}^{(2)}(t) \approx \mathbf{f}_0^{(2)} + \sum_{n=1}^{n_{\text{max}}} \mathbf{f}_n^{(2)} e^{-in\omega t}.\quad (2.17)$$

The time dependent Fourier modes are propagated into the fluid with \mathcal{G} , while for the mean dipole $\mathbf{f}_0^{(2)}$ it is sufficient to propagate with the Oseen tensor, since $\mathbf{T}(\mathbf{r}) \equiv \mathcal{G}(\mathbf{r}, \omega = 0)$. We thus find

$$u_i^{\text{far}}(\mathbf{r}, t) = \partial_k T_{ij}(\mathbf{r}) f_{0,jk}^{(2)} + \sum_{n=1}^{n_{\text{max}}} \partial_k \mathcal{G}_{ij}(\mathbf{r}, n\omega) f_{n,jk}^{(2)} e^{-in\omega t}.\quad (2.18)$$

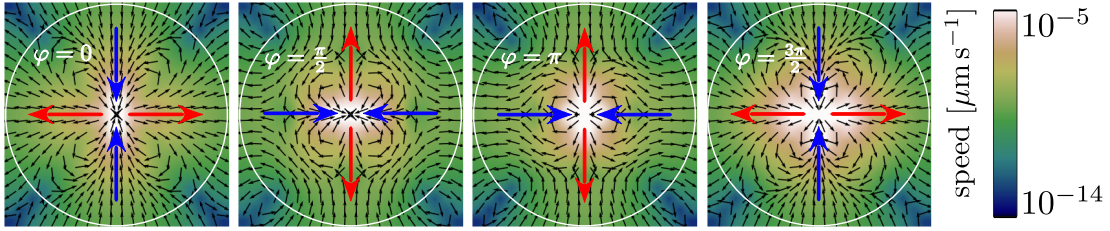


Figure 2.14: *Computed hydrodynamic mid- and far-field of Chlamydomonas.* We computed flow fields, taking into account inertial screening according to equation (2.18). We find that the flow field at a distance larger than $3\delta_s$ (white circles) is approximately static, with screening length δ_s . In contrast, inside a sphere with the same radius the flow fields oscillate.

Note that at distances $r \gg \delta_s$, the flow field is approximately static and dominated by the contribution due to the time-averaged force dipole. This static contribution corresponds to a weak puller. In the vicinity of the swimmer, however, the dynamic contribution that was shown in detail in section 2.2.3 and figures 2.9 and 2.10 dominates the static one. We find for the screening length of *Chlamydomonas* $\delta_s \approx 80 \mu\text{m}$. The distance at which the static and the dynamic component are similar in strength is at about $3\delta_s$, varying slightly with flagellar phase φ .

2.4 Energetics of flagellar self-propulsion

The flagellar beat is an active, energy consuming process, powered by the collective dynamics of molecular motors inside the flagellar axoneme. We can calculate how much

work a shape changing microswimmer exerts on the surrounding viscous fluid, thereby converting chemical energy into heat. If the shape changes are expressed as a velocity profile $\mathbf{v}(\mathbf{r})$ on a surface S , the energy dissipation rate can be written as

$$\mathcal{R} = \int_S dS(\mathbf{r}) \mathbf{f}(\mathbf{r}) \cdot \mathbf{v}(\mathbf{r}). \quad (2.19)$$

Every surface element $dS(\mathbf{r})$ has a power output of $\mathbf{f}(\mathbf{r}) \cdot \mathbf{v}(\mathbf{r})$ with hydrodynamic friction force surface density \mathbf{f} and velocity \mathbf{v} of the surface element at position \mathbf{r} . While equation (2.19) is useful for numeric calculations, we can express the dissipation rate as a volume integral as follows.

$$\mathcal{R} = \int_V dV \Phi = \int_V dV 2\mu\Delta : \Delta \quad (2.20)$$

Here, μ is the viscosity of the fluid and $\Delta_{ij} = \frac{1}{2}(\partial_i u_j + \partial_j u_i)$ is the strain rate tensor and \mathbf{u} is the flow field induced by the shape changes.

For an incompressible fluid fulfilling Stokes equation, we can exploit the mechanical energy balance $\Phi = \nabla \cdot (\mathbf{u} \cdot \mathbf{\Pi})$, with the stress tensor $\mathbf{\Pi}$ and write the dissipation rate as the following surface integral

$$\mathcal{R} = \int_V dV \nabla \cdot (\mathbf{u} \cdot \mathbf{\Pi}) = \int_S d\mathbf{S} \mathbf{v} \cdot (2\mu\Delta + p\mathbf{1}). \quad (2.21)$$

We used Gauss divergence theorem to arrive at the surface integral (2.21).

2.4.1 Impact of inertial screening on hydrodynamic dissipation

Inertial screening causes a correction to the dissipation rate (2.20) compared to the case of low Reynolds number, equation (2.21). In this section, we show that the dissipation rates that we obtain from the latter approach is a good estimate for the dissipation rate for fluids with higher oscillatory Reynolds number. Specifically, we compare the dissipation rate of the Stokeslet (1.12) with the dissipation rate of the Oscilet (2.15).

We insert the Stokeslet flow $\mathbf{u} = \mathbf{T} \cdot \mathbf{f}_0$ induced by a point force with magnitude \mathbf{f}_0 and Oseen tensor \mathbf{T} (1.11) into equation (2.21) for evaluating the strain Δ and insert the fundamental solution for the pressure p . Integrating the integral from an inner radius R_0 to infinity results in a singular dissipation rate

$$\mathcal{R} = \frac{|\mathbf{f}_0|^2}{4\pi\mu R_0}. \quad (2.22)$$

We can use equation (2.20) to compute the hydrodynamic dissipation induced by an oscillating force monopole if the linearized Navier Stokes equation is used. Inserting an Oscilet of strength $f_0 \cos(\omega t)$, we find an oscillating rate of hydrodynamic dissipation outside a spherical cut-off region of radius R_0 centered around the oscilet

$$\mathcal{R} = \frac{f_0^2 \cos^2(\omega t)}{4\pi\mu} \left(\frac{1}{R_0} - \frac{1}{R_1} \right) + \mathcal{O}(R_0/R_1)^2, \quad (2.23)$$

where $R_1 = \frac{6}{5}\delta$. For the limit $R_1 \rightarrow \infty$ the integral (2.22) is reproduced, meaning that it is the same as the viscous dissipation rate for a Stokeslet $f_0 \cos(\omega t)$ between $R_0 \leq r \leq R_1$. We conclude that we can use Stokes flow for calculating hydrodynamic dissipation rates provided $\delta_s \gg L$ where L denotes a typical size of the swimmer.

2.4.2 Case study: the green alga *Chlamydomonas*

Using equation (2.15) we compute the dissipation rate of a swimming *Chlamydomonas* cell. We also compute the dissipation rate of the leading order singularity. Both rates are function of the flagellar phase as depicted in figure 2.15.

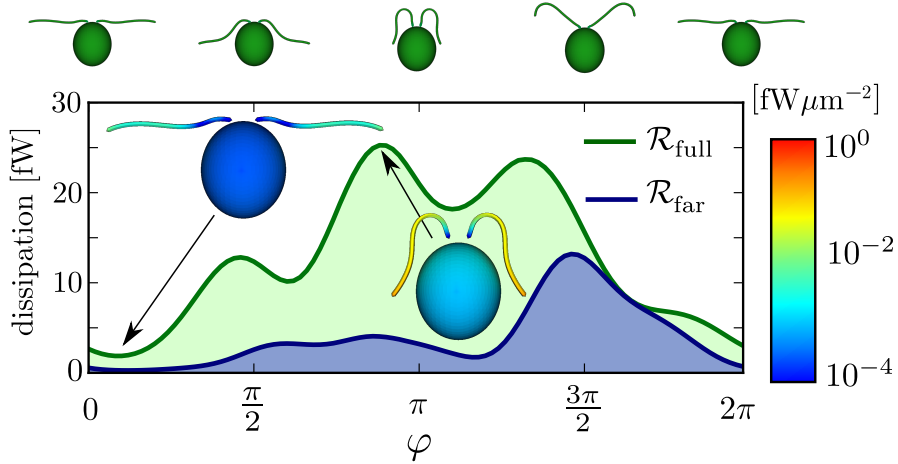


Figure 2.15: *Phase dependent dissipation rate.* The rate at which energy is dissipated into the fluid is phase-dependent with a minimum during the power stroke and a maximum during the recovery stroke. The rate at which the respective force dipole dissipates energy into the medium has a different characteristics. We ascribe this to the high local stresses occurring due to the shear flows between cell body and flagellum, which is not captured by the far field that is characterized by the force dipole. The insets show the surface density of the dissipation rate in color code.

The total dissipation rate has its maximum during the recovery stroke of the flagellar beat, where flagella are closest to the cell body and cause very large strain rates. Those large gradients of the flow field are not present in the flows that are generated by the force dipole. The maximal dissipation rate due to the force dipole dynamics happens during the transition from the recovery stroke to the power stroke, in which flagella move away from each other into a stretched out state.

2.4.3 Discussion: evolutionary optimization and the number of molecular motors

At low Reynolds number, the shape of the swimming trajectory $\mathbf{r}(t)$ is independent of the time parameterization of the swimming stroke. Thus, a re-parameterization changes the total hydrodynamic dissipation, but does not change the net displacement after one

swimming stroke. In particular, we can re-parameterize the flagellar phase as $\varphi \rightarrow \varphi'$ with $\partial\varphi'/\partial t = \omega$ such as to minimize $\oint \mathcal{R}$. Constant dissipation rates are generally not observed biological microswimmers [70], see also figure 2.15. We conclude that energy minimization is not the only evolutionary optimization criterion. Of course, a general cost function that is optimized may depend on many criteria, such as swimming speed, biomixing, phototactic success or synchronization of flagella.

The total amount of energy that is dissipated into the fluid corresponds to the chemical energy that is provided by ≈ 3.000 ATP molecules, which is much less than the number of molecular motors inside the axoneme (≈ 30.000 [94]). This means that, either not all molecular motors consume an ATP molecule during one beat cycle, or the efficiency of energy conversion from chemical energy into mechanical work performed by the beating flagellum is on the order of 10 %.

A more direct treatment and estimation of the energy efficiency is given in section 3.2.3 and 3.3.2.

2.5 Summary

We investigated the flow field that is exerted by a shape-changing microswimmer that swims free from external forces or torques. A dynamic flow field is induced with an intricate structure in the vicinity of the swimmer. The far-field oscillates but has a much simpler, dipolar structure. Specifically, the flow signature of a *Chlamydomonas* cell and a sperm cell alternates between pusher and puller. The strength of the time average of the force dipole of *Chlamydomonas* is an order of magnitude smaller than instantaneous values, which makes *Chlamydomonas* an approximately neutral swimmer.

The fast alternations of the dipolar far field can not happen instantaneously. Thus, inertial effects have to be attributed by retaining the unsteady flow term of the Navier Stokes equation. Inertial effects attenuate oscillating flows at a distance, given by an inertial screening length $\delta_s = \sqrt{2\mu/\rho\omega}$.

Interestingly, we found that measured flagellar beat patterns do not minimize total hydrodynamic dissipation for a fixed net displacement during one swimming stroke. The work performed by the beating flagella on the fluid is one order of magnitude lower than the chemical energy release by hydrolysis of ATP, assuming that every molecular motor makes one step per beat.

The load-response of the flagellar beat

Synchronization in collections of cilia and flagella by hydrodynamic coupling requires that the speed of the flagellar beat changes in response to forces, such as hydrodynamic friction forces. We combine analysis of experimental data and theory to precisely quantify how external fluid flow changes shape and speed of the flagellar beat, using Chlamydomonas as model system.

Chapter overview. First, the experiment, that is performed by our collaborators and how we extracted data from it, is described. Second, I present an effective theory of the flagellar beat that is independent from microscopic details and is calibrated by macroscopic, experimental quantities. Lastly, the findings of experimental results for imposed external flows are compared to theoretical predictions.

The content of this chapter is mostly covered by a publication [71]. Experiments were conducted by Christian Ruloff, while the author contributed to the design and the implementation of the flagellar tracking algorithm. The author performed data analysis, developed and implemented the theoretical description.

3.1 *Experimental collaboration: flagellated swimmers exposed to flows*

In this section, the experiment for inspecting hydrodynamic load-response is described. There, a Chlamydomonas cell is clamped and exposed to external homogeneous flow. First, the experimental setup is described and the flow profile within the micro-fluidic chamber is presented. The experiment was designed and realized by Christian Ruloff and is briefly described for the sake of completeness. Then, we demonstrate how the video-microscopy data of flagellar beating was pre-processed and flagellar shapes tracked. The

tracking algorithm was designed and implemented collaboratively by Christian Ruloff and the author. Last, the limit cycle reconstruction is presented. It leads to the relevant quantities that are used in our theory, which is illustrated in the next section 3.2.

3.1.1 Description of the experimental setup

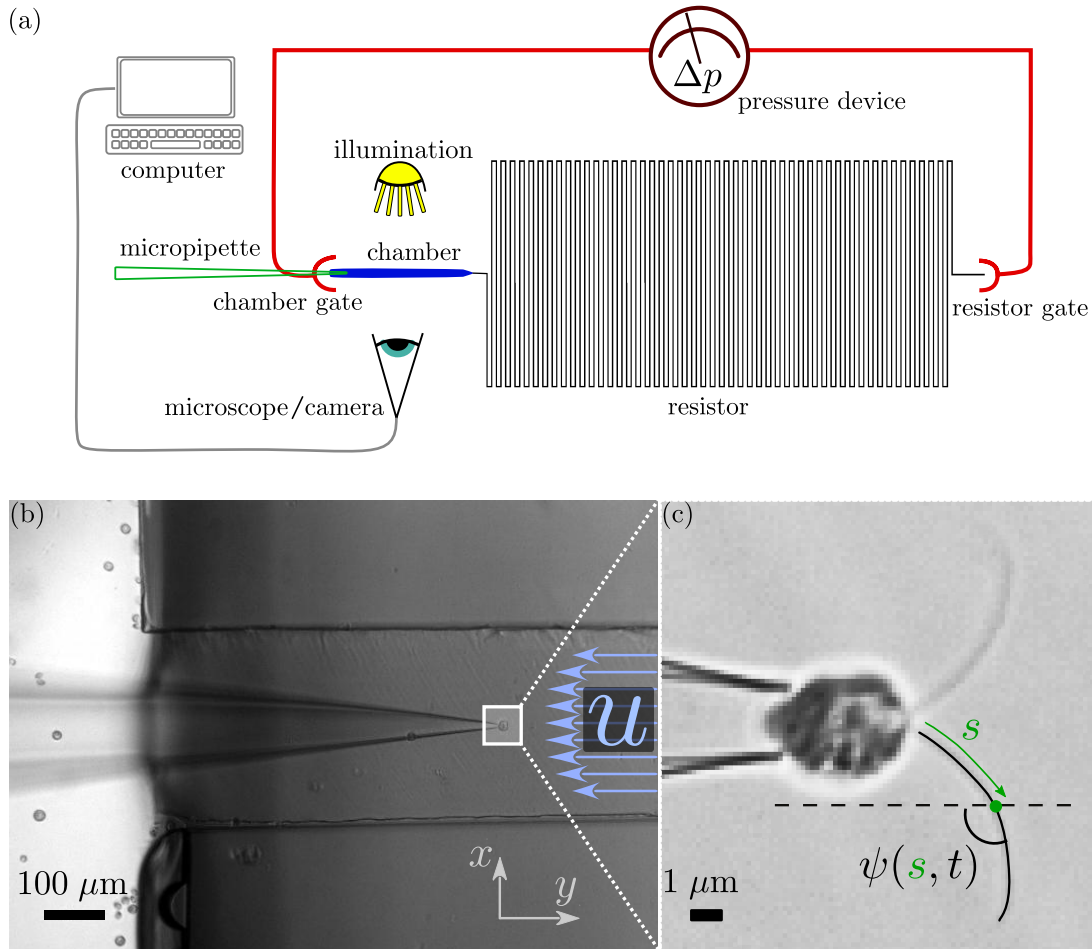


Figure 3.1: *Experimental setup.* (a) Experimental setup with pressure device and micro-fluidic device, consisting of chamber and resistor. The *Chlamydomonas* cell is held within the flow-chamber with a micro-pipette, which is illuminated and recorded. (b) Picture of flow-chamber with micro-pipette used to hold a single *Chlamydomonas* cell. External flows are Poisseuille flows and can be approximated by homogeneous flows in the vicinity of the cell. (c) Movie still of high-speed video-micrographs of flagellar beating. The flagella of a clamped *Chlamydomonas* cell are clearly visible. Micrographs (b), (c) were taken by Christian Ruloff.

The experimental setup mainly consists of a microscope and a camera, a pressure device and a micro-fluidic device, which itself consists of a resistor pipeline and a micro-fluidic chamber. When a pressure difference is applied between the resistor gate and the chamber gate, a flow rate is induced, which depends on the geometry of the resistor

and the cross sectional area of the flow chamber. It is particularly sensitive to changes to the resistor's smaller dimensions. The chamber has a rectangular cross-section with dimensions $(55 \pm 5) \mu\text{m} \times (50 \pm 2) \mu\text{m}$. Since the resistor chamber is very long ($\approx 70\text{cm}$), inertial effects cannot be neglected while tuning the pressure, and waiting times have to be included during the measurements for letting the induced flows equilibrate.

A micro-pipette made of glass with radius $\approx 1 \mu\text{m}$ at the tip is used to clamp the Chlamydomonas cell inside the micro-fluidic chamber. The size of the chambers that were used have the size $(210 \pm 5) \mu\text{m} \times (50 \pm 2) \mu\text{m} \times (\approx 3500) \mu\text{m}$. Poiseuille flow is induced inside the chamber, but in the vicinity of the Chlamydomonas, homogeneous flow can be assumed, because the cell is much smaller than the channel height, see figure 3.2. This is important for being able to apply the theoretic description developed in section 3.2.

Chlamydomonas cells are positioned right in the center of the micro-fluidic chamber. Its orientation is set such that one of the two flagella is in the focal plane of the high speed camera. This can only be done approximately, since the flagellar beat itself is not entirely planar, with small contributions in the third dimension. Also, it is problematic to obtain images of good quality for both flagella, because their beating planes are not perfectly coplanar. The Chlamydomonas is illuminated with light with a luminance of $8,000 \text{ W/m}^2$, which means that a light power of 0.2 nW reaches the cell.

Experimental protocols. Videos are taken from measurements, in which a Chlamydomonas cell is first exposed to zero external flow, which is then stepwise increased until a maximum fluid flow speed is reached (this is called up-sweep) and then again stepwise decreased until zero flow speed (down-sweep). After a change of the external flow rate, the flow is equilibrated until steady flow is achieved. The, the sequences during constant flow rates are recorded. The maximum flow speed for the stalling measurement, see section 3.3.3, is about 10 mm s^{-1} and about 140 sequences with about 1000 frames each are recorded. For the other analysis, the maximum flow is about 2 mm s^{-1} with 16 sequences of about 10,000 frames each.

3.1.2 *Computed flow profile in the micro-fluidic device*

The analysis of the experimental data relies on the assumption that the flow in the vicinity of the cell is homogeneous. To test this assumption we performed hydrodynamic simulations, in which a rectangular box is placed in a fluid with constant fluid flow in y -direction at two surfaces at $z_0 = 0$ and $z_1 = 260 \mu\text{m}$. A sphere with a radius comparable to the size of Chlamydomonas is placed inside, see figure 3.2 (a). Figure 3.2 (b) shows the flow profile for cross sections at different y_i . We conclude that in the surrounding of flagella, the flow field is indeed homogeneous to very good approximation.

3.1.3 *Image processing and flagellar tracking*

It is presented first, how the recorded images are processed to enhance the visibility of flagella and reduce the visibility of the cell body. Then the flagellar tracking algorithm is explained. Last, we present an objective criterion to select high-quality data sets for

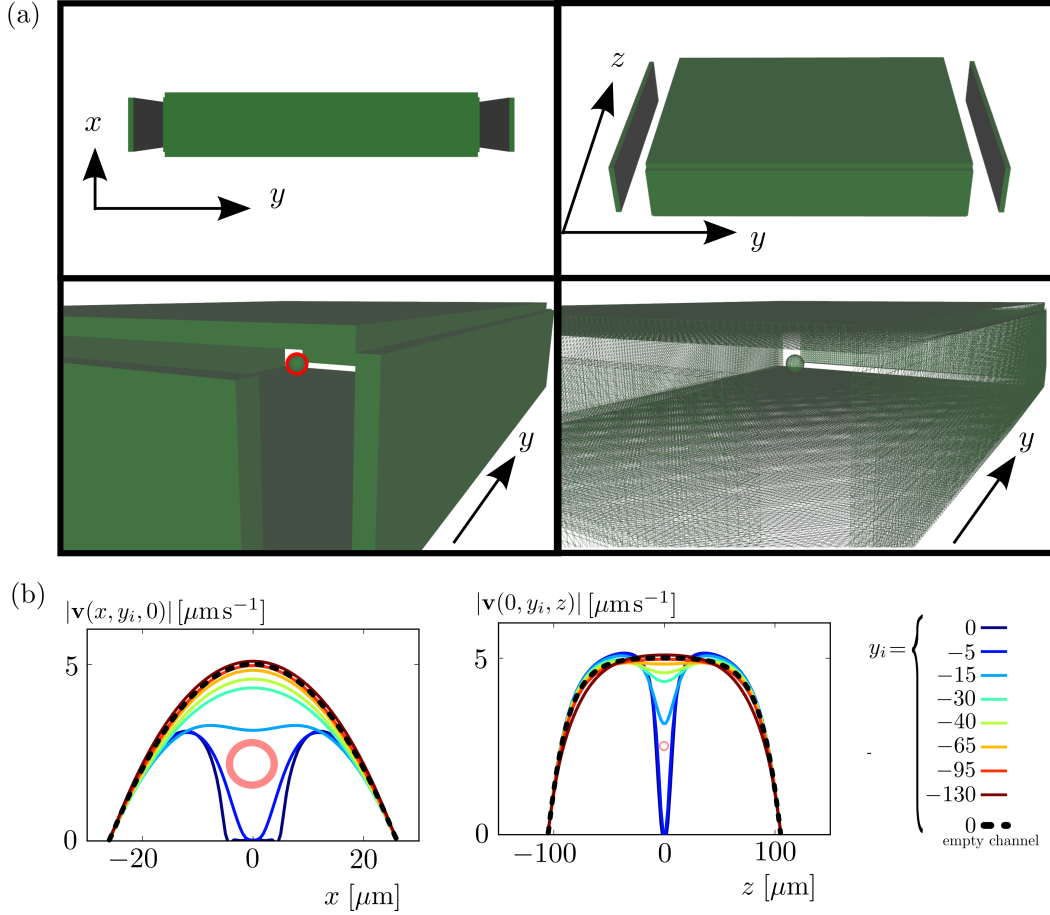


Figure 3.2: *Flow through the micro-fluidic chamber.* (a) In the experiments, the Chlamydomonas held inside a box with size $210\mu\text{m} \times 50\mu\text{m} \times 3500\mu\text{m}$. External flow can be imposed in y -direction, which is the swimming direction. This is virtualized. The bottom images also show a sphere of similar size as Chlamydomonas inside the virtualized chamber. (b) The computed flow-field in the surrounding of Chlamydomonas shown during the recovery stroke, while an external flow with flow speed 0.2mm s^{-1} is imposed. The speed of the flagellar tip is about 1mm s^{-1} . (c) The computed flow profile along the shortest dimension has the form of Poiseuille flow if the Chlamydomonas is not inside the chamber and for values of y at a distance from the cell. Along the z axis, there is a plateau in the profile without the cell, which is approximately homogeneous. The dips in the colored curves are due to the cell body in the interior of the flow-chamber.

further analysis.

Image pre-processing. With the experimental setup, described above our experimental partners provided videos from the experiments. A typical frame for a cell during power and recovery stroke is shown in figure 3.3 (a). For removing the static parts of the images, like the cell body and dirt on the camera lenses or on the surface of the channel, a background subtraction was performed, which means that the time average of the intensity of the micro-graph is subtracted from the original images.

A nematic filter is used, which is explained in the appendix D.1. It can be understood

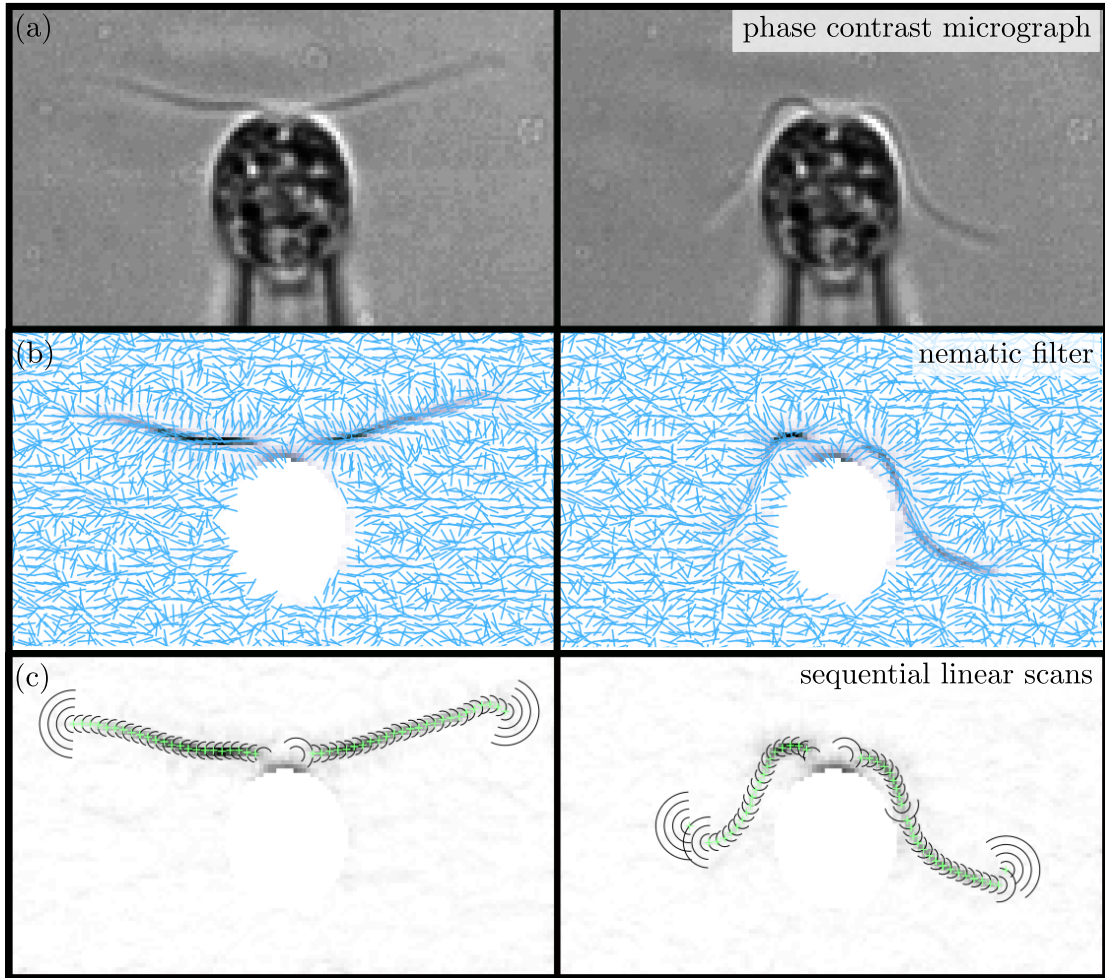


Figure 3.3: *The main steps of the flagellar tracking algorithm.* For a typical cell two phases are shown, one of which during the power stroke (left) and the other one during the recovery stroke (right). (a) The recorded image as is. (b) The background image, which is the mean over multiple frames, was subtracted and the nematic filter is applied. The nematic strength is shown as intensity (white: low intensity, black: high intensity). Note that the cell body was cut out. The nematic orientation is shown as blue nemats, which are nicely oriented along the flagella. (c) The arc-scans are shown as black half-circles and intensity maxima are marked with turquoise cross. Note that if no tracking point could be established, another scan with doubled radius was performed. Micrographs (a) were taken by Christian Ruloff.

as an edge detection algorithm, pronouncing line segments by returning an intensity field $I(x, y)$ with increased intensity at edges. It also returns a direction field $d(x, y)$, which can be used for initial guesses on the direction of the flagellar tracking. Figure 3.3 (b) shows the direction field as blue lines and the intensity field in the background.

Flagellar tracking. The aim of the flagellar tracking algorithm is to obtain two dimensional coordinates along the flagellum, sorted by their arc-length position.

The starting point \mathbf{r}_0 of the flagellum to be tracked is chosen manually for all frames

in a video sequence, since it stays at a fixed position and can be reused for each frame of the video. Then an arc-scan is performed with a radius $r_s = 2 \text{ px}$ around the origin \mathbf{r}_0 with an opening angle of $\delta = \frac{\pi}{2}$ in the direction, that is determined by the nematic direction field $d(x_0, y_0)$. The arc-scan results in an intensity profile $I_c(\alpha)$ along the circular arc. We determine the angle α_0 at which the intensity has its maximum.

We detect a flagellum if the maximum intensity exceeds a certain threshold value I_t , such that $I_c(\alpha_0) > I_t$. While this is a necessary criterion, it is not sufficient. Consider a highly reflective dirt particle in a dark environment, the arc scan would indeed show a large value for I , but the integrated intensity over the arc, would be very low compared to a detected flagellum. We demand the additional acceptance criterion to be that the prominence of the maximum must be large enough. If both criteria are fulfilled, the tracking point is accepted and it will be used as the origin of the next arc-scan if the total length l_f that is tracked so far does not exceed a certain length, which corresponds to a maximal flagellar length. If the maximum length l_{\max} is reached, flagellar tracking is done. If the tracking point is rejected, the arc-scan radius r_s is increased and the arc-scan is repeated, if the arc-scan radius does not exceed a certain arc-scan radius threshold.

The whole procedure is applied recursively, until it is stopped by one of the threshold criteria. In Figure 3.4 a flow chart shows the tracking process described and figure 3.3 (c) shows all tracking points and arc-scan contours for a specific flagellar shape at one instance of time.

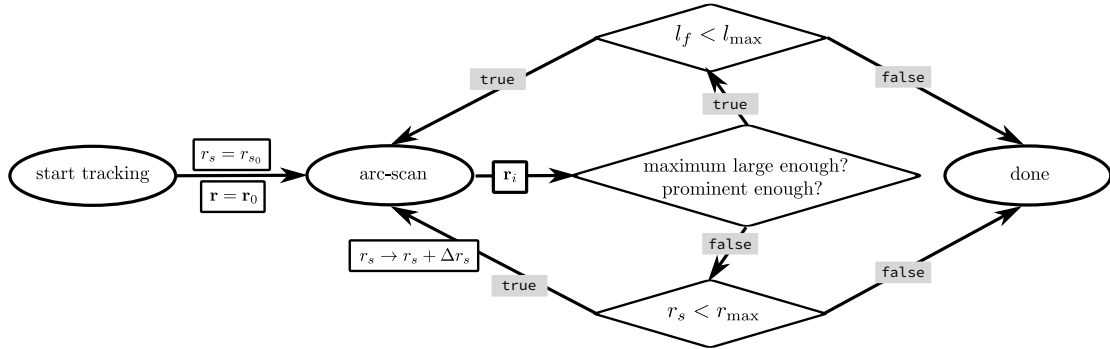


Figure 3.4: *Flow-diagram of flagellar tracking algorithm.* Starting at the flagellar anchoring at the cell body, arc-scans are performed until one of two threshold criteria are fulfilled, that decide if a flagellum is at the current position. Rectangular boxes represent data, elliptic boxes represent processes, the rhombs are branching points. For details see main text in section 3.1.3

Selection of data sets. Before we actually decompose the tracked flagellar shapes into shape modes as described in the next section, we apply two more criteria onto our high-quality data sets for selecting data sets objectively. We define the length of a cell as the median of the tracking lengths of all frames during the reference sequence. If the number of frames of a sequence that exhibit a flagellum shorter than 80% of the flagellar length must be less than 20% of all frames. If more than ten valid sequences are left, the cell is used for all later analysis. With that procedure, we obtained data of

six different flagella of corresponding cells.

3.1.4 Mode decomposition and limit-cycle reconstruction

In this section, the flagellar beat is decomposed into shape modes. Thus, the flagellar beat can be represented as a trajectory in an abstract phase space with shape modes as basis vectors. The trajectories form closed loops, representing stable limit cycles.

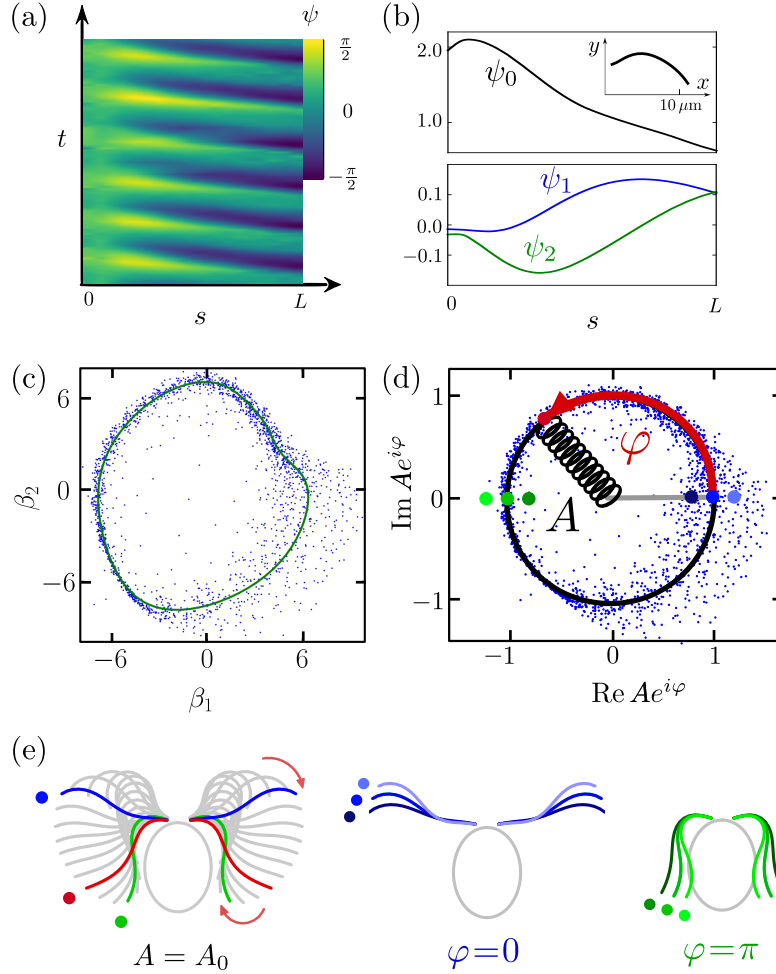


Figure 3.5: *Limit cycle construction.* (a) Flagellar shapes are represented by their tangent angle profiles ψ , see figure 3.1. A typical kymograph of $\psi(s, t)$ is shown. (b) The mean tangent angle $\psi_0 = \langle \psi \rangle_t$ is shown and the shape modes ψ_0 and ψ_1 that are obtained from principal component analysis. The gray insets show the respective flagellar shapes. (c) Fitting the measured shapes ψ onto shape modes ψ_i results in shape scores β_i . The first two scores are plotted against each other. A periodic average flagellar beat is obtained by fitting the scores onto periodic functions. (d) All data points as well as the periodic fit are rescaled to the unit circle. (e) Reconstructed shapes are shown for points on the limit cycle as well as for perturbed amplitudes. The color corresponds to the respective color in (d). Video-microscopy data was provided by Christian Ruloff.

The tracking algorithm, described in section 3.1.3, delivers Cartesian coordinates

that can be used to obtain the tangent angle representation from equation (2.1). This periodic signal is shown in figure 3.5 (a). For the reference case of a clamped cell with zero external flow, the mean bending $\psi_0 = \langle \psi(s_i, t_j) \rangle_t$ is calculated. The principal component analysis, which is described in appendix D.2, is applied to $\psi(s_i, t_j) - \psi_0$ resulting in arc length s dependent shape modes $\psi_i(s_i)$ and time t dependent scores $\beta_i(t_j)$. Thus, the flagellar shape at a specific time can be represented as a N_s dimensional vector $\boldsymbol{\beta} = \{\beta_1, \beta_2, \dots, \beta_{N_s}\}$ of an abstract phase space, where N_s is the number of tracking points along the flagellar length. The vectors $\{\boldsymbol{\beta}(t_j)\}_{j=1 \dots N_t}$ (N_t is the number of frame of the video) are distributed as a point cloud with largest extension along the first axis ψ_1 , and decreasing extensions with higher modes ψ_j . Considering just the first two shape modes is enough to faithfully reproduce the measured tangent angle description of flagellar shapes

$$\psi(s, t) \approx \psi_0(s) + \beta_1(t)\psi_1(s) + \beta_2(t)\psi_2(s). \quad (3.1)$$

Also, deformations that occur due to external perturbations are well represented, see appendix D.3 for a quantification. Figure 3.5 (c) shows the two dimensional projections $P(\boldsymbol{\beta}) = \{\beta_1, \beta_2, 0, \dots, 0\}$ of $\boldsymbol{\beta}$ (blue dots are projections of measured shapes).

The scores are typically periodic signals, which we can approximate by periodic score functions $\bar{\beta}_i(\theta)$, see figure 3.5 (d), black circle. We call θ a protophase, which generally is different from phase φ , which is uniquely defined by the property of increasing constantly with time, $\partial_t \varphi = \omega$ with the frequency ω_0 of the flagellar beat. We use a procedure for reconstructing the phase φ from the protophase θ [72]

$$\varphi = \theta + \sum_{n \neq 0} \frac{S_n}{in} \left(e^{in\theta} - 1 \right). \quad (3.2)$$

S_n are the Fourier coefficients of the probability density $g(\theta)$ of the protophase θ

$$S_n = \frac{1}{2\pi} \int_0^{2\pi} d\theta g(\theta) e^{-in\theta}, \quad (3.3)$$

$$g(\theta) = \sum_n S_n e^{in\theta} = 2\pi \langle (\delta(\Theta(t) - \theta)) \rangle.$$

Additionally, we are able to express the shapes by the previously defined phase φ and the norm of a shape vector, which we call raw amplitude $A' = |\boldsymbol{\beta}|$. Figure 3.5 (d) shows the limit cycle that is normalized by the amplitude, thus we define a normalized instantaneous amplitude of the flagellar beat

$$A_j = \boldsymbol{\beta}(t_j)/A'(\varphi). \quad (3.4)$$

With this, we arrived at a description of the flagellar shape that depends on just two parameters. Additionally to the phase that represents the oscillatory nature of the reconstructed limit cycle of the flagellar beat, the amplitude highlights deformations of flagella.

3.1.5 Changes of limit-cycle dynamics: deformation, translation, acceleration

The flagellar beat is described as a limit cycle that changes due to changes of the environment. We call the effect of changes to the limit-cycle dynamics due to external forces load response. Specifically we investigate the situation of constant external load in the form of homogeneous external flow u . The time average of the flagellar shape is mapped to the state space point inside the limit cycle. In the case of the reference cell, with constant amplitude A and phase speed ω , the mean shape corresponds to the geometric center. We distinguish three distinct shape change contributions, which are depicted in figure 3.6. Deformations of the limit cycle due to changes in the amplitude can be separated into a mean shape change and deformations that do not affect the average shape. Phase speed changes also lead to changes in the time averaged shape.

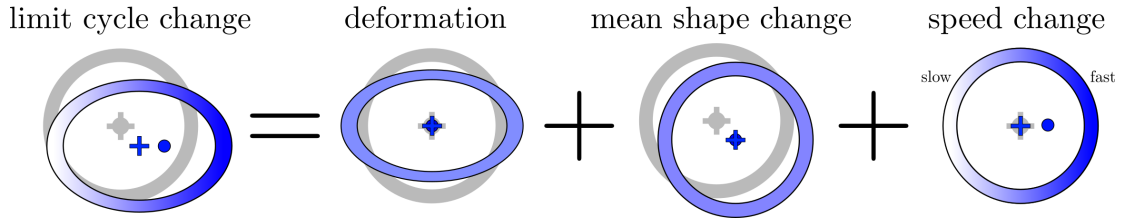


Figure 3.6: *Three contributions to limit cycle changes.* A limit cycle is depicted as a circle, its geometric center is represented by a cross and the time averaged state is shown as a small circle. The gray objects represent a reference limit cycle, whose geometric center coincides with its time average. The limit cycle changes can be separated into three distinct contributions. There are phase dependent amplitude deformations (\odot) that sum up to zero. the mean shape can change (\ominus). The phase speed can change differently at different phases of the limit cycle (\oplus), which also changes the time average.

Generally, we can describe the load response due to external flow u as a flow dependent shape $\psi(s, \varphi; u)$. We choose to represent the change due to load-dependent score functions $\beta_i(\varphi; u)$, which allows us to recover all three limit-cycle changes depicted in figure 3.6. We hold the modes $\psi_i, i \in \{0, 1, 2\}$ independent of the load u , for being able to compare the analysis of the cells for different external loads u .

If we chose to subtract the mean shape for each external flow condition individually, information about changes of the instantaneous phase speed would get lost, since it contributes essentially to the mean shape. To retain the phase speed changes one could use the phase mean tangent angle $\langle \psi(s, t(\varphi)) \rangle_\varphi$. The artefacts that remain on the amplitude changes are negligible compared to its load-response, when using fixed ψ_0 .

As we choose to fit data of sequences onto a fixed set of modes, we assure that there is no phase ambiguity, since it is defined in terms of the two major principle modes ψ_1 and ψ_2 , see equation (3.1).

We estimate that about 90% of the variance of the flagellar beat is preserved for all the flagellar reference datasets that we use for our analysis. About 80% of the changes due to external flow perturbations can be captured. See, appendix, section D.3 for the estimation.

3.2 An effective theory of flagellar oscillations

In this section, we will describe the theoretical description of flagellar swimming in terms of generalized coordinates in the framework of Lagrange mechanics of dissipative systems. First, a force balance between active and passive forces is shown, which is the basis for the dynamical equations. Then the passive dissipative forces are presented, which are due to realistic hydrodynamic calculations and internal friction. The experimental data of the reference sequence, which is the sequence at which no external flow was imposed, is used for calculating active driving forces. Next, the stability of the limit cycle description is illustrated and an elastic amplitude spring force is derived. In the last section, we present the complete set of equations that allows us to numerically determine the dynamics of flagellar beating.

This description is a generalization of a previous theory of flagellar beating [41], by introducing a second degree of freedom for describing the limit cycle dynamics, namely, the amplitude, and considering internal friction.

Numerical results are shown for flagellar shape data from one specific cell. In section 3.3.2, we show that the results are robust under change of the flagellar waveform dataset, though, see figure 3.10.

3.2.1 A balance of generalized forces

The perfectly symmetrically beating *Chlamydomonas* with a planar flagellar beat can be described by three degrees of freedom. We assume that its flagella are identical, such that there is one phase φ and one amplitude A as they are defined in section 3.1.4. This description is analogous to a Hopf oscillator, which is presented in section 5.1. The cell's position is described by the cell body center position y along the long axis of the ellipsoidal cell body, which is the swimming direction. The entire state is described by the generalized coordinate $\mathbf{q} = (\varphi, A, y)$ and its velocity is $\dot{\mathbf{q}} = (\dot{\varphi}, \dot{A}, \dot{y})$. Conjugate forces \mathbf{P} are defined as $P_i = \partial_i \mathcal{R}$ with the energy dissipation rate $\mathcal{R} = \mathbf{P} \cdot \dot{\mathbf{q}} = P_\varphi \dot{\varphi} + P_A \dot{A} + P_y \dot{y}$.

The reference sequence is taken from a clamped cell with zero external flow. By construction, it has constant amplitude and beats with constant angular frequency ω . For later reference we write its dynamics as

$$\dot{\mathbf{q}}^{\text{ref}} = (\omega, 0, 0). \quad (3.5)$$

The dissipation rate of the reference cell is just $\mathcal{R} = P_\varphi \omega$, which implies that the driving force is proportional to the dissipated energy in this case.

The active as well as passive forces have units of generalized forces. We can obtain the equations of motion from a generalized force balance, where active forces \mathbf{Q} are balanced by passive forces \mathbf{P}

$$\mathbf{Q} = -\mathbf{P}. \quad (3.6)$$

In the following subsections, expressions for \mathbf{Q} and \mathbf{P} are derived. The passive forces

comprise both hydrodynamic friction forces and intra-flagellar friction forces and the active forces are calibrated with experimental data.

3.2.2 Hydrodynamic friction in generalized coordinates

Due to the linearity of the Stokes equation (1.10) the relation of generalized velocities $\dot{\mathbf{q}}$ to conjugate hydrodynamic friction forces $\mathbf{P}^{(h)}$ is linear and is expressed as the generalized hydrodynamic friction matrix $\mathbf{\Gamma}^{(h)}$

$$\mathbf{P}^{(h)} = \mathbf{\Gamma}^{(h)} \cdot \dot{\mathbf{q}}. \quad (3.7)$$

The friction matrix is calculated for 20 equidistant phases $\varphi_i \in [0, 2\pi)$ and 10 equidistant amplitudes $A_i \in [0.8, 1.2]$ and saved for later use as a lookup table in dynamical simulations. In appendix C.3 a recipe for calculating general friction matrices is given. For each flagellar waveform dataset, we compute a different lookup table. Physically, the friction matrix is a 3×3 -matrix with each component being a function of two variables. It is periodic in the phase φ and quadratic in the amplitude A . The quadratic dependency is not physically constrained but represents a heuristic approximation. This lookup table is used to fit a function fulfilling the just mentioned properties.

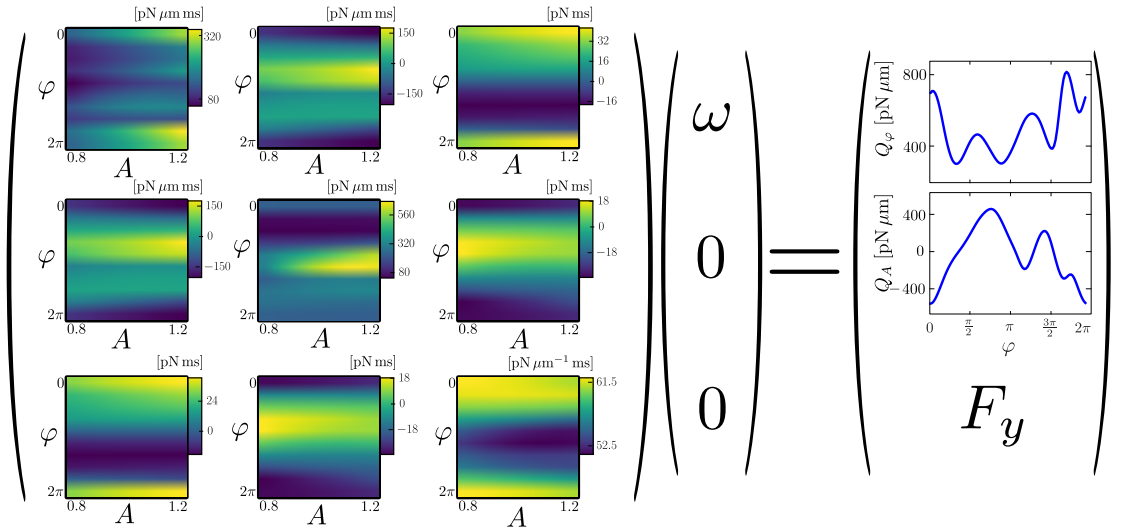


Figure 3.7: *Generalized friction matrix and generalized forces.* The friction matrix depends on the state of the flagella of *Chlamydomonas* which is given by its phase φ and its amplitude A . Some interesting properties of the friction matrix are discussed in the main text in section 3.2.2. Multiplying it with the reference state speed (3.5) gives the generalized forces Q_φ and Q_A that drive the beat. Note that Q_φ is always positive and Q_A can be positive as well as negative. Numerical values are shown for $\eta = 0.2$.

For a specific flagellar waveform dataset, the state dependence of the friction matrix is shown in figure 3.7. Note that the friction matrix is symmetric, which can be seen in equation (C.7). Other interesting properties are, e.g. that the component Γ_{yy} is approximately independent of flagellar phases, i.e. the friction coefficient for translational

motion is dominated by the passive cell body. The component $\Gamma_{\varphi y}$ changes sign. It is positive during the power stroke ($\varphi \approx 0$), meaning that phase propagation has a positive effect on the translational force, and negative during the recovery stroke ($\varphi \approx \pi$), meaning a negative translational force for positive phase propagation. Another interesting property that may have an effect on the synchronization strength of a coupled oscillator, that can be read directly from the friction matrix is non-isochrony. The phase friction $\Gamma_{\varphi\varphi}$ is larger for larger values of the amplitude A , see also section 3.3.4.

3.2.3 Intra-flagellar friction

The dissipative processes inside the flagellum are modeled with the help of the chemical energy conversion efficiency

$$\eta = \frac{E^{(h)}}{E^{\text{tot}}} \quad (3.8)$$

as the ratio of hydrodynamically dissipated energy $E^{(h)} = \oint \mathcal{R}^{(h)}$ against $E^{\text{tot}} = E^{(h)} + E^{(i)}$ that is provided by ATP hydrolysis by molecular motors against the hydrodynamically dissipated energy per beat cycle. The energy that is dissipated inside flagella during a beat is $E^{(i)} = \oint \mathcal{R}^{(i)}$. We assume that the chemical energy rate $\mathcal{R} = \mathbf{Q} \cdot \dot{\mathbf{q}}$ that is provided by ATP is dissipated either hydrodynamically, $\mathcal{R}^{(h)} = \dot{\mathbf{q}}^T \cdot \mathbf{\Gamma}^{(h)} \cdot \dot{\mathbf{q}}$, or internally, $\mathcal{R}^{(i)} = \dot{\mathbf{q}}^T \cdot \mathbf{\Gamma}^{(i)} \cdot \dot{\mathbf{q}}$ and that energy that is stored in a reservoir such as an elastic spring is small compared to dissipation. If $\eta = 1$, no energy dissipates internally ($E^{(i)} = 0$), whereas if $\eta < 1$ the energy is dissipated internally ($E^{(i)} \neq 0$). For $\eta > 1$ the system would overreact to movements.

For simplicity, we consider intra-flagellar friction that is linear in the generalized velocities, thus adding a contribution to the generalized friction matrix.

$$\Gamma_{ij} = \Gamma_{ij}^{(h)} + \Gamma_{ij}^{(i)} \quad (3.9)$$

with $i, j \in \{\varphi, A\}$. For simplicity, we choose $\Gamma_{ij}^{(i)}$ to be proportional to the viscous friction $\Gamma_{ij}^{(h)}$.

$$\Gamma^{(i)} = \frac{1 - \eta}{\eta} \Gamma^{(h)} \quad (3.10)$$

Alternatively, a constant contribution could be assumed. This would give similar results as in section 3.3.2 (not shown).

3.2.4 Calibration of active flagellar driving forces

In our theoretical description, the flagellar beat is driven by generalized forces of the phase φ and hold on its specific shape by amplitude constraining forces, which we denote by Q_φ and Q_A , respectively. The active forces are due to the activity of molecular motors inside the flagella. For this reason we assume that these forces are a property of the cell and do not change under change of its environment such as external flow. We can calculate the active forces \mathbf{Q} with equation (3.6) and (3.7)

$$\mathbf{\Gamma} \cdot \dot{\mathbf{q}} = -\mathbf{Q} \quad (3.11)$$

imposing the dynamics of the reference cell $\dot{\mathbf{q}} = \dot{\mathbf{q}}^{\text{ref}}$, see equation (3.5), with initial state $\mathbf{q}(t=0) = (0, A_0, 0)$.

Figure 3.7 shows the phase driving force Q_φ and amplitude constraining force Q_A . The phase driving is always positive. Also, the friction component $\Gamma_{\varphi\varphi}$ is always positive, implying that the phase always propagates forward. Note, that it varies by a factor of about two. The amplitude constraining changes its sign, which relates to the fact, that hydrodynamic forces tend to bend the flagellum in opposite directions during the beat cycle. The forces \mathbf{Q} depend on the energy efficiency η . Their absolute values become larger with smaller efficiency η .

3.2.5 Stability of the limit cycle of the flagellar beat

In this section, we investigate the stability of the dynamical system (3.11) accounting for intra-flagellar friction, see equation (3.10). Active driving and constraining forces are taken by calibration, see section 3.2.4. For achieving this, we first reduce the dynamical system (3.11) to an effective oscillator, that consists only of two variables, the phase φ and the amplitude A .

We are able to add an elastic amplitude restoring force to reproduce the stability of the limit cycle of the experimental beat pattern, which crucially depends on the amplitude correlation time τ_A , which we will define.

Reference dynamics of the effective oscillator. For reproducing the experimental conditions, we have $\dot{y} = \text{const.}$, which is why we can formulate an equivalent effective system with just two degrees of freedom, a phase φ and an amplitude *amplitude*.

Explicitly writing all components of equation (3.11) then reads as

$$\begin{pmatrix} \Gamma_{\varphi\varphi} & \Gamma_{\varphi A} & \Gamma_{\varphi y} \\ \Gamma_{A\varphi} & \Gamma_{AA} & \Gamma_{Ay} \\ \Gamma_{y\varphi} & \Gamma_{yA} & \Gamma_{yy} \end{pmatrix} \begin{pmatrix} \dot{\varphi} \\ \dot{A} \\ \dot{y} = u \end{pmatrix} = - \begin{pmatrix} Q_\varphi \\ Q_A \\ F_y \end{pmatrix} \quad (3.12)$$

This way, the effective two component oscillator reads as

$$\begin{pmatrix} \Gamma_{\varphi\varphi} & \Gamma_{\varphi A} \\ \Gamma_{A\varphi} & \Gamma_{AA} \end{pmatrix} \begin{pmatrix} \dot{\varphi} \\ \dot{A} \end{pmatrix} = - \begin{pmatrix} Q'_\varphi \\ Q'_A \end{pmatrix} \quad (3.13)$$

$$\begin{aligned} Q'_\varphi &= Q_\varphi - \Gamma_{y\varphi}u \\ Q'_A &= Q_A - \Gamma_{yA}u \end{aligned}$$

Stability analysis without amplitude spring. For the reference case, equation (3.5), we have from equation (3.13)

$$\mathbf{\Gamma}(A = A_0, \varphi) \begin{pmatrix} \omega \\ 0 \end{pmatrix} = - \begin{pmatrix} Q_\varphi \\ Q_A \end{pmatrix} \quad (3.14)$$

There is a periodic orbit, when $\dot{\varphi} = \omega$ and $A = A_0$. In the following, the stability of that orbit under perturbation of the amplitude A and the phase speed $\dot{\varphi}$ is investigated.

The perturbation has the following form.

$$\begin{aligned}\dot{\varphi} &= \omega + \delta\omega \\ A &= A_0 + \delta A \\ \dot{A} &= \delta\dot{A}\end{aligned}\tag{3.15}$$

We insert the Taylor expansion around $A = A_0$ of the friction matrix, up to linear order $\Gamma(\varphi, A) \approx \Gamma(\varphi, A = A_0) + (\partial_A \Gamma)(\varphi, A = A_0)\delta A$, and the perturbation (3.15) into the reference system (3.14).

$$\begin{aligned}\partial_A \Gamma_{\varphi\varphi} \omega \delta A + \Gamma_{\varphi\varphi} \delta\omega + \Gamma_{\varphi A} \delta\dot{A} &= 0 \\ \partial_A \Gamma_{A\varphi} \omega \delta A + \Gamma_{A\varphi} \delta\omega + \Gamma_{AA} \delta\dot{A} &= 0\end{aligned}\tag{3.16}$$

Eliminating $\delta\omega$ then leads to the decay length or amplitude correlation time τ_A , by

$$\delta\dot{A} = -\omega \frac{\partial_A \Gamma_{A\varphi} - \Gamma_{A\varphi} \Gamma_{\varphi\varphi}^{-1} \partial_A \Gamma_{\varphi\varphi}}{\Gamma_{AA} - \Gamma_{A\varphi} \Gamma_{\varphi\varphi}^{-1} \Gamma_{\varphi A}} \delta A = -\tau_A \delta A.\tag{3.17}$$

For $\tau_A < 0$ the periodic is stable with respect to perturbations δA around the equilibrium amplitude. Note that, τ_A generally depends on the phase of the oscillator and, in our case, can even be positive, resulting in an unstable limit cycle dynamics. Since this is not observed experimentally, we are going to impose the amplitude relaxation time τ_A by introducing an additional force term for the amplitude.

Imposing stability by an amplitude spring. From experimental datasets, we can estimate a value for τ_A . For simplicity and because of the lack of sufficiently fine-grained measurements, we assume τ_A to be constant. In section 5.2.2, a method for determining τ_A from experimental shape data is presented. By introducing a generic elastic coupling term, that is phase dependent, we are able to impose the stability of the dynamical system (3.13).

We apply the analogous procedure as in the previous stability analysis, but add a spring force for the amplitude around A_0 , thus changing the second equation of (3.16) to

$$\partial_A \Gamma_{A\varphi} \omega \delta A + \Gamma_{A\varphi} \delta\omega + \Gamma_{AA} \delta\dot{A} = -k_A \delta A\tag{3.18}$$

again eliminating $\delta\omega$ leads to an alternative expression of τ_A , with which we define the phase dependent amplitude stiffness $k_A(\varphi)$.

$$\begin{aligned}\delta\dot{A} &= \frac{k_A + \omega [\partial_A \Gamma_{A\varphi} - \Gamma_{A\varphi} \Gamma_{\varphi\varphi}^{-1} \partial_A \Gamma_{\varphi\varphi}]}{-[\Gamma_{AA} - \Gamma_{A\varphi} \Gamma_{\varphi\varphi}^{-1} \Gamma_{\varphi A}]} \delta A = -\tau_A^{-1} \delta A \\ k_A &= \tau_A^{-1} [\Gamma_{AA} - \Gamma_{A\varphi} \Gamma_{\varphi\varphi}^{-1} \Gamma_{\varphi A}] + \omega [\partial_A \Gamma_{A\varphi} - \Gamma_{A\varphi} \Gamma_{\varphi\varphi}^{-1} \partial_A \Gamma_{\varphi\varphi}]\end{aligned}\tag{3.19}$$

Figure 3.8 (a) shows the amplitude speed \dot{A} in the (φ, A) -domain for the case of missing amplitude spring as well as with a spring for $\tau_A = 1$ ms and the experimentally determined value $\tau_A = 5.9$ ms, see section 5.2.2. In panel 3.8 (b) τ_A is shown for $k_A = 0$,

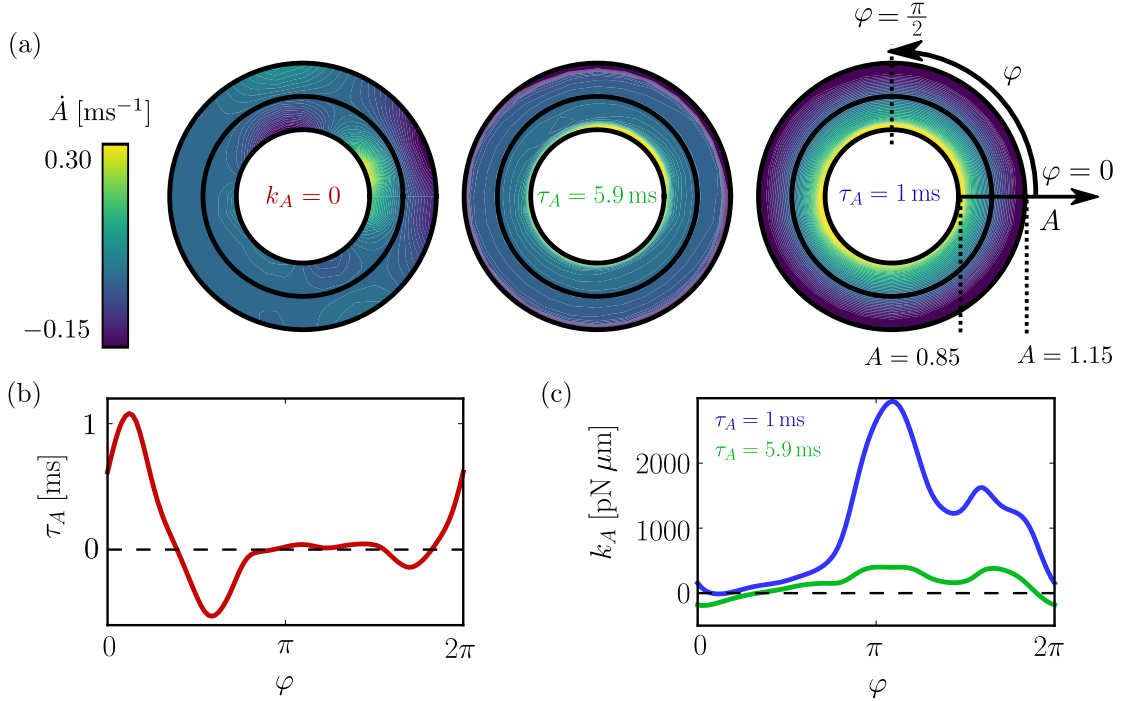


Figure 3.8: *Amplitude stability of the flagellar oscillator.* (a) The rate of change of amplitude \dot{A} as function of instantaneous phase φ and amplitude A is shown for the case without spring and for two springs with different values of the amplitude correlation time. Simulations were performed in the following way. For each position in the diagram the corresponding phase φ and amplitude A was chosen as initial condition. The friction matrix and active forces are determined, and the translational speed \dot{y} is set to zero. With this, $\dot{\varphi}$, \dot{A} and F_y can be obtained. The plot shows the respective values of \dot{A} . (b) τ_A is shown for the case without amplitude spring, see equation (3.17). In this case, τ_A is phase dependent. (c) For two different values of the correlation time τ_A , the phase dependent stiffness is shown, see equation (3.19).

which exposes different stability regimes during a period. Panel (c) shows the phase dependent stiffness $k_A(\varphi)$ for the two values of the correlation time $\tau_A = 1$ ms and $\tau_A = 5.9$ ms.

Here, we restrict ourselves to the case of phase-independent τ_A . Choosing τ_A to be a function of the phase turns out to not having a large effect on the qualitative properties of the dynamical system, see also appendix F.3.

3.2.6 Equations of motion

The full set of equations, including hydrodynamic friction $\mathbf{\Gamma}^{(h)}$ (3.7) and intra-flagellar friction $\mathbf{\Gamma}^{(i)}$ (3.10), effective amplitude spring k_A (3.19) and driving forces Q_φ and Q_A ,

(3.11) are shown for completeness.

$$\begin{pmatrix} \frac{1}{\eta}\Gamma_{\varphi\varphi} & \frac{1}{\eta}\Gamma_{\varphi A} & \Gamma_{\varphi y} \\ \frac{1}{\eta}\Gamma_{A\varphi} & \frac{1}{\eta}\Gamma_{AA} & \Gamma_{Ay} \\ \Gamma_{y\varphi} & \Gamma_{yA} & \Gamma_{yy} \end{pmatrix} \begin{pmatrix} \dot{\varphi} \\ \dot{A} \\ \dot{y}(t) \end{pmatrix} = \begin{pmatrix} Q_{\varphi}(\varphi) \\ Q_A(\varphi) - k_A(\varphi)(A - A_0) \\ Q_y \end{pmatrix} \quad (3.20)$$

We know $k_A(\varphi)$, $Q_{\varphi}(\varphi)$ and $Q_A(\varphi)$ from the calibration process and $\dot{y}(t)$ is set as boundary condition for reproducing the experiment. For each time step t' the system of equation is solved in a least square root manner, obtaining the phase speed $\dot{\varphi}(t')$ and amplitude speed $\dot{A}(t')$, which can be used to integrate the system. We did not use a simple Euler scheme, because the introduction of a second timescale by having the amplitude spring, very small time steps would be necessary to solve the system faithfully. Therefore a `python` package was used that performs a backward differentiation formula [57], which is useful for handling stiff problems with separate timescales.

With this approach, we describe the dynamics of the flagellar beat by a system of three equations, whose quantities are coupled by non-linear friction coefficients and elastic coupling terms. For solving the equations, three conditions are to be set, which can be any combination of generalized speeds and conjugate forces. For example, for a freely swimming cell, we have $Q_y = 0$ besides flagellar driving forces Q_{φ} and Q_A , whereas a clamped cell fulfills $\dot{y} = 0$. We are able to allow the flagella to deform elastically and can tune the deformability in terms of the amplitude correlation time τ_A , which sets the amplitude stiffness k_A and can study its effects on swimming. The correlation time is known from experiments, but the energy efficiency η is a single free parameter in this system. We can study its effect in different situations and determine a value from the measurements, as shown in the next section.

3.3 Comparison of theory and experiment

We consider the situation of a clamped *Chlamydomonas* cell that is exposed to external flows with flow speed u . In this chapter, we compare the analysis of the experimental datasets for different flow speeds u with the dynamics obtained by the theoretical description of the respective setting. First, we highlight the importance of the investigation of the sub-cycle dynamics, clarifying the role of phase and amplitude for the mean curvature of the beat. Then the susceptibilities of the phase speed and the amplitude to external load is investigated, and theoretical predictions are fitted to it, thus determining the single fit-parameter energy efficiency η . Third, the external flow rate is increased up to values, where the flagellar beat stops, because driving forces are not large enough for overcoming the load. Then non-isochrony is discussed, which is believed to play a major role in the synchronization properties of coupled oscillators [95].

3.3.1 Flagellar mean curvature

We define the flagellar mean bending as a arc length s dependent quantity by averaging in two ways.

$$\begin{aligned}\bar{\psi}_t(s) &= \langle \psi(s, t) \rangle_t \\ \bar{\psi}_\varphi(s) &= \langle \psi(s, \varphi) \rangle_\varphi\end{aligned}\quad (3.21)$$

$\bar{\psi}_t(s)$ is the time average and $\bar{\psi}_\varphi(s)$ is the phase average, which, in the case of zero-external flow, coincide, because then, the instantaneous phase φ is equal to ωt . When perturbing the flagellar beat by external flow, we generally have $\varphi \neq \omega t$, thus $\bar{\psi}_t(s) \neq \bar{\psi}_\varphi(s)$. Since the mean bending typically represents a shape that is similar to a circular arc, see also figure 3.9 (a), we restrict our analysis to average curvatures along the circular arc.

$$\begin{aligned}\bar{\psi}_t(s) &\approx K_t \cdot s + \bar{\psi}_{t,0} \\ \bar{\psi}_\varphi(s) &\approx K_\varphi \cdot s + \bar{\psi}_{\varphi,0}\end{aligned}\quad (3.22)$$

The curvatures K_i and the offsets $\bar{\psi}_{i,0}$ for $i \in \{t, \varphi\}$ are determined by linear regression.

The load-dependence of the time averaged curvature $K_t(u)$ is shown in figure 3.9 (b) and the phase averaged curvature's load-dependence $K_\varphi(u)$ is shown in 3.9 (c).

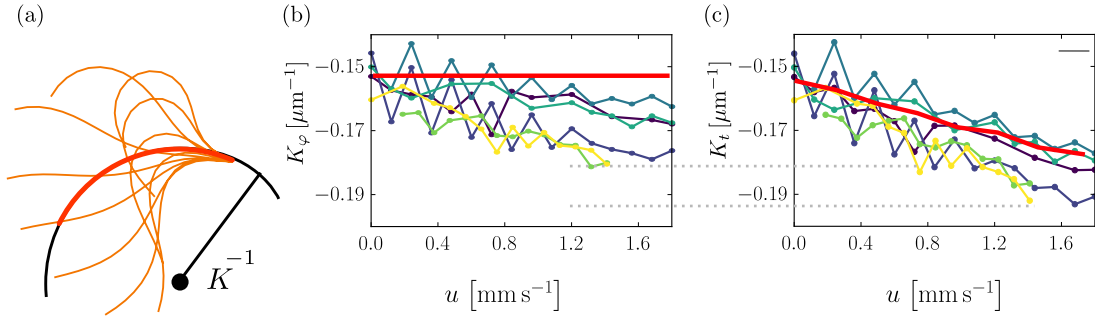


Figure 3.9: Mean flagellar curvature as a function of flow rate. (a) Different flagellar shapes are shown in orange. The mean flagellar shape can be approximated by a circular arc with radius $r = K^{-1}$, shown in red. (b) Mean time averaged curvature K_t is shown for numerical simulation (red) and all flagellar data sets. (c) Same as (b) but for mean phase averaged curvature K_φ . Video-microscopy data resulting in (b) and (c) was provided by Christian Ruloff.

K_t captures the effect, that the time that the limit cycle remains at certain scopes of the beat changes, which is due to phase changes and agrees with the theoretical prediction. Load dependent phase averaged flagellar bending K_φ cannot be reproduced by the theory.

3.3.2 Susceptibilities of phase speed and amplitude

Here, we use measurements, in which the external loads that were applied are small enough for being able to describe the effect on the instantaneous frequency and the

amplitude linearly. We define the linear susceptibilities for the phase speed $\dot{\varphi}$ and the amplitude A to the flow speed u as

$$\begin{aligned}\dot{\varphi}(\varphi; u) &= (\chi_{\varphi}(\varphi) \cdot u + 1) \omega(\varphi), \\ A(\varphi; u) &= (\chi_A(\varphi) \cdot u + 1) A_0(\varphi).\end{aligned}\tag{3.23}$$

Although, by definition, the frequency ω of the flagellar beat and the equilibrium amplitude A_0 are independent of the phase, for the determination of the phase speed susceptibility χ_{φ} we recalculate it for every phase. We do this, because the frequency has a large error due to the small number of cells and because cells may be intrinsically different from each other. By recalculating those quantities, we obtain a more robust result for χ_{φ} and χ_A .

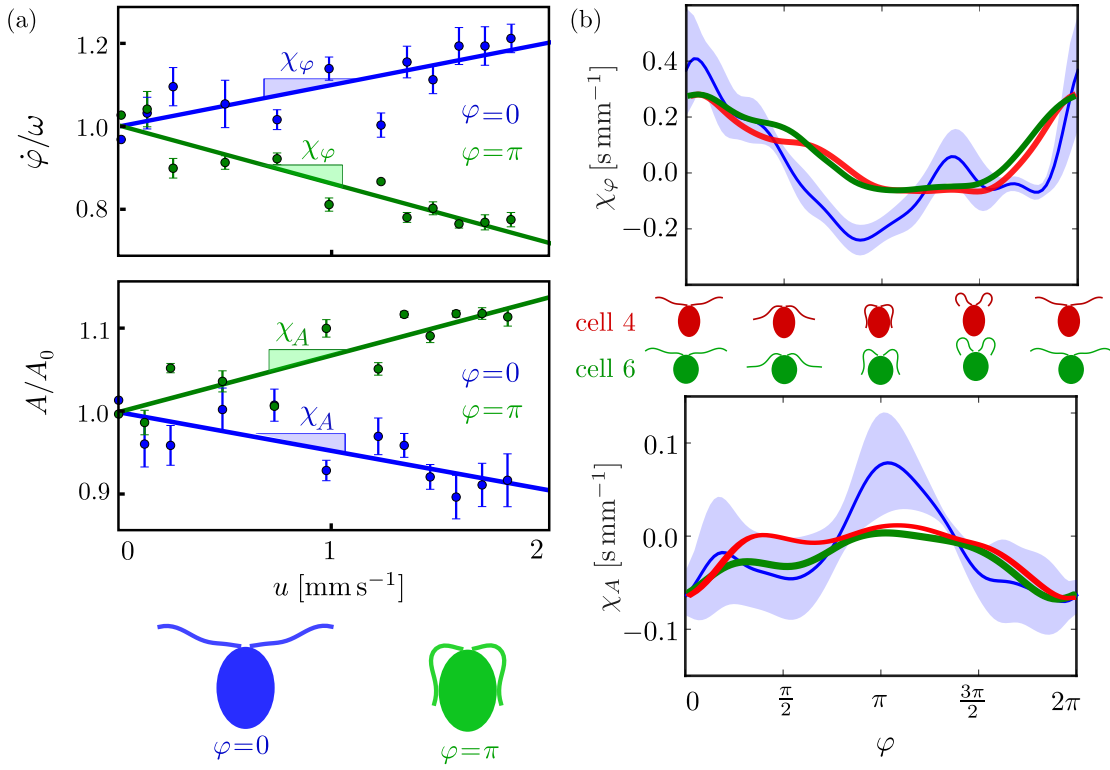


Figure 3.10: *Phase dependent phase speed and amplitude susceptibility.* (a) Susceptibilities are determined by linear regression of the respective quantity against the external flow speed. Examples are shown for a typical cell during power stroke ($\varphi = 0$) and recovery stroke ($\varphi = \pi$). The estimated error is the standard error of the mean extracted from 5 sub-datasets. (b) The red curve, obtained from simulations with shapes from cell 4, has one free parameter, the energy efficiency η and was fitted onto the experimental values (blue curve) leading to $\eta = 0.21 \pm 0.06$. The light blue error region is the standard error from the six different cells. General features of the phase speed and amplitude susceptibilities are reproduced by the model, which is an increase of the instantaneous phase speed during the power stroke and a slow down during the recovery stroke. The underlying experimental data was measured by Christian Ruloff.

The susceptibilities are the slopes of the lines defined in equation (3.23) which is why

we obtain them via linear regression of measurement points $(J(\varphi), u)$ for $J \in \{\dot{\varphi}, A\}$. In figure 3.10 (a) examples for the linear regression are shown for two representative phases, one for the power stroke $\varphi = 0$ and one for the recovery stroke $\varphi = \pi$ for a specific cell. The susceptibilities $\chi_\varphi(\varphi)$ and $\chi_A(\varphi)$ are computed for six cells and their mean and standard error are shown in figure 3.10 (b). We conclude from observing the experimental and theoretical results, that the phase speed $\dot{\varphi}$ during the power stroke increases for increasing values of the flow rate u . This is reasonable, since the direction of flow and flagellum are the same. During the recovery stroke, the flagellum is slowed down.

The amplitude susceptibility of the theoretical prediction matches well to the experimental data, except for $\varphi \approx \pi$ (recovery stroke), where the flagellum is very near to the cell body. The disagreement might be due to the fact, that in measurements, a halo around the cell body is observed, such that we might have overestimated the size of the cell body, and hence steric interactions prevent the theoretical value for the amplitude to be increased considerably.

Energy expenditure of the flagellar beat. The theoretic curves scale linearly with the energy efficiency η , defined in section 3.2.3. Thus, we can fit the theoretical predictions of χ_φ curve onto the experimental data. We repeated the fitting procedure for all successfully tracked cells and obtained $\eta = 0.21 \pm 0.06$, where the error is the standard error. This is in good agreement with previously reported values η in the range 10% to 40% [13, 28, 25, 68]. Knowing the energy efficiency and the hydrodynamic friction forces, it is possible to calculate the chemical energy that is provided by ATP hydrolysis as $\mathcal{R} = \Gamma \cdot \dot{\mathbf{q}} \approx 160 \text{ fW}$. That means, that when considering that *Chlamydomonas* has two flagella with a frequency $f_0 \approx 50 \text{ Hz}$, approximately 60,000 ATP molecules are transformed and only 12,000 of which are converted into mechanical work, which is finally dissipated into heat.

3.3.3 Higher modes and stalling of the flagellar beat at high external load

The experimental data was obtained by performing experiments with the protocol to the one described in section 3.1.1. For each flow speed u , the frequency of the flagellar beat was obtained from the Fourier spectrum of a prophase of the flagellum. The frequency peak with the maximum area below a Gaussian fit counts. The execution of the experiment as well as the analysis of the experimental data was performed by Christian Ruloff. The frequency dependency has a rich structure, examples of which are shown in figure 3.11 for four flagella, which are chosen for clarity. By manual inspection, different beating modes are related to different regions, also shown in figure 3.11.

Experimental observation of excited modes

In the experimental data we find four distinct beating modes. Compare figure 3.11 for the following descriptions of excited beating modes.

Normal beating occurs at low external flow speeds $u \lesssim 5 \text{ mm s}^{-1}$. Its frequency f increases linearly around $u = 0$ and seems to flatten towards higher values.

Tremor-like beating has a similar shape to normal beating for phase $\varphi \approx \pi$. It is still beating in an oscillatory fashion, but it seems to stop the beat at a phase slightly larger $\varphi \gtrsim \pi$, relaxing back to a phase slightly lower than that value $\varphi \lesssim \pi$, then again increasing the phase. The frequency of that pattern is similar to the frequency of the unperturbed beat at $u = 0$ and does not change much when the flow speed is changed.

Chiral beating has a significant binormal or out-of-plane contribution. It is similar to tremor like beating, but the flagellum leaves the beating plane of the normal or tremor-like beat pattern in a regular manner. Its frequency usually is lower than that of the unperturbed beat at $u = 0$ and is unaffected by the flow speed.

Stalling means, that the beat stops. Thus, its frequency drops to zero. We observe a transition state, in which the flagellar shape looks like the maximum phase of the tremor-like pattern, which does not relax back. For very high flow speeds, the flagellum folds back and aligns with the cell body. The critical flow-speed at which stalling occurs is $u_c \approx 8 \text{ mm s}^{-1}$, see also the blue inset in figure 3.12 (b) shows a histogram of stalling events. It also happens that the beat stops, but with negative external flow. Stalling of this kind happens at surprisingly low values of the absolute value of the external flow-speed $u_c \approx 0.5 \text{ mm s}^{-1}$.

Multistable beating is a beat pattern that switches back and forth between tremor-like and binormal beating, without varying the external load. Mode transitions between normal beating and stalling is usually not observed when varying the hydrodynamic load. The most frequent continuous transitions are from normal mode to the multistable mode and from the multi-stable mode to the chiral mode. The most frequent discrete mode transition goes from chiral mode to stalling. The transitions occur for increasing as well as for decreasing flow speeds and usually show hysteresis.

The theoretical description predicts stalling

The normal mode beat pattern is the one we can reproduce with our theoretical description of the last section 3.2, using phase φ and amplitude A for parameterizing the beat, which we also used for comparing the susceptibilities χ_φ and χ_A , see section 3.3.2. The theoretical description does not show tremor-like beating, and binormal beating is impossible, because only planar beat patterns can be reproduced.

The mean frequency. is obtained by running simulations for a time interval $\Delta t = 30T_{u=0}$ of 30 periods of the unperturbed flagellar beat. The last reciprocal period gives the frequency $f = T^{-1}$. Note, that for high flow rates $u \lesssim u_c$ near the stalling point, the frequency obtained by this procedure may be $f = 0$ although the phase dynamics did not stop, but is just very slow. The theoretical stalling point is at $u_c \approx 12 \text{ mm s}^{-1}$. The red curve in figure 3.12 (b) shows the frequency dependency on external load.

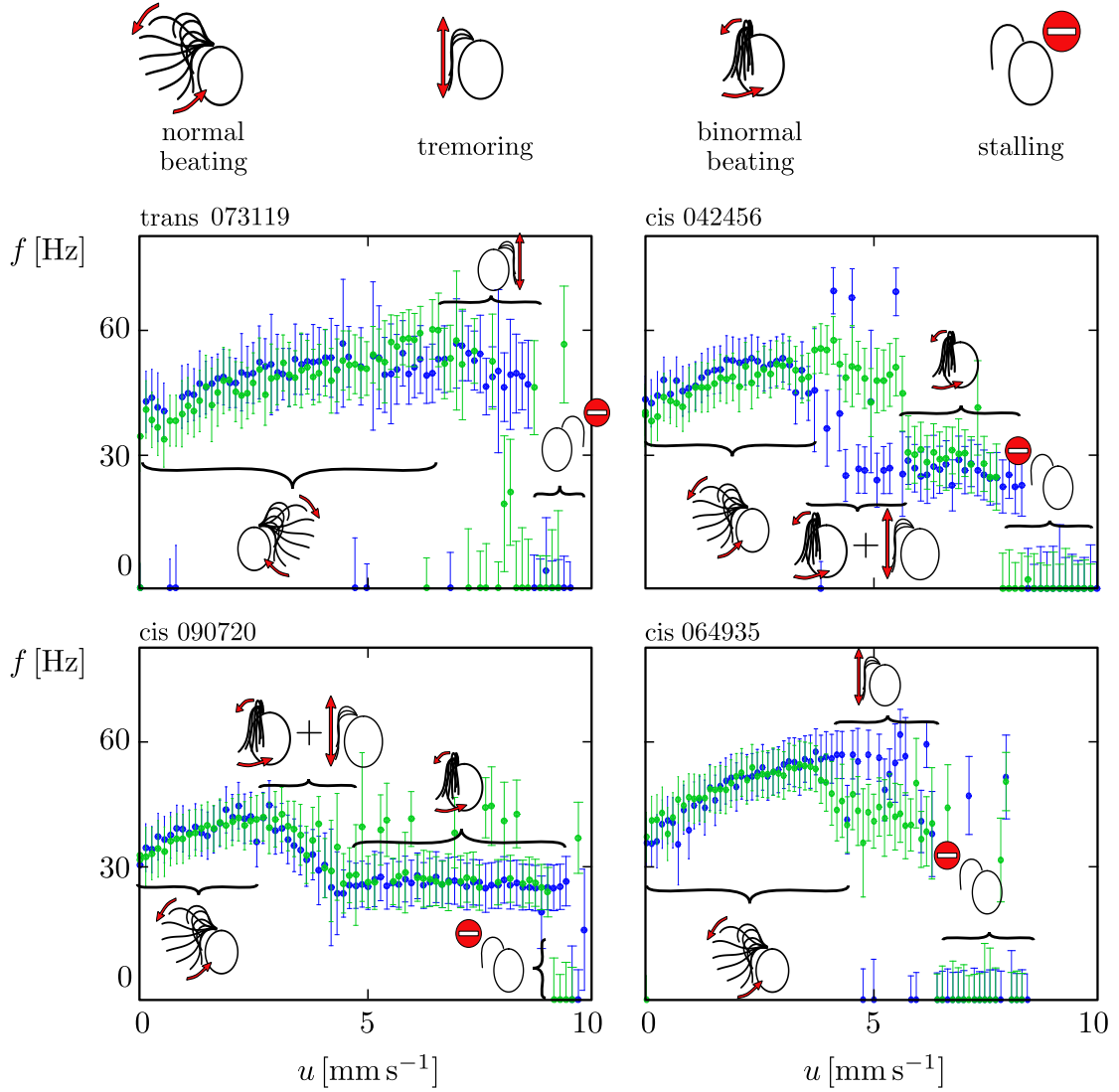


Figure 3.11: *Flagellar stalling at high load and higher modes.* The frequency of four different flagella of different cells are shown for presenting typical effects that occur when the external flow is increased up to a value when stalling occurs. At the top left corner of each graph is a cell identifier which contains information of whether the flagellum is a cis or trans flagellum. If no external flow is imposed, the flagellum beats normally (🌀). It is always possible to stall the flagellar beat (🛑) by imposing high load. For moderate flows, regions exist, in which higher modes arise, like tremoring (🌀) and binormal beating (🌀), see main text for more thorough descriptions. The underlying experimental data was measured and analyzed by Christian Ruloff.

A saddle node bifurcation. occurs at $u = u_c^+$. To see this, we performed simulations, generating the load dependent phase speed field on the state space of the flagellum. For a certain amplitude $A = 0.9$. For zero load $u = 0$, the phase speed $\dot{\varphi}(\varphi)$ is positive for all phases φ . When increasing u , the phase speed during the recovery stroke at $\varphi = \varphi_c^+ \approx \frac{3\pi}{2}$ decreases, until it reaches zero for $u = u_c^+ \approx 12 \text{ mm s}^{-1}$. This is

a fixed point for the phase speed dynamics, which is a saddle node. Further increasing u leads to a splitting into a stable fixed point at a slightly lower phase $\varphi \lesssim \varphi_c^+$ and an unstable fixed point at a slightly larger phase $\varphi \gtrsim \varphi_c^+$. Stalling for negative flow rates occurs analogously as saddle node bifurcation, but for a lower value $u_c^- \approx -7 \text{ mm s}^{-1}$ at a different phase $\varphi = \varphi_c^- \approx \frac{\pi}{5}$. Figure 3.12 shows the phase speed field and a schematic of the corresponding bifurcation diagram.

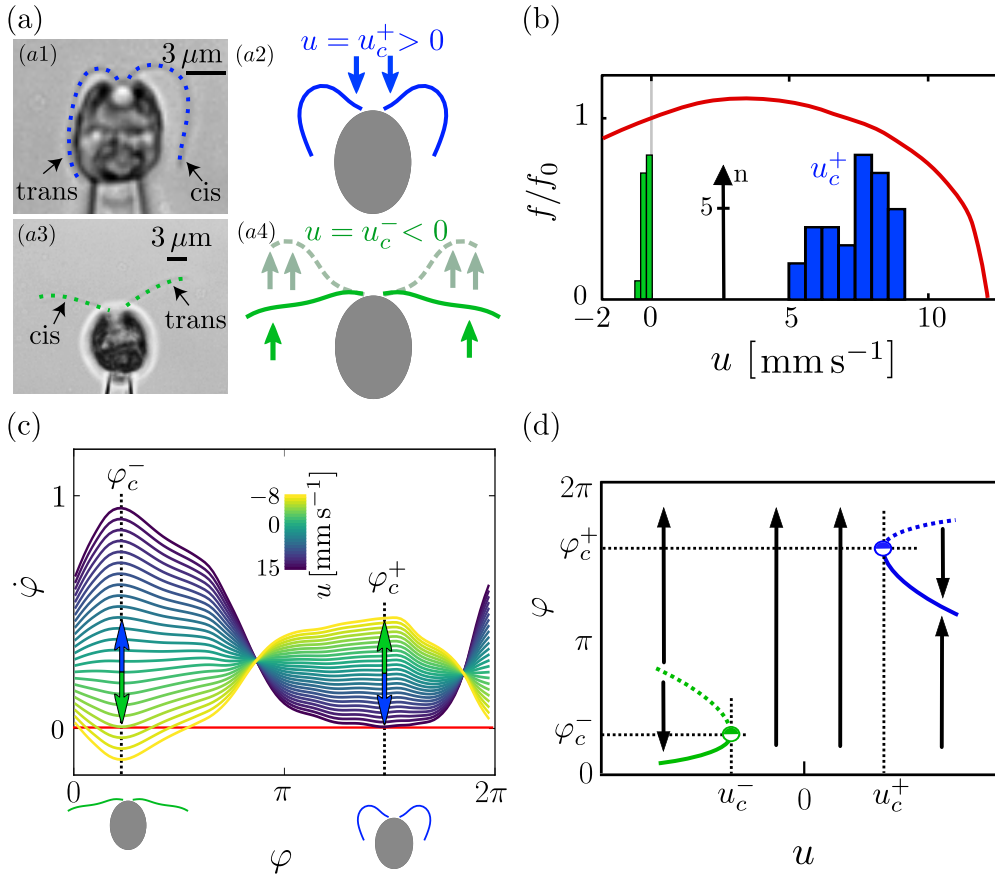


Figure 3.12: *Flagellar stalling in experiment and theory.* (a) Flagellar stalling for a typical cell (a1) when flow comes from the front is similar to the simulated version (a2). The same is true for external load from the back (a3). The theoretical result is shown in (a4). The solid flagellar shape forms at $u = u_c^-$, the dashed shape forms at external flows below the bifurcation point. Movie stills are from Christian Ruloff. (b) The red curve is the frequency of the computed flagellar beat of a clamped cell with different external flow speeds u . The blue histogram shows the flow speed of measured stalling events (provided by Christian Ruloff). Its mean value is approximately 8 mm s^{-1} and is comparable to the theoretical value $\approx 12 \text{ mm s}^{-1}$. For negative flow speeds, the experimental stalling speed (see green histogram, provided by Christian Ruloff), reveals a surprisingly low stall speed. (c) Stalling occurs through a saddle node bifurcation of the phase dynamics, in which a stable and an unstable fixed point is created from a saddle node, when increasing the external flow speed.

Up to flow speeds at which the frequency of the theoretical description reaches its maximum, the monotonic increase of the experimental frequency values is well predicted.

This is in good agreement with the comparison of the phase speed susceptibility χ_φ in section 3.3.2. From figure 3.10 we conclude that $\int_0^{2\pi} d\varphi \chi_\varphi(\varphi) > 0$ for the experimental cell as well as the theoretical model, which is equivalent to having an increased frequency for higher loads u . For higher external loads we cannot assume linear response of the phase speed any more, see equation (3.23). Stalling occurs in the theoretical model as well as in the experiment, with critical values in the same order of magnitude for forward stalling. The experimental value for the critical flow-speed at which backward stalling occurs is much smaller than the predicted value of the theoretical description.

3.3.4 Non-isochrony of flagellar oscillations

The non-isochrony $-\omega_1/\omega$ is a property that was suggested as a synchronization mechanism by [95, 78]. It describes the dependency of the phase speed on the amplitude. A positive value means, that when the amplitude is larger than the equilibrium value, the phase is slowed down and it speeds up for positive values. The friction matrix, shown in figure 3.7, already gives a hint for non-isochrony, since the phase friction component depends monotonically on the amplitude, $\partial_A \Gamma_{\varphi\varphi} > 0$. We write

$$\dot{\varphi} = \omega - \omega_1 A^2 \quad (3.24)$$

which is motivated by the fact that the flagellar beat can be described as a Hopf

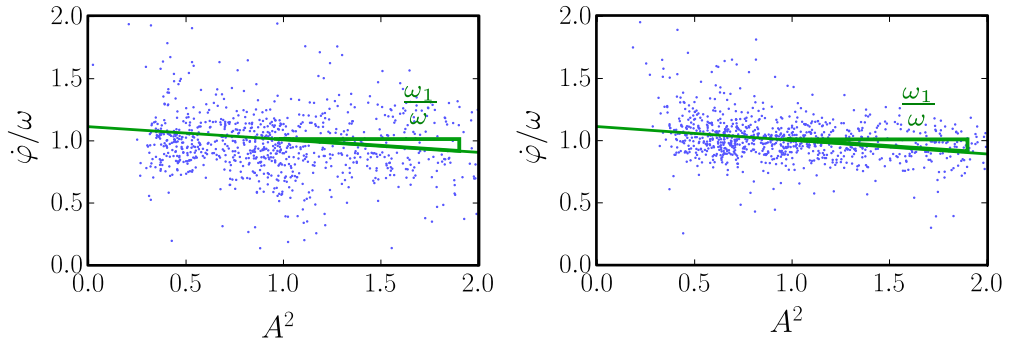


Figure 3.13: *Non-isochrony*. The frequency dependence on the squared amplitude is shown for the two flagellar datasets that were used for the theoretical description in this section. The slope of the linear regression is a measure for the non-isochrony. Video-microscopy data was provided by Christian Ruloff.

oscillator, see section 5.1 for details.

Experimental results are shown in figure 3.13. We find $\omega_1/\omega = 0.077 \pm 0.027$. The theoretical prediction is $\omega_1/\omega \approx 0.78$. While the sign of the non-isochrony matches, the theoretical description predicts a ten-fold higher value.

3.4 Summary

An experimental setup was described, with which it has been possible to clamp a beating *Chlamydomonas* cell while imposing a controlled external flow. The experiments were

performed by Christian Ruloff. With this, we were able to determine, how speed and shape of the flagellar beat changes in response to hydrodynamic forces. For this aim, we developed an effective theory of the flagellar beat, that is calibrated by experimental data.

The crucial theoretical parameter that sets the sensitivity of the flagellar beat to external load is the energy efficiency η , that sets the ratio of energy that is provided by chemical processes and the energy that is dissipated into the fluid. The determined value $\eta \approx 0.2$ agrees with previous estimates.

The developed theory includes a degree of freedom, called flagellar amplitude, that allows a flagellum to deform additionally to the common phase dependent shape. We determined the flagellar amplitude stiffness, which was proposed to have significant impact on the synchronization behavior of the flagellar beat, which is investigated in the next chapter.

For high external load the flagellar beat stalls in a saddle-node bifurcation. Surprisingly, we found higher modes of the flagellar beat in the experimental data that were not reported previously in the literature.

Flagellar load-response facilitates synchronization

The last chapter addressed the question of how sensitive the flagellar beat is with respect to external, mechanical forces, induced e.g. by hydrodynamic flows. This sensitivity is a necessary property for flagellar synchronization, either within collections of flagella or for synchronization to external oscillatory flow.

Chapter overview. In this chapter, two synchronization phenomena are studied through numerical simulations. First, external driving is applied by an oscillating fluid flow $u(t)$ with a frequency close to the beat frequency of *Chlamydomonas*. This numeric experiment is motivated by an experiment of Quaranta et al. [104]. For this, the theoretical framework that was presented in chapter 3 is used. Second, the synchronization of the two flagella of *Chlamydomonas* with each other is investigated. For this, the previously used framework is extended to allow for non-synchronized beating. Further, an additional elastic coupling between the flagella is introduced, which is biologically motivated by the so called distal striation fibers in *Chlamydomonas* [109].

4.1 Synchronization to external driving

We consider the situation of a *Chlamydomonas* cell that is held by a micro-pipette and a periodic external flow is imposed with a frequency f_u that is close to the frequency f of the flagellar beat.

In the experiments reported in [132], a time dependent external flow of square form $u(t) = 2U_F(\Theta(\sin(2\pi f_u t)) - \frac{1}{2})$ is applied, as depicted in figure 4.1 (a). Θ is the Heaviside function. The phase difference $\delta = \varphi - 2\pi f_u t$ of the flagellar phase φ and the external

flow phase $2\pi f_u t$ is analyzed. In the experimental system with thermal and active flagellar noise the fraction of time at which phase locking occurs is a measure for the synchronization strength.

In the theoretical model system without noise, that fraction can be either zero or one, after a certain transient. We expect that transient to be relaxed after 50 beat cycles and determined if phase locking occurs by comparing the total phase lag after that time. If it is smaller than 2π , then no phase slip happened, and the cell is synchronized with the external flow. Of course, this is only an upper bound for estimating the region of synchronization. The Arnold tongue for this system is shown in figure 4.1 (b) for different values of the energy efficiency η . The experimental finding of Quaranta et al. [104] is also included.

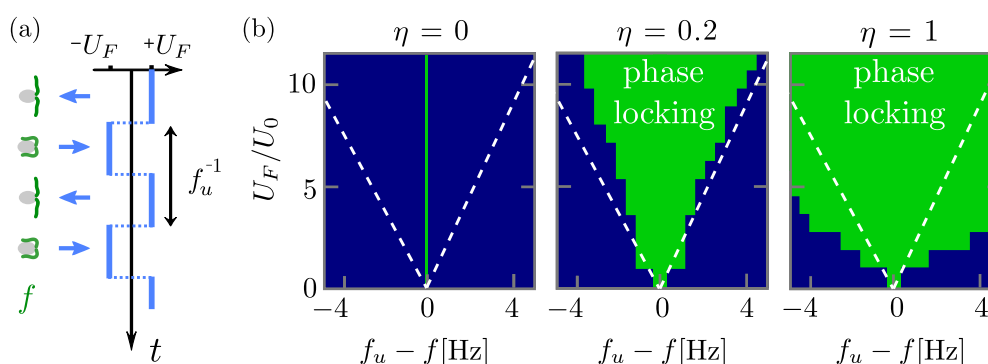


Figure 4.1: *Arnold tongue of flagellar synchronization to periodic driving for different energy efficiencies.* (a) Schematics of the external driving in the experiment of Quaranta [104] and our simulations. A *Chlamydomonas* is exposed to periodic external flow rate given by a square wave. The frequency f_u of the flow is close to the intrinsic frequency f of the flagellar beat. The amplitude of the external driving is U_F . (b) Arnold tongues from numerical simulations showing phase locking as a function of frequency mismatch $f_u - f$ and amplitude U_F for different energy efficiencies η . For $\eta = 0$, synchronization with external flow does not occur when $f_u \neq f$. When the energy efficiency is increased, the Arnold tongue becomes broader. The dashed white line represents the experimental finding, taken from [104] and fits well to the case $\eta = 0.2$.

The effect of energy efficiency on synchronization. When the energy efficiency η is zero, it means that hydrodynamic forces are negligible compared to internal friction forces. Thus, any applied external force is small and has no effect on the flagellar beat due to a vanishing susceptibility. Consequently, the Arnold tongue for such a system would be just a line at $f_u - f = 0$ as any frequency mismatch between intrinsic beating frequency and external flow would lead to the accumulation of a phase lag. For larger values of the energy efficiency, the Arnold tongue becomes broader, since susceptibilities increase and external forces have a stronger impact on the instantaneous phase speeds. In the last chapter we determined the energy efficiency $\eta \approx 0.2$ by fitting the theoretical prediction for the phase speed susceptibility on experimental results. Of course, we could as well use the Arnold tongue of figure 4.1 (b) to determine the energy efficiency. We did not do that, since this procedure is computationally very demanding and the

opening angle of the Arnold tongue of our theoretical description with $\eta = 0.2$ and the experiment result of Quaranta [104] matches quite well.

For an intuitive understanding, why synchronization with external periodic driving occurs the notion of a power and recovery stroke for the external flow helps. During the power stroke the flagella of *Chlamydomonas* move from the front to the back, and from back to front during the recovery stroke. In the same way, the periodic flow has a time span in which the direction of flow goes from the front of the cell to the back of the cell. We call this power stroke. Recovery stroke is defined analogously. If the external flow is in the power stroke and the cell is in the recovery stroke, the flagellar phase speed is reduced. The same is true if the flow is in the recovery stroke and the cell is in the power stroke. If the strokes are the same, the phase speed it increased.

In principal, it is possible to observe higher synchronization modes with $f \approx 2f_0$ that reflect in the presence of additional Arnold tongues. Considering the intuitive picture formed in the previous paragraph, we see, that no systematic phase speed change can be predicted, since during a certain stroke (*e.g.* power stroke), the external driving runs through both kinds of strokes, increasing the flagellar phase speed a certain time, then decreasing it again. In simulations we did not find more Arnold tongues at $f_u \approx 2f$ and $f_u \approx \frac{1}{2}f$.

4.2 *Inter-flagellar synchronization in the green alga Chlamydomonas*

In experiments, it is observed that the two flagella of Chlamydomonas synchronize in-phase, both for clamped cells and for free-swimming cells [133]. The physical origin of this phenomenon is still unclear, while several symmetry breaking synchronization mechanisms may play a role [40]. Some authors suggest that an additional basal coupling might be crucial to facilitate in-phase synchronization [104, 132]

In this section, an extension to the theoretical description of flagellar swimming is presented that allows the two flagella of the model system to have two different phases, which in turn describe deviations from synchronized beating. Then, the synchronization strength λ is defined. It is computed for different situations. First, the parameter controlling the internal friction of flagella, the energy efficiency η , and the parameter controlling the stiffness of flagella, the amplitude correlation time τ_A are set constant ($\eta = 0.2$, $\tau_A = 5.9$ ms) and the synchronization strength λ for the freely swimming cell and the clamped cell are calculated. Next, those same parameters are varied for testing the robustness of the system.

The physical situation, in which the cell is clamped, thus cannot translate and rotate, deserves special attention, because it has not been possible, yet, to model a system of *Chlamydomonas* with a synchronization strength that is in agreement with experimental findings. Therefore the elastically clamped cell is investigated. A very stiff orientational

spring might model the rigid cell wall within Chlamydomonas.

Interestingly, we observe anti-phase synchronization in the model, which is the opposite behavior of experimental findings [133]. Therefore the model is further extended by a basal body coupling, with is inspired by the biological model system [109]. With that, the experimentally measured synchronization strength can be reproduced. At the end of this section, three experiments are proposed for testing the hypothesis, that the combination of waveform compliance with elastic basal body coupling is the relevant synchronization mechanism in Chlamydomonas.

4.2.1 Equations of motion for inter-flagellar synchronization

Each flagellum of the Chlamydomonas cell, denoted L and R is described as phase-amplitude oscillator with respective phases φ_L and φ_R and amplitudes A_L and A_R . Since a planar beat pattern is used for both flagella, the swimming path lies in a plane and there are only two Cartesian coordinates x and y of the cell body center and one orientational degree of freedom α of the cell body to consider.

The state vector of generalized coordinates

$$\mathbf{q}(t) = (\varphi_l(t), \varphi_r(t), A_l(t), A_r(t), x(t), y(t), \alpha(t)) \quad (4.1)$$

governing seven degrees of freedom fully describes the state of the flagellum at each given time t . The generalized velocity is defined by the time derivative of the generalized coordinate $\dot{\mathbf{q}}$. \mathbf{P} is the generalized force, that is defined by considering the dissipation relation $\mathcal{R} = \mathbf{P} \cdot \dot{\mathbf{q}}$

The velocities and dissipative forces are related by the friction matrix $\mathbf{\Gamma} = \mathbf{\Gamma}^{(h)} + \mathbf{\Gamma}^{(i)}$, that depends on the current state \mathbf{q} and consists of a hydrodynamic contribution $\mathbf{\Gamma}^{(h)}$ as well as an internal contribution $\mathbf{\Gamma}^{(i)}$. The hydrodynamic part is calculated as detailed in section 3.2.2. The internal part via equation (3.9) but with $(i, j) = (i'_k, j'_k)$ for $i', j' \in \{\varphi, A\}$ and $k \in \{L, R\}$.

For a single cell, the friction is independent of its position and the orientational dependence of the components of the friction matrix is obtained by rotation $\mathfrak{R}(\alpha)$ in the xy -plane:

$$\mathbf{\Gamma}(\mathbf{q}) = \mathfrak{R}^{-1}(\alpha)\mathbf{\Gamma}(\alpha = 0, \varphi_L, \varphi_R, A_L, A_R)\mathfrak{R}(\alpha) \quad (4.2)$$

with the generalized rotation matrix

$$\begin{aligned} \mathfrak{R}(\alpha) = & \sum_{k \in \{\varphi_L, \varphi_R, A_L, A_R, \alpha\}} \mathbf{e}_k \otimes \mathbf{e}_k \\ & + \cos(\alpha) \mathbf{e}_x \otimes \mathbf{e}_x - \sin(\alpha) \mathbf{e}_x \otimes \mathbf{e}_y \\ & + \sin(\alpha) \mathbf{e}_y \otimes \mathbf{e}_x + \cos(\alpha) \mathbf{e}_y \otimes \mathbf{e}_y \end{aligned} \quad (4.3)$$

All oscillator variables φ_k and A_k for $k \in \{L, R\}$ are active and driven by half the forces obtained from the calibration process in section 3.2.4, see also figure 3.7, because the respective force drives just one flagellum instead of two as it was the case in the

descriptions in chapter 3. Also, the stiffness k_A is the same as in the previous description, see section 3.2.5.

The full dynamics can then be obtained by integrating the system, whose time dynamics is given by the following balance of generalized forces.

$$\begin{aligned}
 & \begin{pmatrix} \frac{1}{\eta}\Gamma_{\varphi_L\varphi_L} & \Gamma_{\varphi_L\varphi_R} & \frac{1}{\eta}\Gamma_{\varphi_LA_L} & \Gamma_{\varphi_LA_R} & \Gamma_{\varphi_Lx} & \Gamma_{\varphi_Ly} & \Gamma_{\varphi_L\alpha} \\ \Gamma_{\varphi_R\varphi_L} & \frac{1}{\eta}\Gamma_{\varphi_R\varphi_R} & \Gamma_{\varphi_RA_L} & \frac{1}{\eta}\Gamma_{\varphi_RA_R} & \Gamma_{\varphi_Rx} & \Gamma_{\varphi_Ry} & \Gamma_{\varphi_R\alpha} \\ \frac{1}{\eta}\Gamma_{A_L\varphi_L} & \Gamma_{A_L\varphi_R} & \frac{1}{\eta}\Gamma_{A_LA_L} & \Gamma_{A_LA_R} & \Gamma_{A_Lx} & \Gamma_{\varphi_Ly} & \Gamma_{A_L\alpha} \\ \Gamma_{A_R\varphi_L} & \frac{1}{\eta}\Gamma_{A_R\varphi_R} & \Gamma_{A_RA_L} & \frac{1}{\eta}\Gamma_{A_RA_R} & \Gamma_{A_Rx} & \Gamma_{A_Ry} & \Gamma_{A_R\alpha} \\ \Gamma_{x\varphi_L} & \Gamma_{x\varphi_R} & \Gamma_{xA_L} & \Gamma_{xA_R} & \Gamma_{xx} & \Gamma_{xy} & \Gamma_{x\alpha} \\ \Gamma_{y\varphi_L} & \Gamma_{y\varphi_R} & \Gamma_{yA_L} & \Gamma_{yA_R} & \Gamma_{yx} & \Gamma_{yy} & \Gamma_{y\alpha} \\ \Gamma_{\alpha\varphi_L} & \Gamma_{\alpha\varphi_R} & \Gamma_{\alpha A_L} & \Gamma_{\alpha A_R} & \Gamma_{\alpha x} & \Gamma_{\alpha y} & \Gamma_{\alpha\alpha} \end{pmatrix} \begin{pmatrix} \dot{\varphi}_L \\ \dot{\varphi}_R \\ \dot{A}_L \\ \dot{A}_R \\ \dot{x} \\ \dot{y} \\ \dot{\alpha} \end{pmatrix} \\
 & = \begin{pmatrix} Q_{\varphi_L}(\varphi_L) \\ Q_{\varphi_R}(\varphi_R) \\ Q_{A_L}(\varphi_L) - k_A(\varphi_L)(A_L - A_0) \\ Q_{A_R}(\varphi_R) - k_A(\varphi_R)(A_R - A_0) \\ Q_x \\ Q_y \\ Q_\alpha \end{pmatrix} \tag{4.4}
 \end{aligned}$$

We have a system of equations with seven degrees of freedom, so we need seven conditions in the form of time or phase dependent functions. Those can be either functions for conjugate forces or for the trajectory itself. Generally, if amplitude variation is allowed, the conjugate forces $Q_{\varphi_L}, Q_{\varphi_R}$ for the phases and Q_{A_L}, Q_{A_R} for the amplitudes are set and assumed to be independent from external influences. The case of a clamped cell that does not translate and does not rotate is described by $\dot{x} = 0, \dot{y} = 0, \dot{\alpha} = 0$, whereas a freely swimming cell mandates $Q_x = Q_y = 0$ and $Q_\alpha = 0$.

Interpretation of specific components of the friction matrix. The flagellar self-interaction terms Γ_{I_i, J_i} for $I, J \in \{\varphi, A\}$ and $i \in \{L, R\}$ strongly depends on the respective flagellum i . For example the dependence of $\Gamma_{\varphi_L\varphi_L}$ on φ_R and A_R is very small compared to the dependence on φ_L and A_L . The coefficients Γ_{I_L, J_R} describe direct hydrodynamic interactions between the two flagella and are dependent on all state variables, but are more than a magnitude smaller than the self-interaction terms. This is partly due the low energy efficiency $\eta = 0.2$, that effectively increases the components Γ_{I_L, J_L} and Γ_{I_R, J_R} . All diagonal elements are positive for all states. The translational friction components Γ_{xx} and Γ_{yy} are almost constant. Note that the diagonals $\varphi_L = \varphi_R$ of all components Γ_{ij} for $i, j \in \{x, y, \alpha\}$ can be similarly found in the grand friction matrix, shown in figure 2.3, with differences that are due to the usage of a different flagellar waveform.

Note that the rotational coupling fulfills the symmetry $\Gamma_{I_L, \alpha}(\varphi_L, \varphi_R) = -\Gamma_{I_R, \alpha}(\varphi_R, \varphi_L)$. That means, that there is no effect on the rotational motion if the two flagella beat in synchrony $\varphi_L = \varphi_R$. Note also that the flagellar coupling to rotation is significantly larger than the coupling to translational degrees of freedom, considering physically relevant magnitudes of the respective quantities during flagellar swimming. It follows

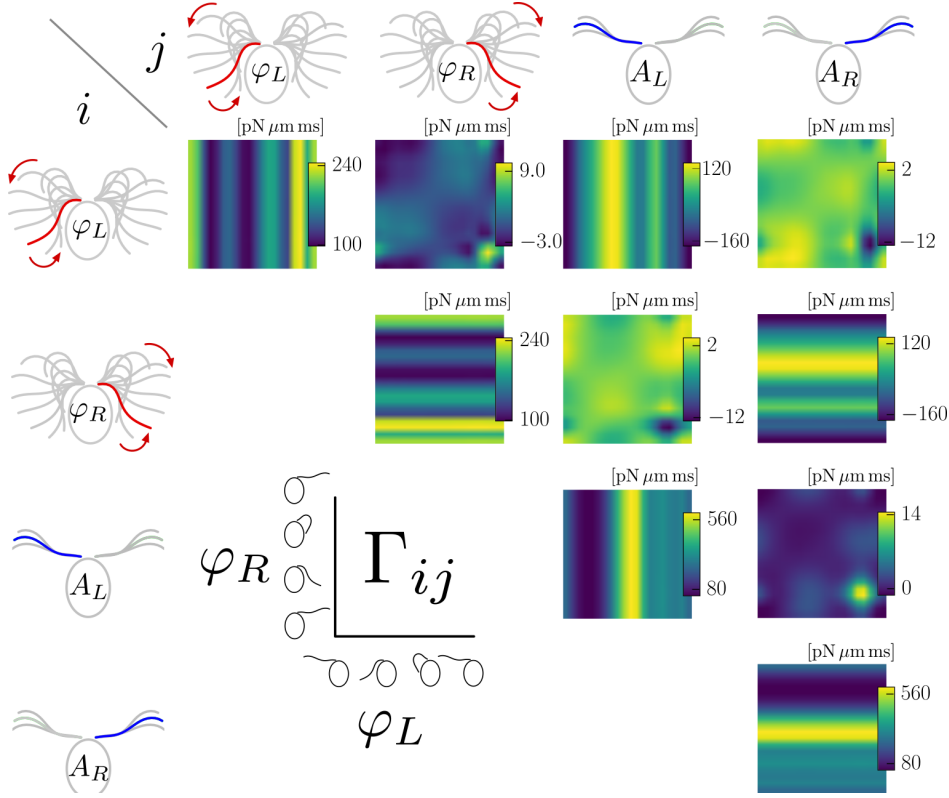


Figure 4.2: *Hydrodynamic friction matrix components in generalized coordinates, phases and amplitudes.* Since the friction matrix is symmetric, see equation (C.7), it is sufficient to show the upper triangular part. Here, the coupling terms of flagellar coordinates are shown. The remaining components of the 7×7 -matrix are shown in figure 4.3.

that flagellar swimming has a large rotational contribution if the flagellar beat is not synchronized in-phase, thus swimming is not straight.

4.2.2 Synchronization strength for free-swimming and clamped cells

We compute the dynamics of the freely swimming cell by imposing $Q_x = Q_y = 0$ and $Q_\alpha = 0$ in equation (4.4). As initial condition we choose $\mathbf{q} = (0, \delta_0, 1, 1, 0, 0, 0)$ with $\delta_0 = 0.01$.

For obtaining the synchronization strength λ we map the dynamics onto the Adler equation (1.1). For our simulations we use small perturbations in the phase difference $\delta \geq 0$ such that we can use the linearized Adler equation $\dot{\delta} = -\frac{\lambda}{T_L} \delta$ with dimensionless synchronization strength λ and period of the left flagellum T_L . Note that the dynamics that is represented by the Adler equation is purely due to the coupling of phase differences, but the coupling of flagella in *Chlamydomonas* is periodic in its phases. Therefore we use a stroboscopic projection of the dynamics on a certain phase φ_L of one flagellum and compute the synchronization strength λ in this way. We do this for a number of

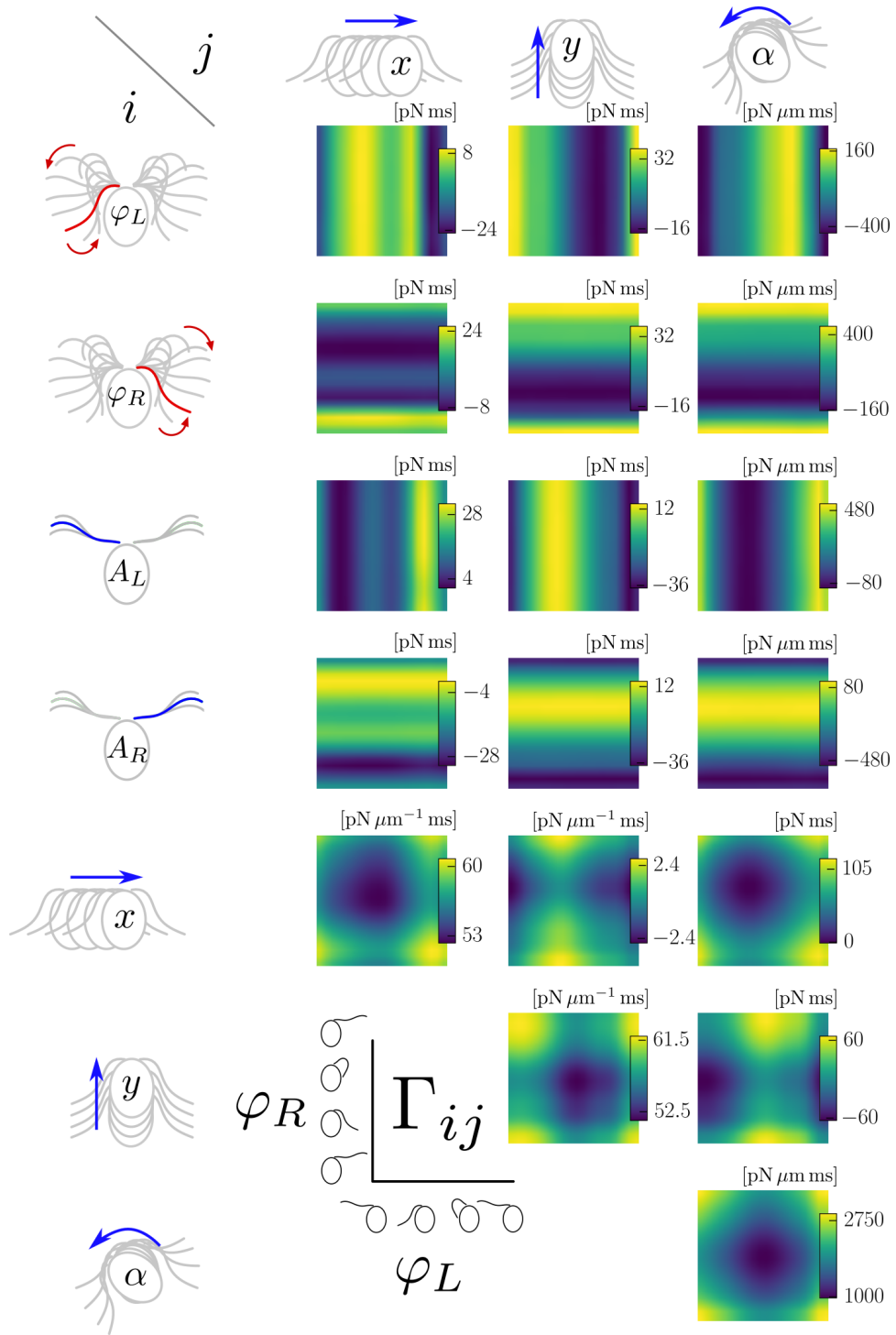


Figure 4.3: Hydrodynamic friction matrix components in generalized coordinates: remaining coordinates. The flagellar variables are coupled indirectly through the translational and orientational degrees of freedom. For direct interactions, see figure 4.2.

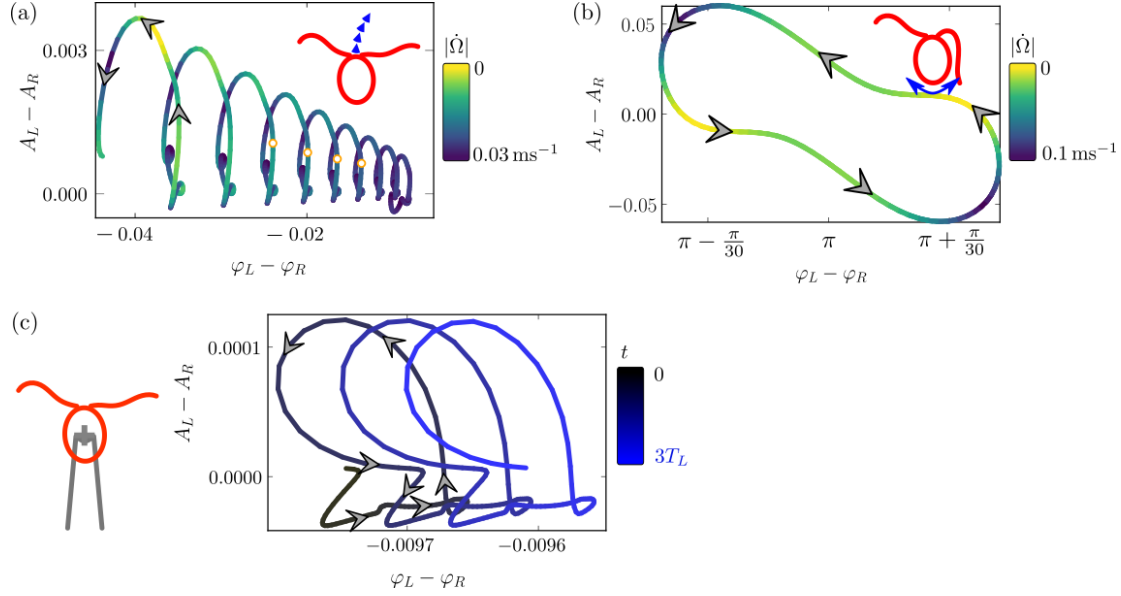


Figure 4.4: *Synchronization of clamped and freely swimming cell.* In all three plots, a projection of the dynamics of flagellar dynamics on the phase difference $\varphi_L - \varphi_R$ and amplitude difference $A_L - A_R$ is shown. (a) The color code represents the angular speed, which has a dominant effect on synchronization for the freely swimming cell. The orange points are used to calculate the synchronization strength with equation (4.5). The orange points represent the stroboscopic map that is generated at $\varphi_L = n \cdot 2\pi + \varphi_0$ for $n = 1, \dots$ and arbitrary offset φ_0 . (b) The anti-phase synchronized state of the freely swimming cell is stable. When the dynamics start with initial conditions as in (a), the limit cycle shown in (b) is reached after infinite time. (c) The dynamics of a clamped cell is shown. The line color goes from black ($t = 0$) to blue ($t = 3T$). Arrows depict the arrow of time.

different phases $\varphi_0 \in [0, 2\pi)$ and use the average value $\lambda = \langle \lambda'(\varphi_0) \rangle_{\varphi_0}$ with

$$\lambda' = -\ln \frac{\delta_{n+1}}{\delta_n} \quad (4.5)$$

with $\delta_n = \delta(t_n)$ and $\varphi_L(t_n) = 2\pi n + \varphi_0$. Figure 4.4 (a) shows orange points, pointing to states with $\varphi_L = 2\pi n + \varphi_0$ for a specific offset φ_0 .

Using equation (4.5), we find for the freely swimming cell $\lambda = -0.165$, which indicates anti-phase synchronization. This is very surprising, since experimental findings are in the range of $\lambda \approx 0.3$ [133], which could be theoretically verified by a less general theory of the flagellar beat [41] to the one that we use here. In that other theory no internal friction is considered and the amplitude degree of freedom is missing entirely, which corresponds to the case of an infinitely strong amplitude spring in our theory, see section 3.2.5. We can reproduce the results of the previous theoretical description when we turn off the mentioned mechanisms. Using that simplified theory, it was reported that cell body rocking is the dominant synchronization mechanism [41], which seems to be reversed by the inclusion of the amplitude degree of freedom. Figure 4.4 (a) shows the trajectory of the projected flagellar phase space onto the flagellar phase lag and amplitude difference. After a period, the phase lag and the amplitude difference is increased as well as the

rotational speed, which is shown in color.

Figure 4.4 (a) shows the projection of the trajectory of the freely swimming cell onto the two-dimensional flagellar phase space consisting of phase lag and amplitude difference. After one period, the phase lag is slightly increased. A system of two coupled oscillators with just one degree of freedom each has exactly two fixed points, one of which is stable, the other one is unstable. If $\lambda < 0$ there is an unstable fixed point at $\delta = 0$ and a stable fixed point at $\delta = \pi$. The situation becomes more complicated if the oscillators provide more degrees of freedom, as in our description of *Chlamydomonas*, equation (4.4). For the coupled flagella, there is a stable limit cycle, surrounding $\delta = \pi$ and $A_L = A_R$, see also figure 4.4 (b).

For the clamped cell, without any rotational freedom, we have $\lambda \approx 0.01$, which is purely through hydrodynamic interactions and more than an order of magnitude weaker than realistic values ($\lambda \approx 0.3$) [133]. See figure 4.4 (c) for the projected dynamics.

4.2.3 The synchronization strength depends on energy efficiency and waveform compliance

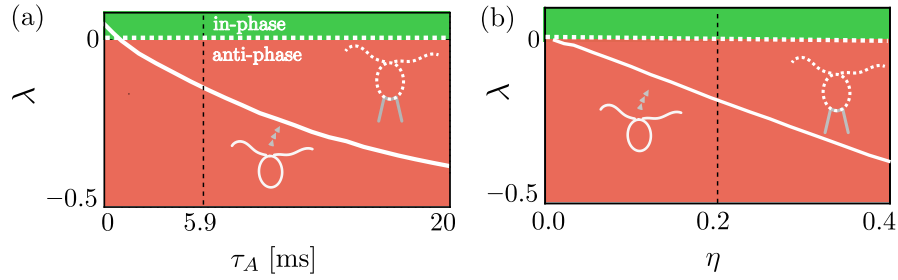


Figure 4.5: *Dependence of intra-flagellar synchronization strength on amplitude relaxation time and energy efficiency.* The simulation results of the freely swimming cell is shown as solid line, the results of the clamped cell is shown as dashed lines. (a) The amplitude stiffness of the flagellum, set by the amplitude correlation time τ_A , changes the synchronization strength λ for the freely swimming cell: inelastic flagella ($\tau_A = 0$) tend to synchronize weakly, whereas elastic flagella, as determined by experiment ($\tau_A = 5.9$ ms) exhibit anti-phase synchronization. For the clamped cell, flagellar stiffness has a small effect on the synchronization strength. In both cases $\eta = 0.2$. (b) For vanishing energy efficiency $\eta = 0$, no synchronization occurs, for increasing values of η , the synchronization strength is decreased and becomes negative, thus we predict anti-phase synchronization ($\tau_A = 5.9$).

Dependence on waveform compliance. For the freely swimming cell, in the limiting case of an inelastic flagellum, $k_A \rightarrow \infty$, which is realized by vanishing amplitude correlation time $\tau_A \rightarrow 0$, we predict an in-phase synchronized state with $\lambda \approx 0.05$. This value is an order of magnitude smaller than the value of the previous description [41], $\lambda \approx 0.56$, which is due to intra-flagellar friction.

For elastic flagella, $\tau_A > 0$, the synchronization strength decreases and becomes negative for a correlation time $\tau_A \gtrsim 1$ ms. In the neighborhood of the experimentally determined value of $\tau_A = 5.9$, anti-phase synchronization $\lambda < 0$ occurs within a stable

limit cycle, see figure 4.4 (b).

The clamped cell performs in-phase synchronization with a very low value in the examined domain $\tau_A \in [0, 20 \text{ ms}]$. This is mainly due to hydrodynamic interactions seem to not play a significant role in synchronization and do not couple in an interesting way to the flagellar amplitude stiffness.

Dependency on energy efficiency. If the energy efficiency is zero, $\eta = 0$, there is no response of the flagellar beat to external load, thus no reaction to fluid flow can occur. Hydrodynamic interactions and the coupling to translational as well as rotational degrees of freedom have no effect on the phase speed $\dot{\varphi}$ and on the amplitude A . Therefore neither in-phase nor anti-phase synchronization can occur. For higher values of η , phases and amplitudes may adapt to cell body movements of hydrodynamic interactions and the synchronization strength decreases linearly, $\lambda < 0$ for $\eta > 0$.

4.2.4 The case of an elastically clamped cell

We can continuously alter the case of a freely rotating cell to a completely clamped one by introducing an elastic coupling of the cell body to a reference orientation $\alpha = 0$ with orientational stiffness k_α .

$$Q_\alpha = -k_\alpha \alpha \quad (4.6)$$

In the limit $k_\alpha = 0$ we mimic the case of a freely rotating cell while translation is not allowed. While this situation may seem artificial, one can use a laser trap for realizing this condition experimentally. For the other limiting case $k_\alpha \rightarrow \infty$ the cell is not allowed to rotate. The clamped *Chlamydomonas* with a micro-pipette is expected to have a large stiffness k_α due to the cell wall that is inherent to plant cells. Figure 4.6 shows the dependence of the synchronization strength on the orientational stiffness. For $k_\alpha \in [10^3, 10^5]$, the synchronization strength is slightly positive, but an order of magnitude lower than experimentally observed values ($\lambda \approx 0.3$) [133]. For $k_\alpha \rightarrow \infty$,

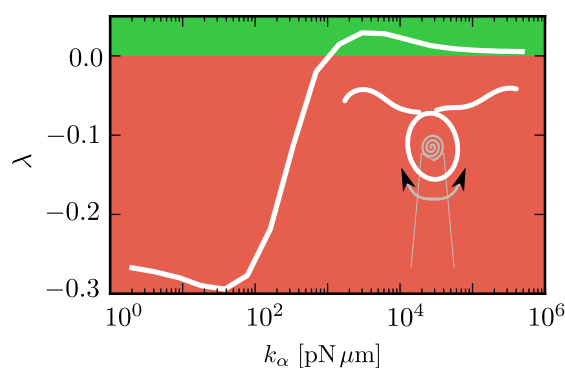


Figure 4.6: *Synchronization strength for an elastically clamped cell.* The case of the completely clamped cell is reproduced for high orientational spring stiffness ($k_\alpha \rightarrow \infty$), while freely rotating but translationally clamped cells ($k_\alpha \rightarrow 0$) perform anti-phase synchronization ($\lambda < 0$).

flagella are coupled only hydrodynamically, such that the value of the synchronization

strength of the completely clamped cell is reproduced $\lambda \rightarrow 0.005$.

The theoretical description is not able to predict experimentally measured values for the synchronization strength of the freely swimming cell and the clamped cell. The elastically clamped cell cannot mimic the case of the clamped cell. This indicates that important ingredients are missing from the theoretical description, as discussed next.

4.2.5 *Basal body coupling facilitates in-phase synchronization*

In this section, direct elastic coupling between the two flagella of *Chlamydomonas* is introduced. It is biologically motivated, see section 1.1.2, and added to the theoretical description of *Chlamydomonas* swimming, because the model so far was not able to reproduce stable flagellar in-phase synchronization and because basal coupling is a recently suggested mechanism [104, 132] for that behavior. First, the theoretical description of basal coupling is introduced. Then, the conditions for stable in-phase synchronization of flagella are discussed. Finally, the transition from stable to unstable flagellar in-phase synchronization is pointed out.

We model this direct coupling as a passive elastic fiber with the elastic energy

$$U_b = \frac{k_b}{2b_1^2}(d_L + d_R - 2d_0)^2 \quad (4.7)$$

with the basal spring stiffness k_b . The typical spatial scale of displacements from the equilibrium position d_0 is b_1 . The distance functions d_l and d_r are proportional to instantaneous values of actual distances of the flagellar anchoring points to d_0 . Those distance functions are unknown and we make a simple ansatz for the form of the functions d_I due to the fact that the flagellar tips positions are periodic functions in φ_I and proportional to the amplitude A_I , $d_I = A_I \sin(\varphi_I - \varphi_0)$ with an unknown phase offset φ_0 . The resulting elastic forces are $C_I = \partial_I U_b$ for $I \in \{\varphi_L, \varphi_R, A_L, A_R\}$ which are dependent on the flagellar degrees of freedom φ_i and A_i .

We need to take into account for this spring force already during the calibration process, see section 3.2.4. Doing so results in an effective form of the elastic force C_I for which the synchronous contribution of C_I is subtracted.

$$\begin{aligned} Q_{\varphi_i}(\varphi_L, \varphi_R, A_L, A_R) &= Q'_{\varphi_i}(\varphi_i) + C_{\varphi_i}(\varphi_L, \varphi_R, A_L, A_R) - C_{\varphi_i}(\varphi_i, \varphi_i, A_i, A_i) \\ Q_{A_i}(\varphi_L, \varphi_R, A_L, A_R) &= Q'_{A_i}(\varphi_i) - k_A(\varphi_i)(A_i - A_0) \\ &\quad + C_{A_i}(\varphi_L, \varphi_R, A_L, A_R) - C_{A_i}(\varphi_i, \varphi_i, A_i, A_i) \end{aligned} \quad (4.8)$$

Two unknown parameters k_b and φ_0 are introduced by the basal spring model extension, which are scanned by performing simulations for each many combinations of tuples (k_b, φ_0) for $k_b \in [0, 6]$ and $\varphi_0 \in [0, 2\pi)$ and obtaining the synchronization strength, which is shown in figure 4.7 for the freely swimming cell, and for the clamped cell.

Conditions for stable in-phase synchronization. We predict regimes in which the freely swimming cell, as well as the clamped cell synchronize their flagella with a synchronization strength that is similar to the experimentally measured values [133]. Note that the synchronization strength λ is π -periodic in the phase offset φ_0 . We find at $\varphi_0 \approx \frac{\pi}{10}$ and $k_b > 3 \text{ pN}\mu\text{m}$ that experimental values can be matched.

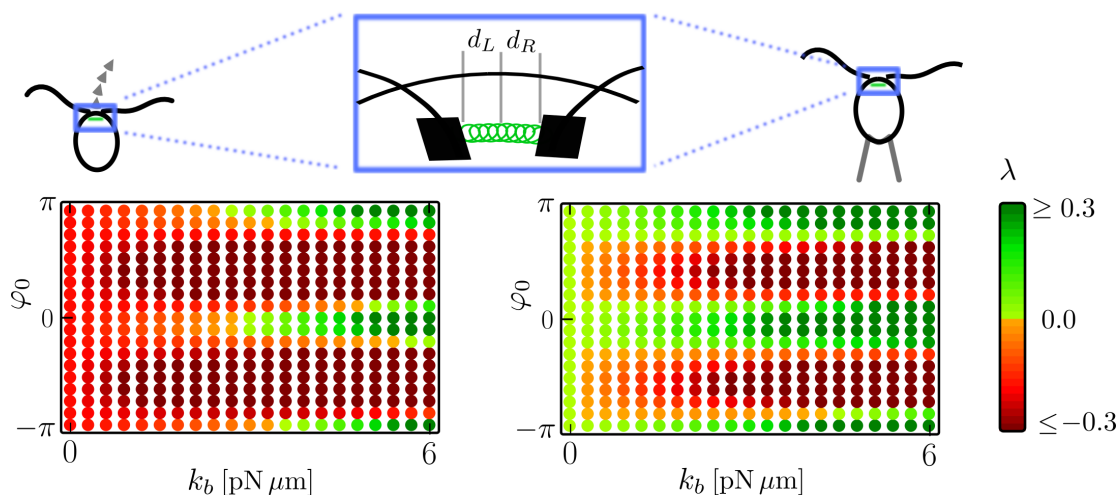


Figure 4.7: *Parameter scan for the basal coupling on synchronization.* Parameter scans are shown for the freely swimming cell (left) and the clamped cell (right). There are regions in which in-phase synchronization occurs for large values of k_b . The synchronization strength λ is π -periodic in φ_0 .

Amplitude compliance and basal elastic coupling are both suggested mechanisms for allowing for stable in-phase synchronization of *Chlamydomonas* flagella. The basal coupling stiffness k_b in *Chlamydomonas* is completely unknown and the determination of the amplitude correlation time τ_A suffers from large measurement errors and cell-to-cell variability. We study the dependence of the synchronization strength on both parameters, τ_A and k_b , while setting the value for the phase offset to $\varphi_0 = \frac{\pi}{10}$. The result is shown in figure 4.8. Without amplitude compliance ($\tau_A = 0$) the effect of basal body coupling on the synchronization strength is negative, thus in-phase synchronization is unstable, for both, freely swimming cells as well as clamped cells. For the freely swimming cell without basal body coupling ($k_b = 0$) in-phase synchronization is unstable as well. Remarkably, the combination of amplitude compliance and basal coupling leads to a positive synchronization strength.

Stable-to-unstable synchronization transition. We investigate the transition from positive to negative values of the synchronization strength for constant $\tau_A = 5.9$ ms while varying the basal stiffness k_b . Therefore, simulations were performed with different initial conditions $\varphi_L(0) = 0$ and $\varphi_R(0) = \delta_0$ with $0 \leq \delta_0 \leq 2\pi$. Note that the dynamics shows transient oscillations and the initial values of the amplitude may 'kick out' the phases, and thus the phase difference δ , from the trajectories that a relaxed oscillation would perform. We thus first perform simulations, in which the phases φ_L and φ_R are constant, but the amplitudes A_L and A_R are relaxed to values, that can then be used as a new set of initial values for the amplitude. With this, we are able to identify stable fixed points and stable limit cycles in the system. Opposing to how we determined the synchronization strength λ in section 4.2.2, here we do not know the exact value of δ^* . Therefore we smoothed the time series $\delta(t)$ near the center of the stable limit cycles δ^* using sliding windows of size T , the period of the flagellar beat. Then we fitted a func-

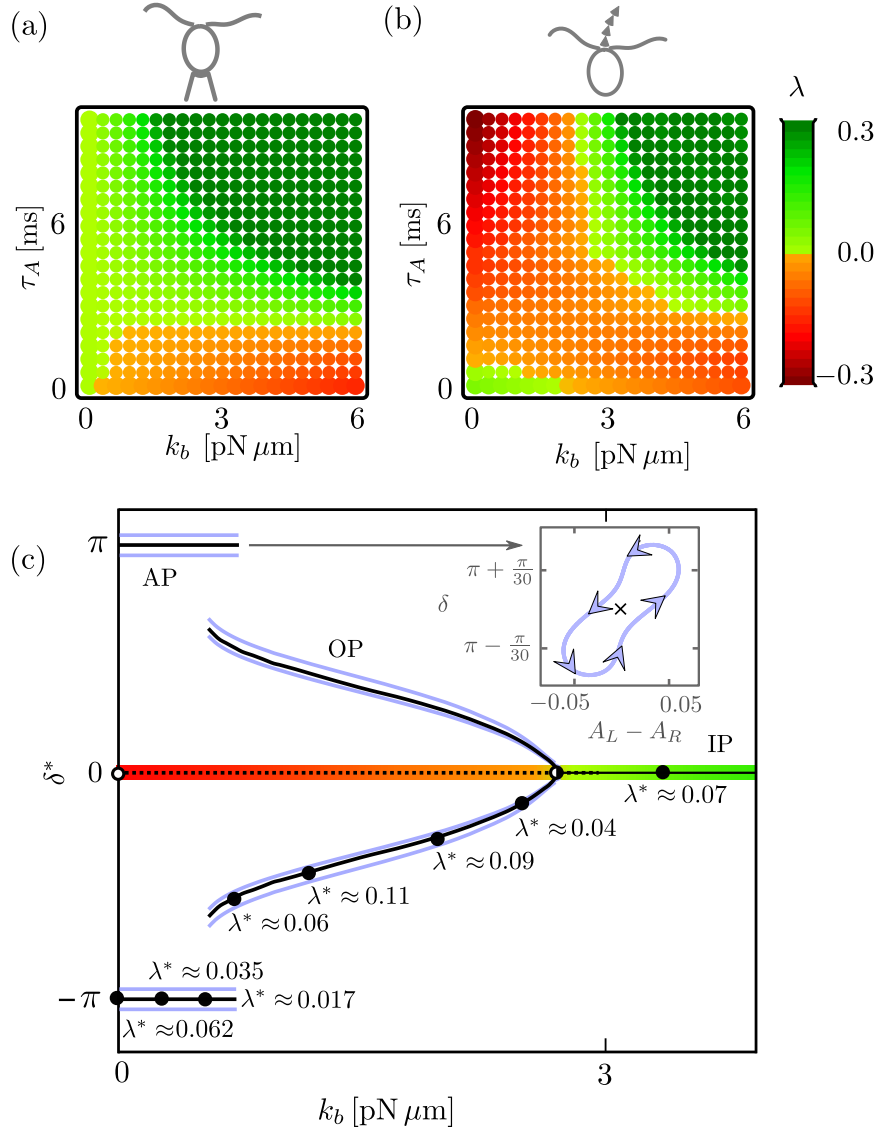


Figure 4.8: *The combination of waveform compliance and basal coupling leads to in-phase synchronization.* (a) The synchronization strength λ as a function of the basal coupling stiffness k_b and amplitude relaxation time τ_A is shown in color code for the clamped cell. (b) Same as (a), but for the freely swimming cell. Only the combination of waveform compliance ($\tau_A > 0$) and basal coupling ($k_b > 0$) results in in-phase synchronization. (c) The black curves show the cycle-averaged values of the phase difference at steady state for varying basal spring stiffness k_b and constant amplitude correlation time τ_A . The light-blue envelope depicts the amplitude of the oscillations of δ . An example of such an oscillation for the anti-phase synchronized state is shown as inset. Specific values of Lyapunov exponents λ^* are shown. The bifurcation diagram shows a pitchfork bifurcation at $k_b \approx 2.7$ pN μm , but instead of a split into three fixed points, one unstable fixed point surrounded by two stable limit cycles remain. A similar bifurcation happens in the interval 0.5 pN $\mu\text{m} < k_b < 0.7$ pN μm , but with an intermediate dynamics in which three stable limit cycles seem to co-exist.

tion $\delta^* + ce^{\lambda^* T^{-1}t}$ for obtaining the limit cycle averages δ^* together with its Lyapunov exponents λ^* . The fixed points and stable limit cycle are shown in figure 4.8 (c).

Remarkably, we find a pitchfork bifurcation at $k_b \approx 2.7 \text{ pN}\mu\text{m}$, in which a stable fixed point ($k_b > 2.7 \text{ pN}\mu\text{m}$) changes into a saddle node, which then splits up into an unstable fixed point at $\delta = \delta_{IP} = 0$ and two stable limit cycles at $\delta = \delta^+ > 0$ and its symmetric counterpart $\delta = \delta^- = -\delta^+$, which is due to the geometric symmetry of the dynamical system. The values δ^- and δ^+ are cycle averaged values of the phase difference at steady state. For smaller values ($k_b \approx 1.2 \text{ pN}\mu\text{m}$) another bifurcation occurs. We did not determine the type of the bifurcation in this region, because unstable limit cycles cannot be identified numerically, reliably. For $k_b = 0$ there is one stable limit cycle at $\delta = \delta_{AP} = \pi$.

We estimate the Young's modulus of the distal striated fiber to be approximately 20 kPa, given its geometry ($300 \text{ nm} \times 2 \cdot 10^4 \text{ nm}^2$) and assuming elongation of the fiber of about $b_1 = 50 \text{ nm}$ from the equilibrium position. This value is the range of Young moduli reported for biological materials [139].

4.2.6 Predictions for experiments

In this section, we propose three experiments that can be used for testing the hypothesis that basal coupling is a crucial mechanism that leads to synchronization in the biological model organism. One is motivated by the experiment, that is described in section 3.1, in which external homogeneous flow is imposed on the surrounding fluid of a clamped cell. An other experiment is similar in the sense that the hydrodynamic load on the flagella is changed, namely the viscosity of the surrounding medium may be changed. Third, we emulate the Calcium concentration within *Chlamydomonas*.

External flow destabilizes in-phase synchronization. With the findings of section 4.2.5, we are able to identify parameter sets, with which we can reproduce values of the synchronization strength λ that are comparable to experimental results. Specific values are for example $k_b = 3.6 \text{ pN}\mu\text{m}$ and $\varphi_0 = \frac{\pi}{10}$, which we use for the next set of numerical simulations.

Motivated by the experiment described in section 3.1, whose measurements were used in the load-response analysis that is, we performed simulations in which a clamped cell is exposed to constant external flow in y -direction. For each flow condition we obtain the synchronization strength. It is clear, that both flagella are in synchrony when the flagellar beat is stalled, see section 3.3.3, but do not synchronize in the sense of the Adler equation, thus we expect the synchronization strength to decrease with increasing external flow speed u . Intuitively spoken, the interactions with the external flow become more important in comparison to other existing couplings, like amplitude deformations with hydrodynamic interactions.

Figure 4.9 shows that for moderate flow speeds, comparable to the speed of the flagellar tip, the synchronization strength λ decreases and even executes anti-phase synchronization $\lambda < 0$ for higher flow speeds. For flow speeds in the surrounding of flagellar stalling, the synchronization strength goes to zero.

While extending this investigation to negative flow speeds would certainly reveal

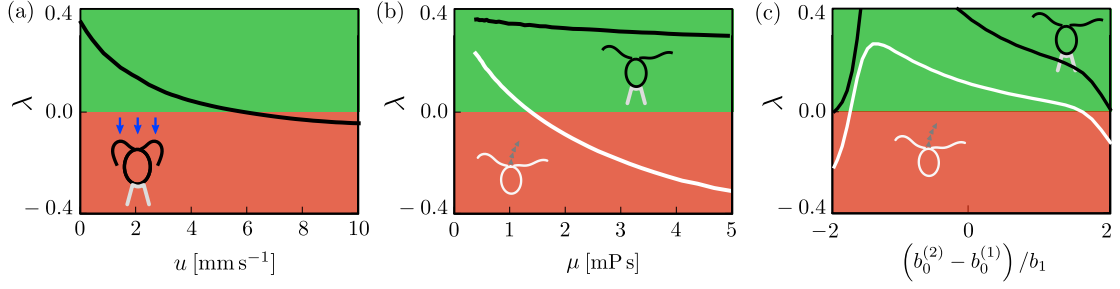


Figure 4.9: *Dependence of synchronization strength on external flow speed viscosity and Calcium concentration considering basal coupling.* Results are shown for basal stiffness $k_b = 3.6 \text{ pN}\mu\text{m}$ and offset $\varphi_0 = \frac{\pi}{10}$. (a) The synchronization strength is reduced with increasing external flow rate and even executes anti-phase synchronization. (b) Simulation results are shown for a freely swimming (white) and a clamped cell (black). (c) The resulting equilibrium distance $d_0^{(2)}$ is different from the one used during the calibration process ($d_0^{(1)}$). Adding *Calcium* to the *Chlamydomonas* cell changes the equilibrium distance of the basal spring.

interesting effects, it is not purposeful to do so, since the computational results of imposing backward flow do not match well with experiments, see section 3.3.3.

Increased viscosity destabilizes in-phase synchronization. External flow from the swimming direction imposes a time-dependent periodic hydrodynamic load on the flagella. Constant changes in the overall load can be achieved by increasing the viscosity of the fluid medium that *Chlamydomonas* is swimming in. Numerical simulations are performed for the clamped as well as for the freely swimming cell.

The hydrodynamic friction matrix $\mathbf{\Gamma}^{(h)}(\mu)$ is proportional to the viscosity μ . The full friction matrix including intra-flagellar friction $\mathbf{\Gamma}^{(i)}$, see section 3.2.3, is

$$\begin{aligned} \mathbf{\Gamma}(\mu, \eta) &= \mathbf{\Gamma}^{(h)}(\mu) + \mathbf{\Gamma}^{(i)}(\eta) \\ &= \frac{\mu}{\mu_0} \mathbf{\Gamma}^{(h)}(\mu = \mu_0) + \frac{1 - \eta}{\eta} \mathbf{\Gamma}^{(h)}(\mu = \mu_0). \end{aligned} \quad (4.9)$$

The driving forces Q_{I_j} , $I \in \{\varphi, A\}$, $j \in \{L, R\}$ and the amplitude stiffness k_A , see equation (3.19), are treated as material properties of flagella, thus are unaffected by a change of viscosity of the surrounding fluid, which means that the calibration of the system at a specific viscosity $\mu = \mu_0$ is used for all other simulations, see section 3.2.4 for details on the calibration process.

The simulation results reveal that the clamped cell is hardly affected by the change of viscosity. The synchronization strength of the freely swimming cell, however, decreases until it reaches anti-phase synchronization for values of the viscosity of $\mu \gtrsim 2 \frac{\text{pNms}}{\mu\text{m}^2}$, see figure 4.9.

A change of Calcium concentration destabilizes in-phase synchronization. If the concentration of *Calcium* in the surrounding of the distal striated fiber is increased, its length decreases [113], see also figure 1.4. In our theoretical description we model the change of the observed length of the distal striated fiber by changing the equilibrium

distance of the basal spring, introduced in equation (4.7), compared to the equilibrium distance during the calibration process. We write the phase and amplitude dependent distances d_L and d_R as

$$d_I(\varphi, A) = b_I(\varphi, A) + d_0^{(1)} \quad (4.10)$$

In the previous calculations, the equilibrium distance $d_0^{(1)}$ had a negligible effect on the synchronization strengths. Here, we first set $2d_0^{(1)}$ to a value that corresponds to the equilibrium distance of the basal spring during the calibration process, see section 3.2.4. Then, for the computations of the synchronization strength λ , we set $d_I = b_I + d_0^{(2)}$. The results are shown in figure 4.9 (c).

Our simulations predict that a contraction of the distal striated fiber stabilizes in-phase synchronization, while extending the fiber destabilizes it. Critical deviation of the ratio $(d_0^{(2)} - d_0^{(1)}) / b_1$ from zero, leads to an unstable fixed point $\delta^* = 0$.

4.3 Summary

In this chapter, we addressed two scenarios of flagellar synchronization relevant for the green alga *Chlamydomonas*. We studied both phase-locking of the flagellar beat to external oscillatory flow, as well as synchronization between the left and right flagellum. For both scenarios, we employed the theoretical description of flagellar dynamics formulated in terms of Lagrangian mechanics developed in the previous chapter 3.

Using the show-case of flagellar synchronization in *Chlamydomonas*, we demonstrated that the load-response of the flagellar beat is a key prerequisite for synchronization of beating flagella by hydro-mechanical coupling. This was shown for a periodic external flow to which the flagellar beat synchronizes if load response is not zero. Our findings are in good agreement with an analogous experiment that was recently performed [104].

We then addressed the case of mutual synchronization of the left and right flagellum in *Chlamydomonas*. Our theory points at a previously missing element for synchronization: We found that our theory accounting for flagellar waveform compliance predicts anti-phase synchronization. Thus, waveform compliance indeed has a profound effect on synchronization as proposed previously on the basis of minimal models, yet our quantitative predictions are opposite to what is observed in experiments.

Recent experiments indicate an important role of an additional structural element, the distal striated fiber that connects the bases of both flagella for synchronization. Incorporating such an elastic link in our theory results in a non-trivial interplay between waveform compliance and basal coupling, resulting in positive synchronization strengths as measured in experiments [133]. Tuning the basal stiffness reveals a rich behavior of flagellar dynamics, such as a pitchfork bifurcation with spontaneous symmetry breaking.

Additionally, we proposed three experiments to test our theory experimentally. First, we considered the case of a clamped cell that is exposed to external flow. In simulations, we observe that the synchronization strength decreases and even becomes negative. Second, the viscosity is varied. Simulation results show a decrease of synchronization

strength up to negative values. Third, our theory predicts that an increase of *Calcium* concentration inside *Chlamydomonas* can also destabilize the in-phase synchronized state.

In this chapter, we mapped the complex dynamics of flagellar synchronization onto the Adler equation with an effective synchronization strength. The Adler equation makes specific predictions on synchronization in pairs of coupled oscillators in the presence of noise, if the strength of noise is known. In the next chapter, we determine the effective flagellar fluctuations of the flagellar beat, in particular the effective phase noise and amplitude noise.

Active flagellar fluctuations

The collective dynamics of molecular motors inside the flagellar axoneme generates regular bending waves, yet also measurable active fluctuations. These fluctuations can be described in terms of a noisy Hopf oscillator with phase and amplitude fluctuations. We discuss implications of flagellar fluctuations on the swimming paths of microswimmers.

Chapter summary. First, the effective description of the flagellar beat as a Hopf oscillator is introduced. Then, the determination of effective noise strengths for the phase and for the amplitude from experimental data is presented. Third, the implications of active flagellar fluctuations on the swimming path of a sperm cell and *Chlamydomonas* is discussed and its effect is compared to the effect of hydrodynamic interactions and thermal noise on a passive particle of the same geometry.

The contribution of the author mainly amounts to section 5.3. For sake of completeness, also the analysis of flagellar fluctuation performed by Benjamin Friedrich is presented in sections 5.1 and 5.2. Most of the chapter's content complies to publication [85] to which the author contributed. High-precision tracking data of swimming bull sperm [108] was recorded by Ingmar Riedel Kruse. Principal Component Analysis has been applied to extract the basic features of the flagellar beat. By the shape mode projection, 95% percent of the variability of the flagellar beat are conserved. The flagellar shape dynamics of freely swimming *Chlamydomonas* cells were previously recorded by Veikko Geyer in the laboratory of Jonathan Howard at MPI CBG and Benjamin Friedrich at MPI PKS developed image analysis algorithms for obtaining the positions of flagellar tracking points [41].

5.1 Effective description of flagellar oscillations

In this chapter we compare the effect of active flagellar noise with hydrodynamic interactions. The shapes of flagella of both microswimmers, sperm cell and *Chlamydomonas*, can be uniquely specified by their time dependent phase φ and amplitude A using the method detailed in section 3.1.4. With this, we map this two dimensional oscillator onto the unit circle, which can be described by a complex oscillator variable

$$Z(t) = A(t) \exp^{i\varphi(t)} \quad (5.1)$$

Previous work described the onset of the flagellar beat as a supercritical Hopf bifurcation [23], whose normal form is written as

$$\dot{Z} = i(\omega_c - \omega_1|Z|^2)Z + \mu(\Lambda - |Z|^2)Z + \Xi \quad (5.2)$$

with amplitude $A = \sqrt{\Lambda}$ and frequency $\omega_0 = \omega_c - \omega_1\Lambda$. The non-isochrony ω_1 describes how the flagellar phase speed changes due to changes in the amplitude, see also section 3.3.4, which is a suggested synchronization mechanism of coupled oscillators [95]. Additionally, we include a complex noise term Ξ for describing active fluctuations. It is multiplicative, i.e. $\Xi = Z(\xi_A + i\xi_\varphi)$ and consists of uncorrelated noise $\langle \xi_i(t)\xi_j(t') \rangle = 2D_j\delta_{jk}\delta(t-t')$ for $i, j \in \{\varphi, A\}$. Equation (5.2) should be interpreted as a Stratonovich stochastic differential equation.

5.2 Measuring flagellar noise

We now present a method to determine the noise strength D_φ and D_A in equation 5.2 from experimental data. Note, that due to the projection of the flagellar beat onto two shape modes, the estimation of the flagellar noise in this section is a lower bound, because noise from neglected shape modes is not considered.

5.2.1 Active phase fluctuations are much larger than thermal noise

Using the limit cycle reconstruction technique that is described in section 3.1.4, a time series of instantaneous flagellar phase $\varphi(t)$ is obtained, well approximated by

$$\dot{\varphi} = \omega + \xi_\varphi. \quad (5.3)$$

We use the phase correlation function H to determine the phase diffusion D_φ , because the phase fluctuations are approximately normally distributed, see figure 5.1 (a).

$$H(t) = \left\langle e^{i[\varphi(t_0-1) - \varphi(t_0)]} \right\rangle_{t_0} \quad (5.4)$$

$$|H(t)| \propto e^{-D_\varphi|t|}$$

Figure 5.1 (b) shows the correlation function and its absolute value and an exponential fit, from which we determine the phase diffusion $D_\varphi \approx 2.8 \text{ s}^{-1}$.

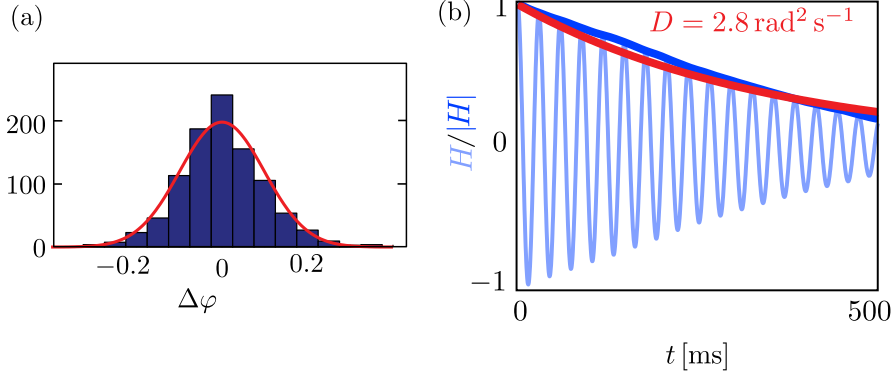


Figure 5.1: *Phase correlation function of flagellar oscillations.* (a) Histogram of phase increments are approximately normally distributed. (b) The correlation function (5.4) represents a damped oscillation with the frequency of the flagellar beat. Its envelope decays roughly as exponential function with a timescale $D_\varphi^{-1} \approx 0.36$ s.

We can compare the measured phase diffusion coefficient to the prediction of the fluctuation-dissipation theorem for a passive system as a result of thermal fluctuations.

$$\begin{aligned} D_\varphi &= \Gamma_{\varphi\varphi} k_B T \approx 0.0015 \text{ s}^{-1} \\ P_\varphi &\approx \Gamma_{\varphi\varphi}^{-1} \dot{\varphi} \end{aligned} \quad (5.5)$$

In fact, the conjugate force P_φ is the sum over all relevant friction terms, for each degree of freedom that sets the state of the microswimmer, but the self-friction $\Gamma_{\varphi\varphi}$ is much larger than the cross terms, so other terms can be neglected for a rough estimate. Note that the active fluctuations are thousand fold larger than thermal noise.

5.2.2 Amplitude fluctuations are correlated

From the Hopf normal form given in equation (5.2), we obtain in the limit of weak noise $D_\varphi, D_A \ll \mu\Lambda$.

$$\langle A(t_0), A(t_0 + t) \rangle_{t_0} - \Lambda \approx \sigma_A^2 \exp(-\tau_A^{-1}|t|) \quad (5.6)$$

The variance $\sigma_A = D_A \tau_A \Lambda$ is proportional to the amplitude diffusion coefficient D_A and the amplitude correlation time $\tau_A = (2\mu\Lambda)^{-1}$. This correlation time is the same that we used to define the amplitude spring stiffness in section 3.2.5. From a fit of the autocorrelation function of amplitude fluctuations, we obtain $\tau_A = (5.8 \pm 1.8)$ ms and $\sigma_A = \langle A(t)^2 \rangle = 0.0070 \pm 0.0023$.

The amplitude noise is described as an Ornstein Uhlenbeck process, which can be understood as a model of a particle that performs Brownian motion within a harmonic potential.

5.3 Active flagellar fluctuations result in noisy swimming paths

We now discuss functional implications of active flagellar fluctuations. Therefore, a noisy dynamics for amplitude and phase fluctuations is prescribed, first for the sperm cell whose effective translational diffusion is determined, then for the *Chlamydomonas* cell, whose diffusion is compared to hydrodynamic interactions and thermal diffusion.

5.3.1 Effective diffusion of swimming circles of sperm cell

We performed hydrodynamic simulations of a swimming sperm cell, prescribing noisy amplitude and phase dynamics. The hydrodynamic simulations are performed via resistive-force theory [50]. Resistive-force theory calculations do not include long range hydrodynamic calculations, which is a good approximation for a sperm cell [38], because the curvature of the flagella is low enough, such that different parts of the cell never come too close to each other.

Note that the amplitude degree of freedom is not affected by external forces. The phase speed is constant besides Gaussian noise and is not influenced by external forces.

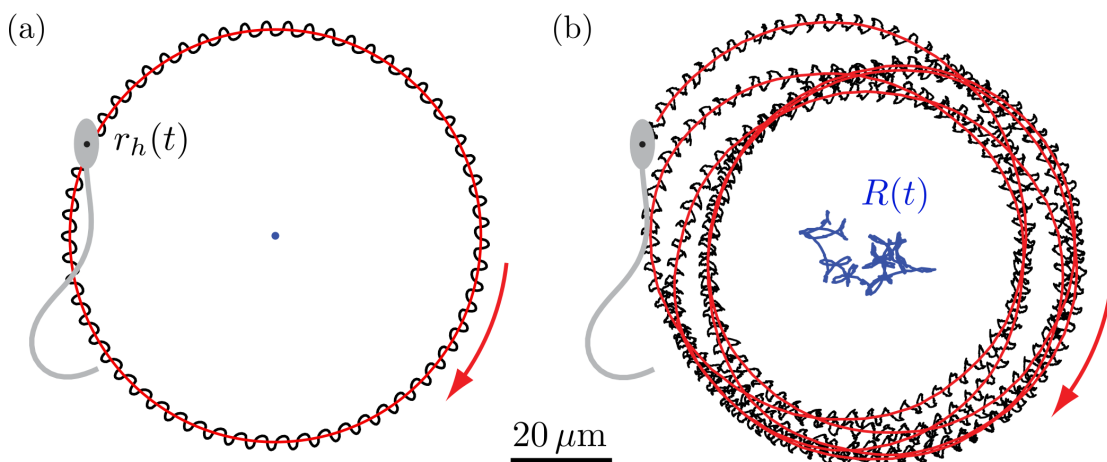


Figure 5.2: *Noisy swimming paths from active fluctuations.* (a) The swimming path of a sperm cell with a flagellum with finite mean curvature and without active fluctuations of the flagellar beat is shown as a black path. The red line represents the circular mean path, whose center is constant. (b) Adding active flagellar fluctuations changes the swimming path and the mean path. The dynamics of the center $R(t)$ is described by effective Brownian motion.

We calculate trajectories $\mathbf{r}_h(t)$ of a freely swimming sperm cell. Its path wiggles periodically from left to right and back while, on average, producing a forward movement. The forward motion is constantly tilted leading to circular swimming paths. In the absence of noise, the mean trajectory lies on a perfect circle with a fixed origin $R(t) = \text{const.}$ With amplitude and phase noise, the centerlines of helical sperm swimming paths become persistent random walks with a persistent length determined by the fluctuation

strength [39]. We determine the effective diffusion coefficient $D_R = (3.30 \pm 0.01) \mu\text{m}^2\text{s}^{-1}$, see also figure 5.2.

If we consider phase noise and do not include amplitude fluctuations, the same trajectory is performed as in the noise-free case. This observation is closely related to the scallop theorem, which states that at least two degrees of freedom are necessary to induce net propulsion. In this case, the phase propagates and fluctuations around the phase cannot lead to a changed trajectory because fluctuations in phase only cause a stochastic re-parameterization in time. This argument would not hold, if the amplitude of the flagellar beat would be a dynamic quantity that reacts to external stimulus, in which case phase fluctuations would induce a diffusive trajectory. This time-reversal symmetry is also broken by including amplitude noise, which causes stochastic swimming paths.

5.3.2 Comparison of the effect of noise and hydrodynamic interactions

We performed hydrodynamic simulations of a swimming Chlamydomonas cell, prescribing noisy amplitude and phase dynamics. The Chlamydomonas swimming is calculated by the fast boundary element method, which is described in appendix A.3. By this, hydrodynamic interactions are considered, which is important for the description of Chlamydomonas swimming cell, since the mean curvature of flagella is rather large and flagella can come very close to the cell body.

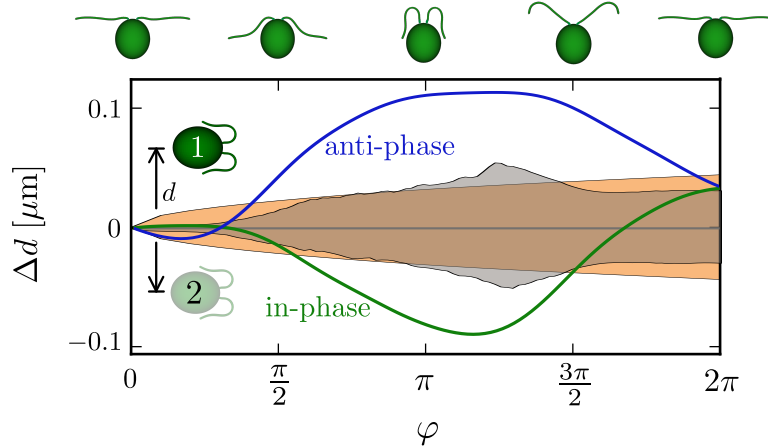


Figure 5.3: Comparison of drags due to active fluctuations and hydrodynamic interactions. Two Chlamydomonas cells that swim next to each other in the same direction, starting with a distance $d = 30 \mu\text{m}$ and interact hydrodynamically with each other. This is compared to thermal diffusive motion of the cell (orange shading) and effective diffusion, resulting from active amplitude fluctuations (gray shading).

Chlamydomonas has two flagella, that in principle can go out of a synchronized state, when they are treated independently. The noise strength or phase diffusion D_φ relates directly to the number of phase slips, that occur while swimming.

In the simulations presented here, a *Chlamydomonas* cell has two independent flagella with prescribed phase speeds $\dot{\varphi} = \omega$ with additional independent noise on the left and the right flagellum. When the two flagella have different phase speeds due to independent phase fluctuations, the cell body changes orientation and translational speeds change, thus leading to different net translations perpendicular to the swimming direction after a period of the flagellar beat. We performed 300 simulations with different seeds for the random number generator. Figure 5.3 shows sideways motion of a single cell due to active flagellar fluctuations as gray shade.

Additionally, figure 5.3 shows sideward motion due to hydrodynamic interactions of two *Chlamydomonas* cells that swim next to each other at an initial distance of $d = 30 \mu\text{m}$ in the swimming plane and the effect of thermal diffusion of a passive particle with the same friction as the *Chlamydomonas* cell. See section 2.2.4 for how simulations of two interacting *Chlamydomonas*'s are performed. The thermal diffusion coefficient is obtained by the Einstein relation $D_d \approx \Gamma_{yy} k_B T$.

We conclude that active fluctuation have a strong impact on the swimming path of *Chlamydomonas*. The net translation perpendicular to the swimming path due to active fluctuations is similar to the one caused by direct hydrodynamic interactions. The effect of thermal diffusion is also at the same range.

5.4 Summary

In this chapter, we presented a description of the flagellar beat as noisy Hopf oscillator. We identified two independent effective noise contributions, one for the phase, the other for the amplitude degree of freedom of the flagellar beat. We found that active flagellar phase fluctuations are much larger than thermal noise and that amplitude fluctuations are correlated.

Using the determined noise strengths, computer simulations were performed to investigate the effect of noise on flagellar swimming paths of a sperm cells and *Chlamydomonas*, which results in noisy swimming with effective diffusion, resulting in displacements that are comparable to the effect of hydrodynamic interactions.

Summary and outlook

In this thesis in theoretical biological physics we addressed swimming and synchronization of flagellated swimmers by investigating three questions:

- What are the flow fields generated beating cilia and flagella?
- In turn, how do external flows feed back on shape and speed of the flagellar beat?
- How does the feedback loop of flagella-generated flow and flow-induced load response of the flagellar beat orchestrate flagellar synchronization in the model organism *Chlamydomonas*?

6.1 *Summary of our results*

Dynamic flow signatures of flagellated swimmers. In chapter 2 we investigated flagellar swimming of microswimmers with a prescribed flagellar beat. We characterized the highly dynamic fluid motion that surrounds the microswimmer by projecting it onto the leading order singularity, which allows for understanding its three dimensional structure. *Chlamydomonas* is commonly considered a typical representative of a puller-like swimmer and the sperm cell as a typical pusher-like swimmer. However, we showed that both microswimmers alternate between pusher-like and puller-like swimming. We estimated at which distance the oscillatory component of the flow will be attenuated due to inertial effects.

External forces change shape and dynamics of the flagellar beat. In a close collaboration with the experimentalists Christian Ruloff and Christian Wagner of the Saarland University, we were able to directly measure the response of the flagellar beat to external fluid flow. Specifically, we quantified the shape of the flagellar beat of

Chlamydomonas cells that were held with a micropipette within a micro-fluidic chamber. The cells were exposed to controlled external flows. These flows feed back onto the shape and speed of the flagellar beat. In chapter 3, we described this load response of the flagellar beat. For completeness, the experimental setup, designed and set up by Christian Ruloff, was described. We then used a dimensionality reduction algorithm to project the flagellar shapes on a two dimensional representation, allowing us to define an effective oscillator phase and amplitude. With this, an effective theory of the flagellar beat was developed, which is calibrated by experimental shape data. Intra-flagellar friction is included in the theoretical description. Furthermore, an amplitude spring provides waveform compliance. By comparing the theoretical prediction with experimental results, we explicitly revealed the load response of the flagellar beat to external load. In section 4.1, we compared experimental results of synchronization with an oscillating external flow with our theoretical predictions of analogous simulations, providing quantitative agreement.

Flagellar synchronization through coupling at the flagellar base. In chapter 4 we investigated the mutual synchronization of the two flagella of Chlamydomonas. The theoretical description developed in 3.2 was extended to allow for different phase dynamics of the two flagella. We used this theoretical framework to explore different synchronization mechanisms, some of which had been previously proposed in minimal models [128, 130]. A prominent, putative synchronization mechanism is amplitude compliance of oscillators [95]. Surprisingly, including an effective waveform compliance in our theory, we found that in-phase synchronization is not stable, opposite to what is observed in experiments. It is known that the proximal bases of both flagella are connected by an elastic link and recent experiments emphasized a role of this basal coupling for synchronization [104, 132]. To test the role of this basal coupling, we extended our theory accordingly. We found that basal coupling without amplitude compliance leads to unstable in-phase synchronization. The combination of amplitude compliance with elastic basal body coupling, however, leads to robust in-phase synchronization as observed in experiments. We suggest three non-invasive experiments for testing the theoretically motivated hypothesis that flagellar synchronization is mediated by a combination of waveform compliance and basal coupling.

6.2 Outlook on future work

Functional consequences of oscillating fluid signature. The flow signature of a single microswimmer has profound consequences on the dynamics of the density distribution of many interacting microswimmers in a suspension [140, 112, 91]. As we showed, the flow signature varies with the cyclic swimming stroke of the microswimmer. It would be interesting to see the consequence of this property on a suspension of interacting agents.

The flows generated by microswimmers also affect the active mixing of tracer particles. Experimental results of displacement probability distributions of tracer particles in a

Chlamydomonas suspension have a Gaussian core and a robust exponential tails [79]. This is explained by the interplay of Brownian motion and advection of motile particles. The oscillatory flow field that we found in chapter 2 indicates that tracer particles near microswimmers do not propagate in simple loops as presented in reference [33], but show also motion on a smaller scale, as observed in reference [79].

Of course, the Stokes doublet has major importance for interactions of a microswimmer with boundaries. From an evolutionary point of view, it might be favorable for some swimmers, being it prey or predators, to swim “quite”, meaning that nearby flows are as small as possible [69].

Generalization of our theoretical description of flagellar swimming and synchronization. The theoretical description that is presented in 3.2 and used in 3.3 and 4 is kept as simple as possible. In fact, it is a linear theory that allows us to make predictions for small perturbations from a reference condition used for model calibration. Within this framework, it is possible to use different parameters for describing the shape of a microswimmer. It does not have to be necessarily flagellated, also ameboidal swimming can be described. Non-planar beats can easily be implemented. Better knowledge of the load-response of the flagellar beat can be used to include a more fine-grained description of the internal processes inside the flagellum and data from experiments with strong perturbations of the flagellar beat may be used to obtain knowledge for constructing a non-linear waveform compliance.

Predictions for experiments of flagellar synchronization. From our theory, we make specific suggestions that can be tested in future experiments, see section 4.2.6: a clamped Chlamydomonas with external flow from the front, a cell in a medium with different viscosity than Chlamydomonas’s normal condition or a cell swimming in a suspension with added Calcium. One may also investigate for higher order synchronization by placing two Chlamydomonas cells next to each other and investigate the synchronization properties of the two pairs individually or with respect to each other. Another mechanism that may play a role for synchronization is an intra-cellular chemical signaling system that interacts with flagella. Different chemical concentrations may lead to different stiffnesses of flagella or the distal striated fiber. The theoretical description used in this thesis could very well be enhanced to consider such properties. Also, in this thesis there were two identical flagella in Chlamydomonas. Further studies may be conducted to allow for different mechanical properties of the *cis* and *trans* flagellum.

Role of noise. While hydrodynamic interactions have been theoretically predicted to give rise to intriguing dynamical effects in collections of microswimmers, active flagellar fluctuations may mask its effects. Large noise levels also inhibit the capability of flagella to synchronize. The number of phase slips increases with the noise strength. Furthermore, swimming paths are affected by noise and can be attributed to effective noise, which opens up the possibility to perform stochastic search strategies such as run-and-tumble motion [7, 99, 39].

Theories of motor control. The flagellar beat emerges from the complex interplay of thousands of molecular motors and cross linker molecules that couple axonemal micro-

tubules. Theories of motor control [117, 6, 82, 56] make predictions on how the flagellar shape dynamics look like, and in principal, can make predictions on how the flagellar shapes are changed due to external forces. Our directly determined susceptibilities of shape deformations and phase speed changes can be used to compare those predictions, thus testing the theories of motor control. For this aim, it could also be interesting to resolve the load response of the flagellar beat in a more fine-grained manner, i.e. by exposing clamped flagellated cells by uniform flows of different directions, or even shear flow profiles.

Metachronal waves in cilia carpets. The insights that we got from this work can further be used to shed light on the emerging dynamics in cilia carpets, which are basically grids of many flagella on epithelial surfaces. They form metachronal waves, i.e. spatio-temporal synchronization patterns with specific phase relations [115]. By the inclusion of elastic or rotational degrees of freedom, one may predict patterns or perturbation responses thereof in biological systems as well as artificial cilia carpets [29].

Appendix A

Solving the Stokes equation

Stokes equation (1.10) describes the physics of fluids in which inertia is neglected against viscous forces. First the multipole expansion is presented and how the flow field can be represented by multipoles. Then resistive-force theory is presented, which describes swimming of slender bodies approximately. Last, the fast multipole boundary element method is briefly sketched.

A.1 Multipole expansion

Force multipole moments can be defined as in reference [118] and [73] via the surface integral

$$\mathbf{f}^{(n+1)} = \frac{1}{n!} \int_S dS \mathbf{r}^n \mathbf{f}(\mathbf{r}), \quad (\text{A.1})$$

where the integration goes over some surface S , \mathbf{f} is a force surface density and \mathbf{r}^n is an outer potency of a position vector \mathbf{r} on the surface, thus \mathbf{r}^n is a rank n tensor. Force multipole moments $\mathbf{f}^{(n+1)}$ are rank $(n+1)$ tensors. Formally, we can write the force density with respect to the force multipoles

$$\mathbf{f}(\mathbf{r}) = \sum_{n=0}^{\infty} (-1)^n \mathbf{f}^{(n+1)} \cdot \nabla^n \delta(\mathbf{r}), \quad (\text{A.2})$$

with the contraction \cdot over all Cartesian coordinates. Generally, products not written with an explicit point mean outer products of tensors.

For testing the validity of (A.2), we first use the definition (A.1) and insert equation (A.2) and see, if we can reproduce $\mathbf{F}^{(n)}$.

$$\begin{aligned} \mathbf{f}^{(n+1)} &= \frac{1}{n!} \int_S \mathbf{r}^n \sum_{m=0}^{\infty} (-1)^m \mathbf{f}^{(m+1)} \cdot \nabla^m \delta(\mathbf{r}) d\mathbf{r} \\ &= \sum_{m=0}^{\infty} \frac{1}{n!} \mathbf{f}^{(m+1)} (-1)^m \int_S \mathbf{r}^n \nabla^m \delta(\mathbf{r}) d\mathbf{r} \\ &= \mathbf{f}^{(n+1)} \left(\int_S \mathbf{r}^n \nabla^m \delta(\mathbf{r}) d\mathbf{r} = \begin{cases} m = n & n!(-1)^n \\ m > n & 0 \\ m < n & m!(-1)^m \int_S \mathbf{r} \delta(\mathbf{r}) d\mathbf{r} = 0 \end{cases} \right) \end{aligned} \quad (\text{A.3})$$

We can insert the formal equation (A.2) into the general solution of the Stokes equation (1.12) to obtain the flow field as a function of force multipoles

$$\begin{aligned} \mathbf{u}(\mathbf{r}) &= \int dV \mathbf{T}(\mathbf{r})\mathbf{f}(\mathbf{r}) \\ &= \sum_{n=0}^{\infty} (-1)^n \mathbf{f}^{(n+1)} \cdot \int dV \mathbf{T}(\mathbf{r}) \nabla^n \delta(\mathbf{r}) \end{aligned} \quad (\text{A.4})$$

n -fold application of partial integration yields

$$\mathbf{u}(\mathbf{r}) = \sum_{n=1}^{\infty} (-1)^n \nabla^n \mathbf{T}(\mathbf{r}) \circ \mathbf{f}^{n+1} \quad (\text{A.5})$$

$\mathbf{u}_{\mathbf{f}}(\mathbf{r})$ is the velocity field that is generated by an exerted force density \mathbf{f} . Since the Taylor expansion was done at a distant point, the first terms are a good approximation of the flow-field that is far away from the origin. The more terms are used, the more accurate are the resulting flow-fields near the force density.

These equations are valid for a force multipoles that are evaluated at the origin $\mathbf{r}' = 0$. Generalizations to multipoles with a distinct origin are straightforward, by using $r_i \rightarrow r_i - r'_i$ in equation (A.1) and $\delta(\mathbf{r}) \rightarrow \delta(\mathbf{r} - \mathbf{r}')$ in equation (A.2).

A.2 Resistive-force theory

Resistive-force theory is a simple approximation for describing hydrodynamic properties of moving slender objects. Global hydrodynamic interactions are not considered. It is assumed that if an object moves, it feels a force, which is linearly coupled to the components perpendicular and parallel to its surface, anisotropically. This is shown in figure A.1.

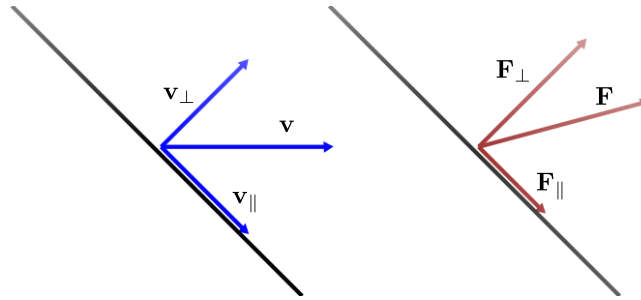


Figure A.1: *Friction anisotropy for the Resistive-Force Theory.* A line, moving from left to right is shown and its velocity as a vector as well as its contributions parallel and perpendicular to the line element. Right: The resulting force vector is tilted because the perpendicular friction is larger than the parallel one.

In the physics of microswimming, usually the method of Gray & Hancock [50] is used. Given the dynamics of the tangent angle $\partial_t \psi(s, t)$, as described in section 2.1.1, it is

possible to calculate the line density $\mathbf{f}(s, t)$ of the force, acting on the flagellum by using resistive-force theory

$$\mathbf{f}(s, t) = \zeta^{\parallel} \mathbf{v}^{\parallel}(s, t) + \zeta^{\perp} \mathbf{v}^{\perp}(s, t) \quad (\text{A.6})$$

where \mathbf{v}^{\parallel} is the component of the velocity, which is parallel to the flagellar shape, thus the projection onto the tangent field $\mathbf{t}(s, t)$, and \mathbf{v}^{\perp} is the projection of the velocity field onto the normal field $\mathbf{n}(s, t)$.

$$\begin{aligned} \mathbf{v}^{\parallel}(s, t) &= (\mathbf{v}(s, t) \cdot \mathbf{t}(s, t)) \mathbf{t}(s, t) \\ \mathbf{v}^{\perp}(s, t) &= (\mathbf{v}(s, t) \cdot \mathbf{n}(s, t)) \mathbf{n}(s, t) \end{aligned} \quad (\text{A.7})$$

The product with the dot means scalar product of vectors. For a bending shape that is clamped at one side, the velocity profile with the resulting resistive force line density is shown in figure A.2.

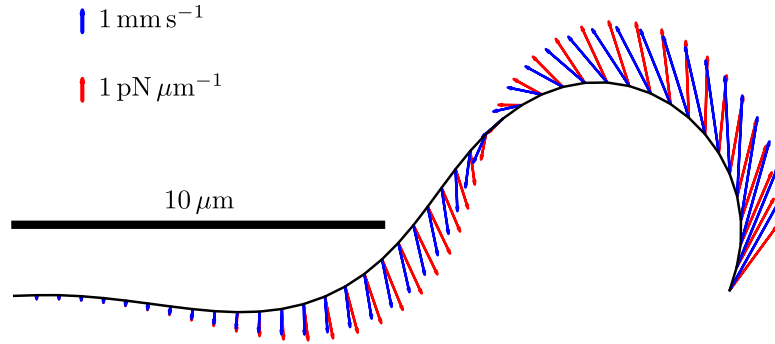


Figure A.2: *Velocity distribution and force density with resistive-force theory.* An example shape of a sperm cell is shown with its velocity profile as blue arrows and the resulting force line density due to viscous friction.

A.3 Fast multipole boundary element method

Here, we sketch key concepts of the fast multipole boundary element method. For a detailed exposition, the reader is referred to Liu [83].

The fast multipole boundary element method can be used to solve either two or three dimensional problems of the form

$$\nabla^2 \phi + f = 0, \quad (\text{A.8})$$

where f is a known function in the domain V and the following boundary conditions are considered.

$$\begin{aligned} \phi &= \bar{\phi} \text{ on } S_{\phi}, \\ q &= \frac{\partial \phi}{\partial n} = \bar{q} \text{ on } S_q, \end{aligned} \quad (\text{A.9})$$

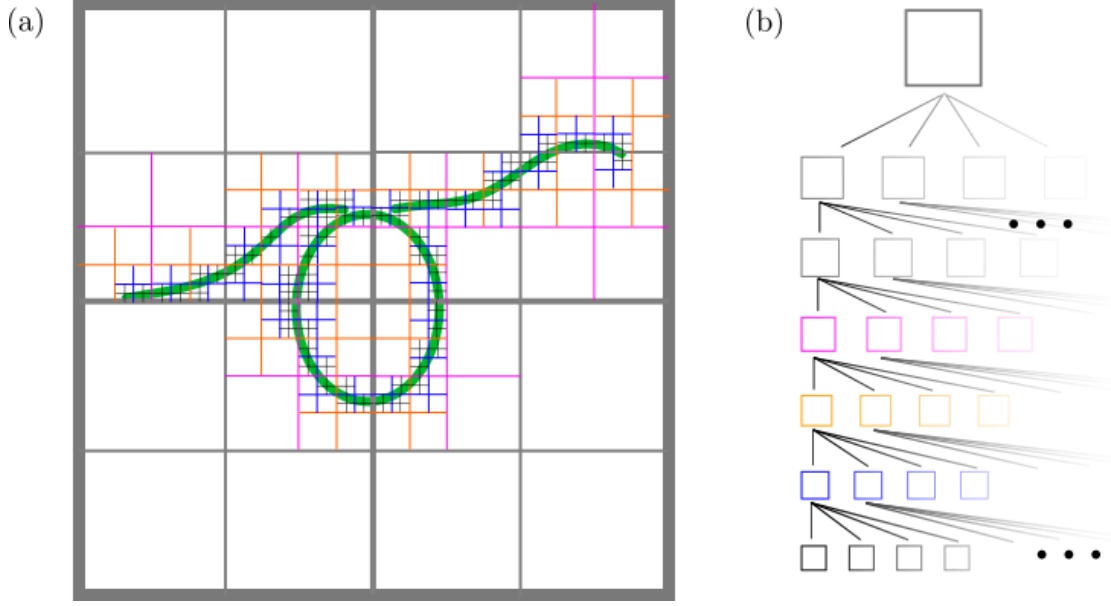


Figure A.3: *Spatial discretization in the fast multiple boundary method.* (a) Two dimensional space is filled with a one dimensional boundary. Starting with one square, determine if a boundary is inside it. If so, divide the square into four equally sized squares filling all of the large square. For each new, smaller square, that procedure is repeated any number of iterations. (b) Space that is discretised as in (a) can be represented as a tree structure, in which every node has either zero or four nodes.

with the outward normal n of the boundary S and $S_\phi \cup S_q = S$. If a fundamental solution $G(\mathbf{x}, \mathbf{y})$ for A.8 exists, we can define $F(\mathbf{x}, \mathbf{y}) = \frac{\partial G(\mathbf{x}, \mathbf{y})}{\partial n(\mathbf{y})}$. It is now possible to write the integral formulation of potential problem

$$c(\mathbf{x})\phi(\mathbf{x}) = \int_S dS(\mathbf{y}) [G(\mathbf{x}, \mathbf{y})q(\mathbf{y}) - F(\mathbf{x}, \mathbf{y})\phi(\mathbf{y})] + \int_V dV(\mathbf{y}) G(\mathbf{x}, \mathbf{y})f(\mathbf{y}), \forall \mathbf{x} \in S. \quad (\text{A.10})$$

After discretising, we arrive at a system of linear equations

$$\begin{aligned} \mathbf{F}\phi &= \mathbf{G}\mathbf{q} \\ \Rightarrow \mathbf{A}\boldsymbol{\lambda} &= \mathbf{b}. \end{aligned} \quad (\text{A.11})$$

The second equation is obtained by switching columns in between the matrices \mathbf{F} and \mathbf{G} , thus $\boldsymbol{\lambda}$ being a vector with mixed components from ϕ and \mathbf{q} . Solving this matrix with the conventional boundary element method requires $\mathcal{O}(N^3)$ operation with the number N of discretization points, because the resulting matrices are dense. With the fast boundary element method, the complexity of the algorithm can be reduced to $\mathcal{O}(N \ln N)$.

The fundamental reason for this to be possible is that we can expand the Green's function at the expansion point \mathbf{y}_c

$$G(\mathbf{x}, \mathbf{y}) = \sum_i G_i^x(\mathbf{x}, \mathbf{y}_c) G_i^y(\mathbf{y}, \mathbf{y}_c). \quad (\text{A.12})$$

With this expansion we are able to write

$$\begin{aligned}
 \int_{S_c} dS(z) G(z_0, z) q(z) &= \frac{1}{2\pi} \sum_{k=0}^{\infty} O_k(z_0 - z_c) M_k(z_c), \\
 &= \frac{1}{2\pi} \sum_{l=0}^{\infty} L_l(z_L) I_l(z_0 - z_L), \\
 M_k(z_c) &= \int_{S_c} dS(z) I_k(z - z_c) q(z), \\
 L_l(z_L) &= (-1)^l \sum_{k=0}^{\infty} O_{kl}(z_l - z_c) M_k(z_c).
 \end{aligned} \tag{A.13}$$

The first expansion is called multipole moment expansion, the latter is called local expansion. The basis functions are polynomials $I_k(z) = \frac{z^k}{k!}$ and $O_k(z) = \frac{(k-1)!}{z^k}$. M_k are called moments and L_l is called moment-to-local translation. Another important equation is the local-to-local translation

$$L_l(z_{L'}) = \sum_{m=0}^{p-l} I_m(z_{L'} - z_L) L_{l+m}(z_L). \tag{A.14}$$

The algorithm for solving potential problems with the fast multipole boundary element method is as follows.

Discretization. The surface of the object has to be discretised. In three dimensional problems, a two dimensional triangulated surface is provided. Example surfaces are shown in figure 2.2.

Tree structure determination. A bounding cube is created that contains all of the object's discretization points. This cube represents the root of the tree structure. The cube is now separated in the following way. If more than a prescribed number of discretization points is inside the cube, it is divided into eight equally sized cubes. Those cubes are child nodes to the cube that contains the cubes. For each cube that procedure is repeated. See figure A.3 (a) for an example in two dimensions, and figure A.3 (b) for the resulting tree. In the following, the cubes are called cells.

Upward pass. For all cells, the moments are computed. First the multipole expansion moments M_k are computed for the points inside the leaf cells, then the moment to moment translation

$$M_k(z'_c) = \sum_{l=0}^k I_{k-l}(z_c - z'_c) M_l(z_c) \tag{A.15}$$

is applied to translate the moments to the next higher cell in the tree structure.

Downward pass. The local expansion coefficients L_l are computed at level two of the discretization tree. Those are passed downward to all children via local-to-local translation, equation (A.14).

Evaluation of the integrals. The integral A.13 is evaluated with the help of moments, moment-to-local and moment-to-moment translations.

Iterations of the solution. An iterative method can be used to solve the eigenvalue problem (A.11), such as Arnoldi-iteration. The unknown vector $\boldsymbol{\lambda}$ is updated and the algorithm is continued at the upward pass, if the solution is not converged within a given tolerance.

Appendix B

Linearized Navier-Stokes equation

The flow-field, that is exerted by an oscillating point force, is derived. In the first part, the underlying hydrodynamic equations are justified. In the second part the case of an oscillating sphere is worked on. Then the limit to vanishing radii is made. At the end, the relation to the greens function of the linearized Navier Stokes equation is shown.

B.1 *Linearized Navier-Stokes equation*

The treatment in this section is conform with [55].

The Navier-Stokes equation has the form

$$\rho(\partial_t \mathbf{u} + \mathbf{u} \cdot \nabla \mathbf{u}) = -\nabla p + \nabla^2 \mathbf{u}, \quad (\text{B.1})$$

with the density ρ , flow field \mathbf{u} and pressure p . We introduce the following dimensionless quantities, by stating that the timescale is independent of the velocity scale.

$$\begin{aligned} t &= \frac{\tilde{t}}{\omega}, \\ \mathbf{r} &= l \tilde{\mathbf{r}}, \\ \mathbf{u} &= U \tilde{\mathbf{u}}, \\ p &= \tilde{p} \frac{\eta U}{l} + p_\infty. \end{aligned} \quad (\text{B.2})$$

Here, we introduced a pressure at infinity p^∞ , a time scale ω^{-1} , spatial scale l and a velocity scale U . Then, equation (B.1) can be rewritten in terms of dimensionless quantities,

$$\begin{aligned} \text{Re}^r \partial_{\tilde{t}} \tilde{\mathbf{u}} + \text{Re}^t \tilde{\mathbf{u}} \cdot \tilde{\nabla} \tilde{\mathbf{u}} &= -\tilde{\nabla} \tilde{p} + \tilde{\nabla}^2 \tilde{\mathbf{u}}, \\ \text{Re}^r &= \frac{l^2 \omega \rho}{\eta}, \\ \text{Re}^t &= \frac{l U \rho}{\eta}. \end{aligned} \quad (\text{B.3})$$

Re^t and Re^r are the *Reynolds* numbers for translational and oscillating effects, respectively¹. When considering an oscillating object, that performs little net propulsion,

¹For microswimmers, that swim very slowly by means of an oscillatory shape change, it is reasonable to assume a vanishing translational *Reynolds* number while considering a non-vanishing oscillatory *Reynolds* number Re^t

it is reasonable to set $\text{Re}^t = 0$, while having non zero Re^f . Doing so in equation (B.3) and back transformation to dimension afflicted quantities leads to the linearized Navier Stokes equation.

$$\rho \dot{\mathbf{v}} = -\nabla p + \eta \Delta \mathbf{u} \quad (\text{B.4})$$

B.2 The case of an oscillating sphere

The explanations in the following two sections follow [74]. A solution to the linearized Navier-Stokes equation is presented for the case of a translationally oscillating sphere. Be the velocity of a sphere $\mathbf{v} = \mathbf{v}_0 e^{-i\omega t}$.

Since the rotation of gradients vanishes, rotating equation (B.4) results in

$$\partial_t(\nabla \times \mathbf{u}) = \eta \Delta(\nabla \times \mathbf{u}) \quad (\text{B.5})$$

The continuity and incompressibility of the fluid leads to the fact, that the velocity field can be written as a rotation $\mathbf{u} = \nabla \times \mathbf{c}$ with the axial Vector \mathbf{c} , which can be represented by a cross product of two polar vectors. The following ansatz for the velocity field is chosen:

$$\begin{aligned} \mathbf{u} &= \nabla \times \mathbf{c} \\ &= \nabla \times (g'(r) \mathbf{n} \times \mathbf{v}) \\ &= e^{-i\omega t} \nabla \times (\nabla g \times \mathbf{v}_0) \end{aligned} \quad (\text{B.6})$$

By using Lagrange's formula $\nabla \times (\nabla \times \mathbf{c}) = \nabla \nabla \mathbf{c} - \nabla^2 \mathbf{c}$, the rotation of the flow-field can be expressed as

$$\nabla \times \mathbf{u} = -\Delta(\nabla \times g\mathbf{v}) = -\Delta(\nabla g \times \mathbf{v}) \quad (\text{B.7})$$

which can be inserted into (B.5), and time derivation can be performed.

$$\begin{aligned} (i\omega \Delta + \eta \Delta^2)(\nabla g \times \mathbf{v}_0) &= 0 \\ \nabla(i\omega \Delta g + \eta \Delta^2 g) &= 0 \\ i\omega \Delta g + \eta \Delta^2 g &= \text{const.} \end{aligned} \quad (\text{B.8})$$

The second equation holds, because \mathbf{u}_0 is constant. The constant in (B.8) is chosen to be zero, due to the boundary condition of the velocity field and all its derivatives to be zero at infinity.

We need an expression of $\partial_r g$, for obtaining the velocity field, therefore obtaining a solution for $\partial_r g$ is sufficient to obtain the flow field (B.6). If we choose the following ansatz, exploiting that g only depends on the radial direction

$$\begin{aligned} \Delta g &= \frac{1}{r^2} \partial_r (r^2 \partial_r) g = a \frac{e^{ikr}}{r} \\ \Rightarrow \partial_r g &= a \frac{e^{ikr}}{r^2} \left(r - \frac{1}{ik} \right) + \frac{b}{r^2}, \end{aligned} \quad (\text{B.9})$$

we can determine the constants a and b with the boundary condition, that the velocity on the sphere surface must be the same as the velocity of the sphere $\mathbf{u}(r = R) = \mathbf{u}$.

$$\begin{aligned} a &= -\frac{3R}{2ik}e^{-ikR}, \\ b &= -\frac{R^3}{2} \left(1 - \frac{3}{ikR} - \frac{3}{R^2k^2} \right). \end{aligned} \quad (\text{B.10})$$

B.3 The small radius limit

We will execute the small radius limit of the previous solution for an oscillating sphere, equation (B.9) with (B.6). We can write the flow field as a function of space and time, parameterized by the radius R of the sphere and the amplitude of the velocity \mathbf{v}_0 . We use Stokes Law to obtain the force acting on the sphere, assuming that the extension of the oscillations are small compared to the positions, at which we evaluate the flow field.

$$\begin{aligned} \mathbf{u} &= \mathbf{u}_{R, \mathbf{u}_0}(\mathbf{r}, t) \\ \mathbf{f}(t) &= 6\pi\eta R \mathbf{u}_0 e^{-i\omega t} = \mathbf{f}_0 e^{-i\omega t} \\ \mathbf{u}_0 &= \frac{\mathbf{f}_0}{6\pi\eta R} \end{aligned} \quad (\text{B.11})$$

Although Stokes law is valid for vanishing Reynolds number, we assume its validity here as well, since we expect corrections to the Stokes equation to happen at a distance of the point force.

With equation (B.11) into (B.6), we find a relation between the amplitude of the force and the flow field. This relation can be used to take the limit to small radii. We then obtain the flow field that is exerted by an oscillating point force.

$$\mathbf{u}_f(\mathbf{r}, t) = \lim_{R \rightarrow 0} \frac{e^{-i\omega t}}{6\pi\eta R} \nabla \times (\nabla \times \mathbf{f}_0 g) \quad (\text{B.12})$$

When using appropriate abbreviations, the flow field, that is exerted by an oscillating point force, with $\mathbf{f}_0 = (1, 0, 0)$ can be expressed as

$$\begin{aligned} v_x &= \frac{\mathcal{E} e^{-i\omega t}}{8\pi\eta r} \left[(1 - i\mathcal{D})i + (1 + 3i\mathcal{D}) \frac{x^2}{r^2} \right], \\ v_y &= \frac{\mathcal{E} e^{-i\omega t}}{8\pi\eta r} (1 + 3i\mathcal{D}) \frac{xy}{r^2}, \\ v_z &= \frac{\mathcal{E} e^{-i\omega t}}{8\pi\eta r} (1 + 3i\mathcal{D}) \frac{xz}{r^2}, \\ \mathcal{E} &= e^{(i-1)\frac{r}{\delta}}, \\ \mathcal{D} &= \left(\frac{\delta}{r} \right)^2 \left[\frac{1}{\mathcal{E}} - 1 - (1 - i)\frac{r}{\delta} - (1 - i)^2 \left(\frac{r}{\delta} \right)^2 \right], \\ \delta &= \sqrt{\frac{2\eta}{\rho\omega}}. \end{aligned} \quad (\text{B.13})$$

Analogous expressions are obtained with forces $\mathbf{f}_1 = (0, 1, 0)$ and $\mathbf{f}_2 = (0, 0, 1)$. Due to the linearity of the linearized Navier-Stokes equation (B.4), velocity fields can be linearly superposed, and the flow field of arbitrary oscillating forces $\mathbf{f} = (f_x, f_y, f_z) = f_x \mathbf{f}_0 + f_y \mathbf{f}_1 + f_z \mathbf{f}_2$ can be obtained, which allows us to write

$$\begin{aligned} \mathbf{u}(\mathbf{r}, t) &= \mathcal{G}(\mathbf{r}, \omega) \mathbf{f} e^{-i\omega t} \\ \mathcal{G}_{ij} &= \frac{\mathcal{E}}{8\pi\eta r} \left[(1 - i\mathcal{D}) \delta_{ij} + (1 + 3i\mathcal{D}) \frac{r_i r_j}{r^2} \right] \end{aligned} \quad (\text{B.14})$$

Note that the Green's function \mathcal{G} is not explicitly time dependent. As shown in the next section, this is a valid property of \mathcal{G} .

B.4 Greens function

It is shown that the Green's function for the hydrodynamics of oscillating force densities can in fact be written as a function that does not depend on time, although general time dependent motion would enforce explicit time dependence of \mathcal{G} .

Equation (B.4) is a linear equation, thus a Green's function \mathcal{G} exists, such that $\mathcal{G}_{ij} f_{0j}$ solves the inhomogeneous linearized Navier-Stokes equation:

$$\rho \dot{\mathbf{u}}(\mathbf{r}, t) + \nabla p(\mathbf{r}, t) - \eta \Delta \mathbf{u}(\mathbf{r}, t) = \mathbf{f}_0 \delta(\mathbf{r}, t) \quad (\text{B.15})$$

Let us consider the problem of a force density $\mathbf{f}(\mathbf{r})$ on the time varying surface $S(t)$ of a body.

$$\mathbf{u}(\mathbf{r}, t) = \int_{-\infty}^t dt' \int_{S(t')} dS \mathcal{G}_{ij}(\mathbf{r} - \mathbf{r}', t - t') f_j(\mathbf{r}', t') \quad (\text{B.16})$$

say, this body performs an oscillation, that is small compared to the distances at which we want to evaluate the flow field: $r' \ll r$. The movement can be written as: $\mathbf{f}(\mathbf{r}, t) = \mathbf{f}(\mathbf{r}) e^{-i\omega t}$.

$$\begin{aligned} \mathbf{u}(\mathbf{r}, t) &= \int_{-\infty}^t dt' \mathcal{G}_{ij}(\mathbf{r}, t - t') \int_{S(t')} dS f_j(\mathbf{r}', t') \\ &= \int_{-\infty}^t dt' \mathcal{G}_{ij}(\mathbf{r}, t - t') \int_{S(t')} dS f_j(\mathbf{r}) e^{-i\omega t'} \\ &= \int_{-\infty}^t dt' \mathcal{G}_{ij}(\mathbf{r}, t - t') F_j e^{-i\omega t'} \end{aligned} \quad (\text{B.17})$$

The integral can be decomposed into two integrals with the limits $\int_{-\infty}^t = \int_{-\infty}^{\infty} - \int_t^{\infty}$. The second term vanishes, because forces are not propagated backward in time, or in

formulas: $\mathcal{G}_{ij}(\mathbf{r}, t) = 0$, for $t < 0$. It follows, that inside the time integral the time can be translated arbitrarily, and time reflections may occur.

$$\begin{aligned}
 \mathbf{u}(\mathbf{r}, t) &= \int_{-\infty}^{\infty} dt' \mathcal{G}_{ij}(\mathbf{r}, t - t') F_j e^{-i\omega t'} \\
 &= \int_{-\infty}^{\infty} dt' \mathcal{G}_{ij}(\mathbf{r}, t') F_j e^{i\omega t'} e^{-i\omega t} \\
 &= \tilde{\mathcal{G}}_{ij}(\mathbf{r}, \omega) F_j e^{-i\omega t}
 \end{aligned} \tag{B.18}$$

which is the same expression as the first equation of (B.14) for the far field.

Appendix C

Hydrodynamic friction

C.1 *A passive particle*

In Stokes flow, forces and velocities depend linearly on each other due to the linearity of Stokes equation. A spherical particle that translates with the velocity \mathbf{v} exerts the force

$$\begin{aligned}\mathbf{F} &= \zeta_t \mathbf{v} \\ \zeta_t &= 6\pi\mu a\end{aligned}\tag{C.1}$$

on the surrounding fluid, with translational friction coefficient ζ_t . Equation (C.1) is called Stokes law for a translating sphere. The radius of the sphere is a and the surrounding medium has viscosity μ . A very similar law exists for rotational movement $\boldsymbol{\omega}$ that leads to a torque

$$\begin{aligned}\boldsymbol{\tau} &= \zeta_r \boldsymbol{\omega} \\ \zeta_r &= 8\pi\mu a^3\end{aligned}\tag{C.2}$$

with the rotational friction coefficient ζ_r .

If the immersed particle is not a sphere, we need to take into account that an applied force at the particle may induce an angular motion and an applied torque may lead to a velocity. With composite vectors $\boldsymbol{\mathcal{U}} = (\mathbf{v}, \boldsymbol{\omega})$ and $\boldsymbol{\mathcal{P}} = (\mathbf{F}, \boldsymbol{\tau})$, the friction $\boldsymbol{\zeta}$ can be expressed as a 6×6 -matrix and couples forces and velocities by

$$\boldsymbol{\mathcal{P}} = \begin{pmatrix} \zeta_{tt} & \zeta_{tr} \\ \zeta_{rt} & \zeta_{rr} \end{pmatrix} \boldsymbol{\mathcal{U}}.\tag{C.3}$$

Here, ζ_{tt} relates the translational quantities \mathbf{F} and \mathbf{v} to each other, ζ_{rt} relates the rotational movement $\boldsymbol{\omega}$ to the translational force \mathbf{F} and so forth.

Generally, the friction matrix $\boldsymbol{\zeta} = \boldsymbol{\zeta}(S)$ depends on the shape S of the particle. Just for very few cases, analytic expressions for $\boldsymbol{\zeta}$ are available. A useful formula for the friction of a prolate as well as a oblate ellipsoid is derived by Perrin [98].

C.2 *Multiple Particles*

When multiple particles are immersed into the fluid, their movements will affect each other by means of hydrodynamic interactions. This can be elegantly expressed in a hydrodynamic friction matrix \mathcal{Z} , when we define the multi particle velocity $\mathcal{V} =$

$(\mathbf{u}_1, \dots, \mathbf{u}_n)$ and the multi particle force $\mathcal{F} = (\mathcal{P}_1, \dots, \mathcal{P}_n)$ for an immersion with n particles, with composite velocities $\mathbf{u}_i = (\mathbf{v}_i, \boldsymbol{\omega}_i)$ and $\mathcal{P}_i = (\mathbf{F}_i, \boldsymbol{\tau}_i)$

$$\mathcal{F} = \mathcal{Z}\mathcal{V}$$

$$\mathcal{Z} = \begin{pmatrix} \zeta_{11} & \zeta_{12} & \cdots & \zeta_{1n} \\ \zeta_{21} & & \ddots & \vdots \\ \vdots & & & \\ \zeta_{n1} & \zeta_{n2} & \cdots & \zeta_{nn} \end{pmatrix}. \quad (\text{C.4})$$

Now, ζ_{ij} describes hydrodynamic interactions between particle i and j . Those interactions are different for different spatial configuration of the particles. That means, if another particle k , has a different positions, the hydrodynamic interactions ζ_{ij} will change. Self couplings ζ_{ii} , that are interpreted as in equation (C.3) ($\zeta_{ij} \in \mathbb{R}^{6 \times 6}$), will change, too.

There are different methods for computing approximations to the friction matrix \mathcal{Z} , like the method of reflection [55], which is an iterative method that converges to the physical solution, or the Rodne-Prager approximation, which is an instance of the method of reflection with just two iterations.

In this work I will generate friction matrices with the help of the fast multipole boundary element method, as described in appendix A.3.

C.3 Generalized coordinates

Expressing the dissipation rate, equation (2.19), in terms of a discretized surface and in terms of a linearly related set of coordinates, such as the generalized coordinates introduced in section 4.2.1, gives us a computational recipe for calculating friction matrices in terms of those coordinates.

Be $S(t)$ a surface that is triangulated into N triangles, see section 2.1.2. The positions of the triangle centers are collected in a mesh position vector $\mathbf{S} = (\mathbf{r}_1, \dots, \mathbf{r}_N)^T$. The boundary condition is then represented as $\dot{\mathbf{S}} = (\mathbf{v}(\mathbf{r}_1), \dots, \mathbf{v}(\mathbf{r}_N))^T$. The force surface density can be represented similarly: $\mathbf{f}_S = (\mathbf{f}(\mathbf{r}_1), \dots, \mathbf{f}(\mathbf{r}_N))^T$. It is then possible to find a linear relation \mathbf{L} that maps any generalized velocity $\dot{\mathbf{q}}$ into a mesh velocity $\dot{\mathbf{S}}$ and, since Stokes flow is a linear equation, we can also find a linear map \mathbf{K} between mesh velocities $\dot{\mathbf{S}}$ and force surface density collection \mathbf{f}_S .

$$\begin{aligned} \dot{\mathbf{S}} &= \mathbf{L} \cdot \dot{\mathbf{q}} \\ \mathbf{f}_S &= \mathbf{K} \cdot \dot{\mathbf{S}} \end{aligned} \quad (\text{C.5})$$

Here, \mathbf{L} is a $3N \times M$ matrix, where M is the number of generalized coordinates, thus the number of components of $\dot{\mathbf{q}}$. With this, the dissipation rate \mathcal{R} can also be written as

$$\begin{aligned} \mathcal{R} &= \dot{\mathbf{S}}^T \cdot \mathbf{f}_S = \dot{\mathbf{S}}^T \cdot \mathbf{K} \cdot \dot{\mathbf{S}} \\ &= \dot{\mathbf{q}}^T \cdot \mathbf{L}^T \cdot \mathbf{K} \cdot \mathbf{L} \cdot \dot{\mathbf{q}} \\ &= \dot{\mathbf{q}}^T \cdot \boldsymbol{\Gamma} \cdot \dot{\mathbf{q}} \end{aligned} \quad (\text{C.6})$$

$$\begin{aligned}\mathbf{\Gamma} &= \mathbf{L}^T \cdot \mathbf{K} \cdot \mathbf{L} \\ \Gamma_{ij} &= L_{i\gamma}^T K_{\gamma\beta} L_{\beta j} = \mathcal{L}_i^T \cdot \mathcal{K}_j\end{aligned}\tag{C.7}$$

Latin indices are used as indices for the generalized coordinates whereas Greek symbols describe the indices that refer to specific components inside the mesh. The change of a generalized coordinate δq_i corresponds to a velocity profile \mathcal{L}_i on the triangulated surface. This in turn is imposed by traction force \mathcal{K}_i .

Appendix D

Data analysis methods

D.1 *Nematic filter*

The nematic filter is an edge detection algorithm that we use to track flagellar shapes from experimental data [90]. It takes an image $I : \mathbb{R}^2 \rightarrow \mathbb{R}$ and converts it into a nematic field, that we express as a nematic strength field $|n| : \mathbb{R}^2 \rightarrow \mathbb{R}$ and a directional field $\phi : \mathbb{R}^2 \rightarrow \mathbb{R}$. First, nemats and a possible representation of it are introduced. Then formulas are presented for computing a nematic field from an image.

D.1.1 *Nemat*

A nemat is a mathematical structure, which can be thought of a vector without an arrow head. Given a nemat, we are given a direction, but without a sign. Thus, a rotation of a nemat by an angle of π leads to the same nemat. This property can be fulfilled by a traceless symmetric matrix

$$\mathbf{n} = \begin{pmatrix} n_{xx} & n_{xy} \\ n_{xy} & -n_{xx} \end{pmatrix} = |n| \begin{pmatrix} \cos(2\phi) & \sin(2\phi) \\ \sin(2\phi) & -\cos(2\phi) \end{pmatrix} \stackrel{!}{=} \mathfrak{R}(\pi)\mathbf{n}\mathfrak{R}(-\pi) \quad (\text{D.1})$$

The nemat in two dimensional can be described by two quantities: The orientation ϕ , which can be obtained by $\phi = \frac{1}{2} \arctan\left(\frac{n_{xy}}{n_{xx}}\right)$, and its length $|n| = \sqrt{n_{xx}^2 + n_{xy}^2}$.

D.1.2 *Nematic correlation*

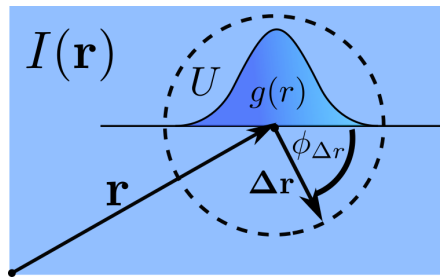


Figure D.1: *Nematic transformation*. For position \mathbf{r} the intensity field I is evaluated in the environment U . The intensities are weighted with a nematically deformed Gaussian kernel g , see equation (D.2).

An edge is a region of similar intensity of a scalar field with an aspect ration that differs from one. Thus, it can be obtained by a weighted correlation, in the following

way

$$\begin{aligned}
 n_{xx}(\mathbf{r}) &= I(\mathbf{r}) \int d\Delta r g(\Delta r) \sin(2\phi_{\Delta r}) I(\mathbf{r} + \Delta \mathbf{r}) \\
 n_{xy}(\mathbf{r}) &= I(\mathbf{r}) \int d\Delta r g(\Delta r) \cos(2\phi_{\Delta r}) I(\mathbf{r} + \Delta \mathbf{r}) \\
 g(r) &= \exp^{-\frac{r^2}{\lambda^2}}
 \end{aligned} \tag{D.2}$$

The image I is represented as a function of two dimensional space. The image is convoluted with a quenched Gaussian kernel $g(\Delta \mathbf{r}) \cdot (\sin(2\pi_{\Delta \mathbf{r}}), \cos(2\pi_{\Delta \mathbf{r}}))$, such that noise due to pixelation or other dirt is removed and the nematic property is fulfilled.

D.2 Principal-component analysis

Principal-component analysis (PCA) is a method for classifying a dataset by a reduced number of parameters. It is also called a dimensionality reduction method, because the state of the system can be described by a point in a state space with lower dimensionality. An interesting application of PCA is the classification of shapes, such as flatworms, cells within tissues or cilia and flagella [134]

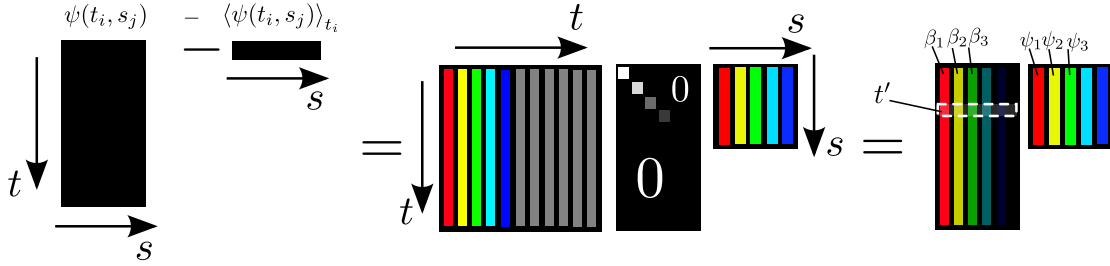


Figure D.2: Principal component analysis of the mean shape.

We can write m observations of n features of a system as a data matrix $\Delta \in \mathbb{R}^{n \times m}$, which can be decomposed via singular-value decomposition.

$$\Delta = \mathbf{U}^* \mathbf{S} \mathbf{V} \tag{D.3}$$

\mathbf{U} and \mathbf{V} are unitary matrices, and \mathbf{S} is a diagonal matrix. An advantage of this decomposition is, that for many systems, many entries of \mathbf{S} are very small, letting us neglect their contributions. Equation (D.3) in index notation reads as

$$\Delta_{ij} = U_{ik}^* S_{kl} V_{lj} = S_{il}^* V_{lj}. \tag{D.4}$$

For an exact treatment, the summation over l must be done for $l = 1, \dots, m$, but the ordering of the components of \mathbf{S} and the generalized rotations \mathbf{U} and \mathbf{V} are in such a way, that we are allowed to consider less terms for a similarly accurate description. The number of modes to consider is specific to the problem at hand and the accurateness obliged.

D.3 The quality of the limit-cycle projections of experimental data

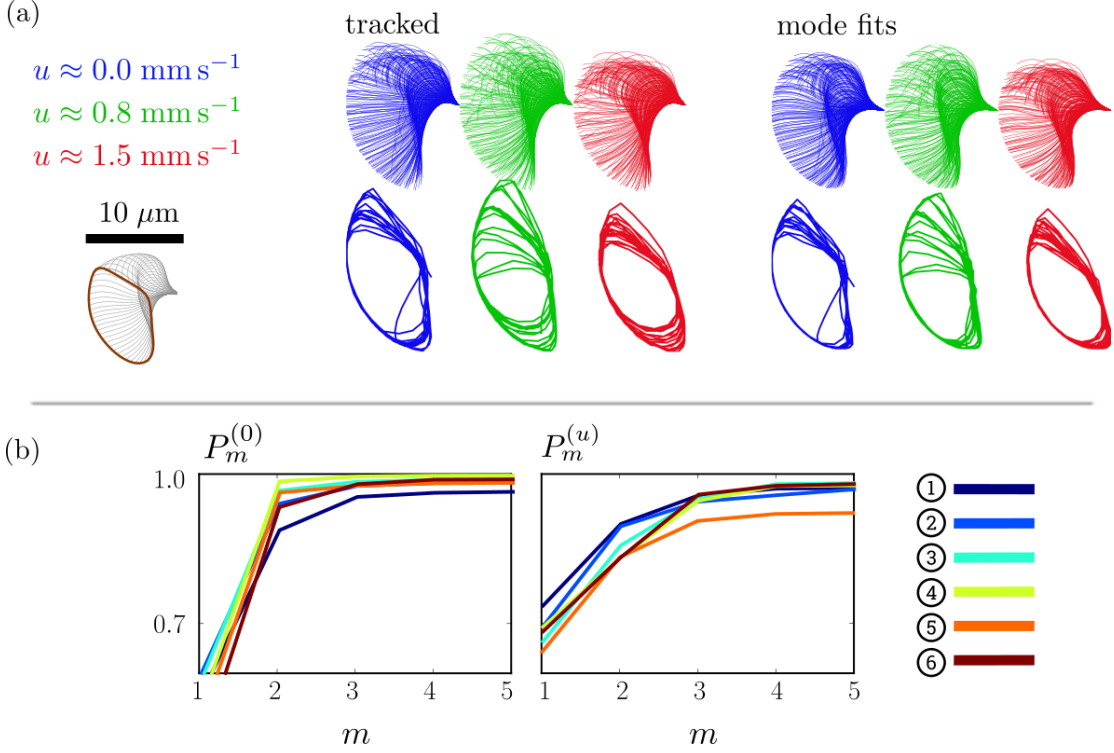


Figure D.3: Comparison of tracked shape and shape projections on two shape modes. (a) For three different flow speeds exemplary shapes are shown with the trajectories of the flagellar tip below it. (b) $\langle (\psi)^2 \rangle$ is a measure for the shape variance. Top: We see that for two modes ($m = 2$) about 90% of the shape variance can be reproduced. Bottom: With two modes, it is possible to map about 80% of the shape deformations due to external load.

The quality of the approximation of the projected shapes $\psi^{(m)}$ onto the tracked shapes ψ is quantified by comparing the variances

$$P_m^{(0)} = \frac{\langle (\psi^{(m)} - \psi_0)^2 \rangle}{\langle (\psi - \psi_0)^2 \rangle} \quad (\text{D.5})$$

Similarly, we quantify to what extent the projected shape changes capture the load-response

$$P_m^{(u)} = \frac{\langle (\psi_{u=u_0}^{(m)} - \psi_{u=0}^{(m)})^2 \rangle}{\langle (\psi_{u=u_0} - \psi_{u=0})^2 \rangle} \quad (\text{D.6})$$

with the number of modes m that are used to approximate the shape. For $m \rightarrow \infty$ the reproduced shape would be identical to the originally tracked ones, thus $P_\infty^{(i)} \rightarrow 1$.

Figure D.3 shows the projection qualities for low values of m . Considering just two modes, faithfully represent the measured shape and capture the load-response of the flagellar beat.

Appendix E

Adler equation

The Adler equation is derived for the case of two weakly interacting oscillators L and R with generic coupling. The oscillators intrinsic frequencies are ω_L and ω_R are coupled by generic coupling function d and b . The dynamics of the phases φ_L and φ_R is follows

$$\begin{aligned}\dot{\varphi}_L &= \omega_L + d(\varphi_L, \varphi_R) \\ \dot{\varphi}_R &= \omega_R + b(\varphi_L, \varphi_R)\end{aligned}\tag{E.1}$$

For simplicity and because it holds for the theoretical description in section 4, we assume $\omega_L = \omega_R$. We also set $b(\varphi_L, \varphi_R) = d(\varphi_R, \varphi_L)$, meaning that interchanging φ_L with φ_R leads to the same equations. We write the dynamics of the phase lag $\delta = \varphi_L - \varphi_R$ as follows.

$$\dot{\delta} = d(\varphi_L, \varphi_R) - d(\varphi_R, \varphi_L)\tag{E.2}$$

and decompose the coupling term d into Fourier modes since it is periodic in the phases φ_L and φ_R .

$$\begin{aligned}d(\phi_1, \phi_2) &= \sum_{n=0}^{\infty} D_n(\varphi_1) \sin(n\varphi_2) + E_n(\varphi_1) \cos(n\varphi_1) \\ D_n(\varphi) &= \sum_{m=0}^{\infty} D'_{nm} \sin(m\varphi) + D''_{nm}(\varphi) \cos(m\varphi) \\ E_n(\varphi) &= \sum_{m=0}^{\infty} E'_{nm} \sin(m\varphi) + E''_{nm}(\varphi) \cos(m\varphi)\end{aligned}\tag{E.3}$$

Let's now consider just the first two Fourier mode and plug those into equation (E.2).

$$\begin{aligned}\dot{\delta} &\approx A (\sin(\varphi_L) - \sin(\varphi_R)) + B (\cos(\varphi_L) - \cos(\varphi_R)) \\ &+ C (\sin(\varphi_L) \cos(\varphi_R) - \cos(\varphi_L) \sin(\varphi_R)) \\ &= 2A \cos(\bar{\varphi}) \sin\left(\frac{\delta}{2}\right) - 2B \sin(\bar{\varphi}) \cos\left(\frac{\delta}{2}\right) + C \sin(\delta)\end{aligned}\tag{E.4}$$

The following shorthands were used: $A = E'_{01} - D''_{10}$, $B = E''_{01} - E'_{10}$, $C = E'_{11} - D''_{11}$, $\bar{\varphi} = \frac{\varphi_L + \varphi_R}{2}$.

The crucial assumption for the Adler equation to hold is that the coupling is weak, which means that the dynamics of the phase φ_L and φ_R or equivalently $\bar{\varphi}$ are much faster than the dynamics of the phase lag δ . We apply that assumption to equation (E.5) by treating $\bar{\varphi}$ and δ as independent variables and averaging out the fast dynamics

$\dot{\varphi}$. Thus, the first two terms of equation (E.5) vanish and the famous Adler equation comes out.

$$\dot{\delta} = -\lambda \sin(\delta) \tag{E.5}$$

If the synchronization strength $\lambda = -C$ is positive, there is stable in-phase synchronization between the two oscillators, if $\lambda < 0$, in-phase synchronization is unstable but anti-phase synchronization is stable.

Appendix F

Sensitivity analysis for computational results

F.1 *The distance function of basal coupling*

As we see in section 4.2.5, the synchronization strength λ depends on the details of the distance functions d_L and d_R . It is not obvious if the distance functions d_i should depend on the amplitude A_i or not. Figure F.1 shows the synchronization strength for different offset φ_0 and basal spring stiffnesses k_b for two different variants of the distance function $d_b = d_L + d_R$.

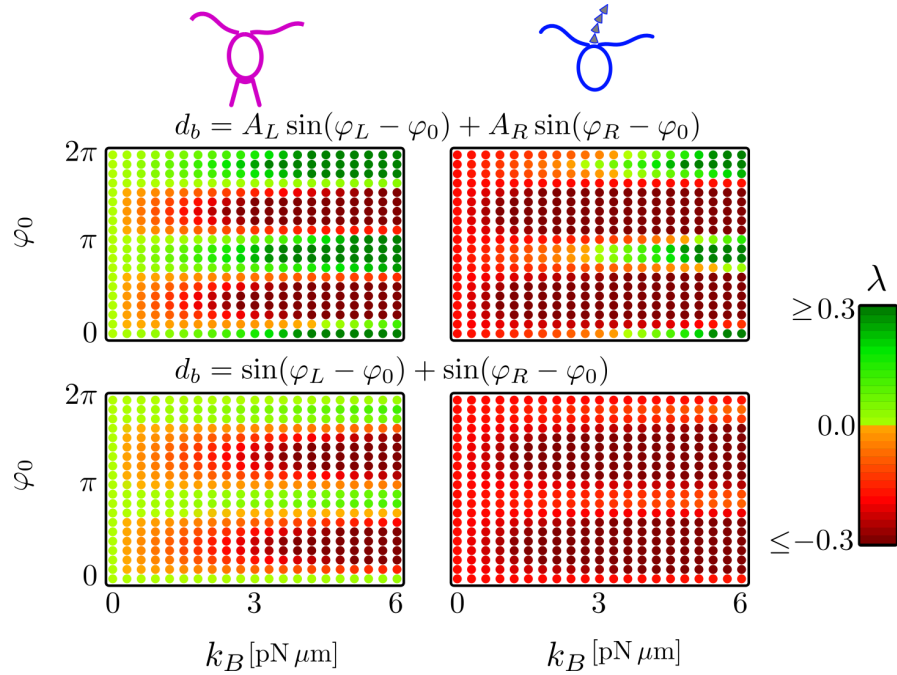


Figure F.1: *Parameter scans for the synchronization strength for two different distance functions.* (top) Amplitude dependent distance function. (bottom) Amplitude independent distance function. (left) clamped cell. (right) freely swimming cell.

We observe that the dependence of the synchronization strength λ on the offset φ_0 and the basal coupling stiffness k_b is qualitatively similar, but larger values of k_b are necessary to obtain the same values for λ for the case of the distance function that is independent of the amplitude.

F.2 Computed synchronization strength for alternative waveform

Here, we compare the synchronization properties of a cell with different flagellar shapes. The synchronization strength is shown in figure F.2, analogously to figure 4.7. The qualitative features of the synchronization strength match well with the shape data used in section 4.2.5. We observe that the phase offset φ_0 is shifted, which is due to a phase shift from using a different set of shape modes. Note also that quantitative agreement would be obtained by using values for the basal coupling constant k_b double as large as was used for the cell from section 4.2.5.

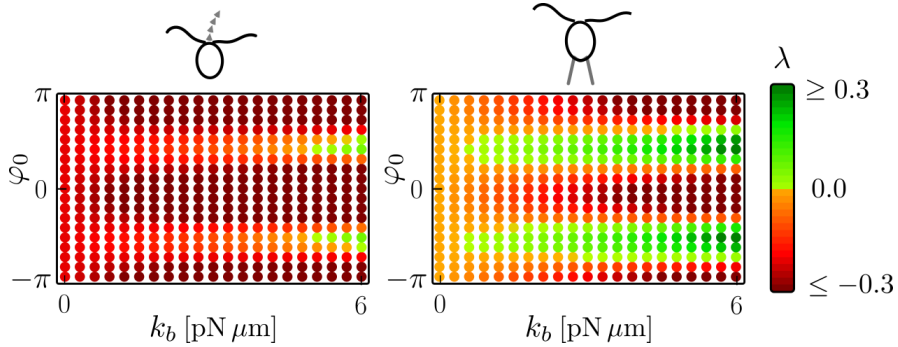


Figure F.2: *Distance function parameter scan for different shape data.* (left) freely swimming cell. (right) clamped cell.

F.3 Insensitivity of computed load-response to amplitude correlation time

Simulation as in section 3.3.2 were performed, in which external flow is imposed on a clamped cell, but with different values of the amplitude correlation time τ_A , as well as phase dependent $\tau_A(\varphi)$. Except for very low values of $\tau_A \approx 1$ ms, the susceptibilities χ_φ and χ_A are qualitatively similar and within a range of 80% with respect to the case $\tau_A = 5.9$ ms.

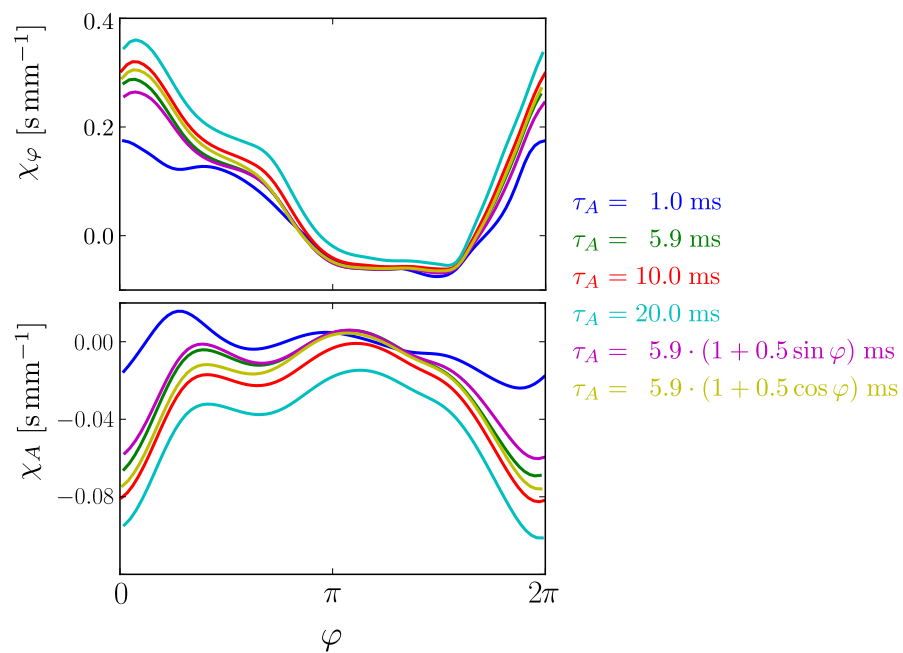


Figure F.3: *Low sensitivity of load-response to change of amplitude correlation time.* The load-response as in section 3.3.2, figure 3.10 for different as well as for phase dependent values of the amplitude correlation time τ_A .

List of Symbols

A	amplitude of the flagellar beat
α	relative orientation of the force dipole with respect to microswimmer orientation
A_0	equilibrium value of the flagellar amplitude, see section 3.2.5
b_1	length scale of displacements of basal bodies from their equilibrium distance d_0 , see equation (4.7)
β_i	flagellar shape score coefficient to mode ψ_i
C_i	elastic force from basal body coupling, see section 4.2.5
δ	phase difference, or phase lag $\varphi_L - \varphi_R$
Δ	fluid strain, symmetrized spatial derivative of the flow vector field
d_L, d_R	distance functions of basal coupling, see equation (4.7)
d_0	equilibrium distance from flagellar anchoring point to basal-body center, see equation (4.7)
D_A	amplitude diffusion, see section 5.1
D_φ	phase diffusion, see section 5.1
δ_s	inertial screening length, see equation (2.14)
η	energy conversion efficiency, see section 3.2.3
ϵ	force dipole planarity, see equation (2.11)
\mathbf{f}	force surface density
\mathbf{F}	force acting on a microswimmer
φ	flagellar phase
f	frequency of the flagellar beat
$\mathbf{f}^{(2)}$	force dipole, see equation (2.10)
f_s	force dipole strength, see equation (2.11)
u	frequency of external periodic flow
$\mathbf{f}^{(n)}$	force multipole of order n , see equation (1.13)

$\mathbf{\Gamma}$	friction matrix in generalized coordinates
\mathcal{G}	Green's function for the Navier-Stokes equation, see equation (2.15)
$\mathbf{\Gamma}^{(h)}$	hydrodynamic friction matrix in generalized coordinates
$\mathbf{\Gamma}^{(i)}$	intra-flagellar friction matrix in generalized coordinates
k_A	amplitude spring stiffness, see equation (3.19)
k_b	elastic coupling constant between basal bodies of Chlamydomonas
K_t, K_φ	flagellar curvature, see section 3.3.1
λ	synchronization strength of a system of two coupled oscillators
μ	dynamic viscosity
$\mathbf{\Omega}$	orientation of microswimmer
\mathcal{P}	composite vector of force and torque
\mathbf{P}	vector of generalized forces due to friction
p	pressure field
$\mathbf{\Pi}$	stress tensor, see equation (1.6)
ψ	tangent angle of the flagellar shape, see equation (2.1)
ψ_0	mean bending of the flagellar tangent angle
ψ_i	flagellar shape mode number i or principal mode
\mathbf{Q}	vector of generalized active forces
\mathbf{q}	state vector or vector of generalized coordinates, see section 3.2.1
Q_A	flagellar amplitude constraining force, see section 3.2.4
Q_φ	flagellar phase driving force, see section 3.2.4
$\dot{\mathbf{q}}^{\text{ref}}$	reference dynamics for the clamped cell, see equation (3.5)
ρ	mass volume density
\mathcal{R}	energy dissipation rate, see section 2.4
\mathfrak{R}	rotation matrix
Re	Reynolds number, see equation (1.8)
s	arclength

σ	force dipole symmetry, see equation (2.12)
S	surface of microswimmer
\mathbf{T}	Oseen tensor, Greens function of the Stokes equation
θ	protophase, periodic quantity, not necessarily proportional to time
t	time
$\boldsymbol{\tau}$	torque acting on microswimmer
τ_A	amplitude correlation time, see equation (3.17)
\mathbf{U}	composite vector of velocity and angular velocity
\mathbf{u}	fluid flow field
u	external flow speed on a clamped Chlamydomonas cell
$\mathbf{u}^{(n)}$	flow field, generated by a force multipole $\mathbf{f}^{(n)}$, see equation (1.14)
\mathbf{v}	velocity of microswimmer
$\boldsymbol{\omega}$	angular velocity of microswimmer
ω	mean frequency of the flagellar beat
ξ_A	effective amplitude noise, contributes to active flagellar noise, see section 5.1
ξ_φ	effective phase noise, contributes to active flagellar noise, see section 5.1
χ_A	linear susceptibility of flagellar amplitude to external flow speed, see section 3.3.2
χ_φ	linear susceptibility of flagellar phase speed to external flow speed, see section 3.3.2
y	generalized coordinate for translation in the model of synchronous swimming, see section 3.2
ζ	grand friction matrix, see section 2.1.4

List of Figures

1.1	Ciliated microswimmers	2
1.2	The architecture of the axoneme	4
1.3	Schematic of how the microscopic structure of the flagellar axoneme leads to bending oscillations	6
1.4	Distal striated fiber in the basal apparatus of green alga is contractile	7
1.5	Minimal model of hydrodynamic synchronization in the presence of amplitude compliance	9
1.6	Stokeslet: the fundamental solution of the Stokes equation	12
1.7	Example of how the leading-order multipole dominates the far-field	13
1.8	Breaking time reversal symmetry with two degrees of freedom: The push-me-pull-you stroke	14
1.9	Flow-signatures of puller- and pusher-type swimmers	15
2.1	Tangent angle representation of flagellar shapes	20
2.2	Triangulated surface of microswimmers studied in this thesis	22
2.3	Grand friction matrix of <i>Chlamydomonas</i>	24
2.4	Constraining forces and swimming velocity of <i>Chlamydomonas</i>	25
2.5	Computed flow field exerted by a freely swimming <i>Chlamydomonas</i> cell	26
2.6	Radial projection of the far field of a freely swimming <i>Chlamydomonas</i> cell	27
2.7	Characterization of 3D Stokes doublet flow signatures	29
2.8	Constant swimmer signature of a bacterium	29
2.9	Phase-dependent swimmer signature of a <i>Chlamydomonas</i> cell	30
2.10	Phase-dependent swimmer signature of a sperm cell	31
2.11	Time dynamics of inter-swimmer distance for a pair of hydrodynamically interacting <i>Chlamydomonas</i> cells	33
2.12	Stability diagram for the relative orientation of two <i>Chlamydomonas</i> cells in two different spatial arrangements	34
2.13	Oscilet and doscilet dynamics	35
2.14	Computed hydrodynamic mid- and far-field of <i>Chlamydomonas</i>	36
2.15	Phase dependent dissipation rate	38
3.1	Experimental setup	42
3.2	Flow through the micro-fluidic chamber	44
3.3	The main steps of the flagellar tracking algorithm	45
3.4	Flow-diagram of flagellar tracking algorithm	46
3.5	Limit cycle construction	47
3.6	Three contributions to limit cycle changes	49
3.7	Generalized friction matrix and generalized forces	51

3.8	Amplitude stability of the flagellar oscillator	55
3.9	Mean flagellar curvature as a function of flow rate	57
3.10	Phase dependent phase speed and amplitude susceptibility	58
3.11	Flagellar stalling at high load and higher modes	61
3.12	Flagellar stalling in experiment and theory	62
3.13	Non-isochrony	63
4.1	Arnold tongue of flagellar synchronization to periodic driving for different energy efficiencies	66
4.2	Hydrodynamic friction matrix components in generalized coordinates, phases and amplitudes	70
4.3	Hydrodynamic friction matrix components in generalized coordinates: remaining coordinates	71
4.4	Synchronization of clamped and freely swimming cell	72
4.5	Dependence of intra-flagellar synchronization strength on amplitude relaxation time and energy efficiency	73
4.6	Synchronization strength for an elastically clamped cell	74
4.7	Parameter scan for the basal coupling on synchronization	76
4.8	The combination of waveform compliance and basal coupling leads to in-phase synchronization	77
4.9	Dependence of synchronization strength on external flow speed viscosity and Calcium concentration considering basal coupling	79
5.1	Phase correlation function of flagellar oscillations	85
5.2	Noisy swimming paths from active fluctuations	86
5.3	Comparison of drags due to active fluctuations and hydrodynamic interactions	87
A.1	Friction anisotropy for the Resistive-Force Theory	96
A.2	Velocity distribution and force density with resistive-force theory	97
A.3	Spatial discretization in the fast multiple boundary method	98
D.1	Nematic transformation	111
D.2	Principal component analysis of the mean shape	112
D.3	Comparison of tracked shape and shape projections on two shape modes	113
F.1	Parameter scans for the synchronization strength for two different distance functions	117
F.2	Distance function parameter scan for different shape data	118
F.3	Low sensitivity of load-response to change of amplitude correlation time	119

Bibliography

- [1] R. Adler. A study of locking phenomena in oscillators. *Proceedings of the IRE*, 34(6):351–357, 1946.
- [2] B. Alberts, A. Johnson, J. Lewis, M. Raff, K. Roberts, and P. Walter. *Molecular Biology of the Cell (Garland Science, New York, 2002)*. 1997.
- [3] J. Alper, V. Geyer, J. Howard, et al. Reconstitution of flagellar sliding. *Methods in Enzymology*, 524:343–369, 2013.
- [4] J. Avron, O. Kenneth, and D. Oaknin. Pushmepullyou: an efficient micro-swimmer. *New Journal of Physics*, 7(1):234, 2005.
- [5] C. B. Barber, D. P. Dobkin, and H. Huhdanpaa. The quickhull algorithm for convex hulls. *ACM Transactions on Mathematical Software*, 22(4):469–483, 1996.
- [6] P. Bayly and K. Wilson. Analysis of unstable modes distinguishes mathematical models of flagellar motion. *Journal of The Royal Society Interface*, 12(106):20150124, 2015.
- [7] R. R. Bennett and R. Golestanian. Emergent run-and-tumble behavior in a simple model of chlamydomonas with intrinsic noise. *Physical Review Letters*, 110(14):148102, 2013.
- [8] R. R. Bennett and R. Golestanian. A steering mechanism for phototaxis in chlamydomonas. *Journal of The Royal Society Interface*, 12(104):20141164, 2015.
- [9] H. C. Berg and R. A. Anderson. Bacteria swim by rotating their flagellar filaments. *Nature*, 1973.
- [10] S. A. Berman, N. F. Wilson, N. A. Haas, and P. A. Lefebvre. A novel map kinase regulates flagellar length in chlamydomonas. *Current Biology*, 13(13):1145–1149, 2003.
- [11] B. A. Bradley and L. M. Quarmby. A nima-related kinase, cnk2p, regulates both flagellar length and cell size in chlamydomonas. *Journal of Cell Science*, 118(15):3317–3326, 2005.
- [12] C. Brennen and H. Winet. Fluid mechanics of propulsion by cilia and flagella. *Annual Review of Fluid Mechanics*, 9(1):339–398, 1977.
- [13] C. Brokaw. Adenosine triphosphate usage by flagella. *Science*, 156(3771):76–78, 1967.

- [14] C. Brokaw. Effects of viscosity and atp concentration on the movement of reactivated sea-urchin sperm flagella. *Journal of Experimental Biology*, 62(3):701–719, 1975.
- [15] C. Brokaw. Calcium-induced asymmetrical beating of triton-demembrated sea urchin sperm flagella. *The Journal of Cell Biology*, 82(2):401–411, 1979.
- [16] C. J. Brokaw. Bend propagation by a sliding filament model for flagella. *Journal of Experimental Biology*, 55(2):289–304, 1971.
- [17] C. J. Brokaw. Flagellar movement: a sliding filament model. *Science*, 178(4060):455–462, 1972.
- [18] C. J. Brokaw. Direct measurements of sliding between outer doublet microtubules in swimming sperm flagella. *Science*, 243(4898):1593, 1989.
- [19] N. A. Brown and L. Wolpert. The development of handedness in left/right asymmetry. *Development*, 109(1):1–9, 1990.
- [20] D. R. Brumley, M. Polin, T. J. Pedley, and R. E. Goldstein. Metachronal waves in the flagellar beating of volvox and their hydrodynamic origin. *Journal of The Royal Society Interface*, 12(108):20141358, 2015.
- [21] D. R. Brumley, K. Y. Wan, M. Polin, and R. E. Goldstein. Flagellar synchronization through direct hydrodynamic interactions. *eLife*, 3:e02750, 2014.
- [22] K. H. Bui, H. Sakakibara, T. Movassagh, K. Oiwa, and T. Ishikawa. Asymmetry of inner dynein arms and inter-doublet links in chlamydomonas flagella. *The Journal of Cell Biology*, 186(3):437–446, 2009.
- [23] S. Camalet and F. Jülicher. Generic aspects of axonemal beating. *New Journal of Physics*, 2(1):24, 2000.
- [24] S. Camalet, F. Jülicher, and J. Prost. Self-organized beating and swimming of internally driven filaments. *Physical Review Letters*, 82(7):1590, 1999.
- [25] R. A. Cardullo and J. M. Baltz. Metabolic regulation in mammalian sperm: mitochondrial volume determines sperm length and flagellar beat frequency. *Cell Motility and the Cytoskeleton*, 19(3):180–8, jan 1991.
- [26] Z. Carvalho-Santos, J. Azimzadeh, J. B. Pereira-Leal, and M. Bettencourt-Dias. Tracing the origins of centrioles, cilia, and flagella. *The Journal of Cell Biology*, 194(2):165–175, 2011.
- [27] R. S. Cathcart and W. C. Worthington. ciliary movement in the rat cerebral ventricles: clearing action and directions of currents*+. *Journal of Neuropathology & Experimental Neurology*, 23(4):609–618, 1964.

- [28] D. T. Chen, M. Heymann, S. Fraden, D. Nicastro, and Z. Dogic. Atp consumption of eukaryotic flagella measured at a single-cell level. *Biophysical Journal*, 109(12):2562–2573, 2015.
- [29] N. Coq, A. Bricard, F.-D. Delapierre, L. Malaquin, O. Du Roure, M. Fermigier, and D. Bartolo. Collective beating of artificial microcilia. *Physical Review Letters*, 107(1):014501, 2011.
- [30] G. Corkidi, B. Taboada, C. Wood, A. Guerrero, and A. Darszon. Tracking sperm in three-dimensions. *Biochemical and Biophysical Research Communications*, 373(1):125–129, 2008.
- [31] H. C. Crenshaw, C. N. Ciampaglio, and M. McHenry. Analysis of the three-dimensional trajectories of organisms: estimates of velocity, curvature and torsion from positional information. *Journal of Experimental Biology*, 203(6):961–982, 2000.
- [32] K. Drescher, R. E. Goldstein, N. Michel, M. Polin, and I. Tuval. Direct measurement of the flow field around swimming microorganisms. *Physical Review Letters*, 105(16):168101, 2010.
- [33] J. Dunkel, V. B. Putz, I. M. Zaid, and J. M. Yeomans. Swimmer-tracer scattering at low Reynolds number. *Soft Matter*, 6(17):4268, 2010.
- [34] G. J. Elfring and E. Lauga. Hydrodynamic phase locking of swimming microorganisms. *Physical Review Letters*, 103(8):088101, 2009.
- [35] J. Elgeti and G. Gompper. Emergence of metachronal waves in cilia arrays. *Proceedings of the National Academy of Sciences*, 110(12):4470–4475, 2013.
- [36] J. Elgeti, U. B. Kaupp, and G. Gompper. Hydrodynamics of sperm cells near surfaces. *Biophysical Journal*, 99(4):1018–1026, 2010.
- [37] J. Elgeti, R. G. Winkler, and G. Gompper. Physics of microswimmers: single particle motion and collective behavior: a review. *Reports on Progress in Physics*, 78(5):056601, 2015.
- [38] B. Friedrich, I. Riedel-Kruse, J. Howard, and F. Jülicher. High-precision tracking of sperm swimming fine structure provides strong test of resistive force theory. *Journal of Experimental Biology*, 213(8):1226–1234, 2010.
- [39] B. M. Friedrich. Search along persistent random walks. *Physical biology*, 5(2):026007, 2008.
- [40] B. M. Friedrich. Hydrodynamic synchronization of flagellar oscillators. *The European Physical Journal Special Topic*, pages 2353–2368, 2016.
- [41] V. F. Geyer, F. Jülicher, J. Howard, and B. M. Friedrich. Cell-body rocking is a dominant mechanism for flagellar synchronization in a swimming alga. *Proceedings of the National Academy of Sciences*, 110(45):18058–18063, 2013.

- [42] V. F. Geyer, P. Sartori, B. M. Friedrich, F. Jülicher, and J. Howard. Independent control of the static and dynamic components of the chlamydomonas flagellar beat. *Current Biology*, 26(8):1098–1103, 2016.
- [43] S. Ghose and R. Adhikari. Irreducible representations of oscillatory and swirling flows in active soft matter. *Physical Review Letters*, 112(11):118102, 2014.
- [44] I. Gibbons. The relationship between the fine structure and direction of beat in gill cilia of a lamellibranch mollusc. *The Journal of Biophysical and Biochemical Cytology*, 11(1):179–205, 1961.
- [45] I. Gibbons and A. Rowe. Dynein: a protein with adenosine triphosphatase activity from cilia. *Science*, 149(3682):424–426, 1965.
- [46] S. Gluzman, D. A. Karpeev, and L. V. Berlyand. Effective viscosity of puller-like microswimmers: a renormalization approach. *Journal of The Royal Society Interface*, 10(89):20130720, 2013.
- [47] R. E. Goldstein, M. Polin, and I. Tuval. Noise and synchronization in pairs of beating eukaryotic flagella. *Physical Review Letters*, 103(16):168103, 2009.
- [48] R. Golestanian and A. Ajdari. Analytic results for the three-sphere swimmer at low reynolds number. *Physical Review E*, 77(3):036308, 2008.
- [49] J. Gray. *Ciliary movement*. Cambridge University Press, 1928.
- [50] J. Gray and G. Hancock. The propulsion of sea-urchin spermatozoa. *Journal of Experimental Biology*, 32(4):802–814, 1955.
- [51] S. W. Grill, K. Kruse, and F. Jülicher. Theory of mitotic spindle oscillations. *Physical Review Letters*, 94(10):108104, 2005.
- [52] G. Grosjean, M. Hubert, G. Lagubeau, and N. Vandewalle. Realization of the najafi-golestanian microswimmer. *Physical Review E*, 94:021101, Aug 2016.
- [53] J. S. Guasto, K. A. Johnson, and J. P. Gollub. Oscillatory flows induced by microorganisms swimming in two dimensions. *Physical Review Letters*, 105(16):168102, 2010.
- [54] B. Guirao and J.-F. Joanny. Spontaneous creation of macroscopic flow and metachronal waves in an array of cilia. *Biophysical Journal*, 92(6):1900–1917, 2007.
- [55] J. Happel and H. Brenner. *Low Reynolds number hydrodynamics: with special applications to particulate media*, volume 1. Springer Science & Business Media, 2012.
- [56] A. Hilfinger, I. Riedel-Kruse, J. Howard, and F. Jülicher. How molecular motors shape the flagellar beat. *Biophysical Journal*, 96(3):196a, 2009.

- [57] A. C. Hindmarsh. Odepack, a systematized collection of ode solvers, rs stepleman et al.(eds.), north-holland, amsterdam,(vol. 1 of), pp. 55-64. *IMACS Transactions on Scientific Computation*, 1:55–64, 1983.
- [58] H. J. Hoops, R. L. Wright, J. W. Jarvik, and G. B. Witman. Flagellar waveform and rotational orientation in a chlamydomonas mutant lacking normal striated fibers. *The Journal of Cell Biology*, 98(3):818–824, 1984.
- [59] J. Howard et al. *Mechanics of motor proteins and the cytoskeleton*. Sinauer Associates Sunderland, MA, 2001.
- [60] J. Hu, M. Yang, G. Gompper, and R. G. Winkler. Modelling the mechanics and hydrodynamics of swimming e. coli. *Soft matter*, 11(40):7867–7876, 2015.
- [61] J. S. Hyams and G. G. Borisy. Isolated flagellar apparatus of chlamydomonas: characterization of forward swimming and alteration of waveform and reversal of motion by calcium ions in vitro. *Journal of Cell Science*, 33(1):235–253, 1978.
- [62] T. Ishikawa. Suspension biomechanics of swimming microbes. *Journal of The Royal Society Interface*, page rsif20090223, 2009.
- [63] B. Jewell and J. Ruegg. Oscillatory contraction of insect fibrillar muscle after glycerol extraction. *Proceedings of the Royal Society of London B: Biological Sciences*, 164(996):428–459, 1966.
- [64] J. F. Jikeli, L. Alvarez, B. M. Friedrich, L. G. Wilson, R. Pascal, R. Colin, M. Pichlo, A. Rennhack, C. Brenker, and U. B. Kaupp. Sperm navigation along helical paths in 3d chemoattractant landscapes. *Nature communications*, 6, 2015.
- [65] F. Jülicher and J. Prost. Spontaneous oscillations of collective molecular motors. *Physical Review Letters*, 78(23):4510, 1997.
- [66] A. Kaiser, K. Popowa, H. Wensink, and H. Löwen. Capturing self-propelled particles in a moving microwedge. *Physical Review E*, 88(2):022311, 2013.
- [67] R. Kamiya and G. B. Witman. Submicromolar levels of calcium control the balance of beating between the two flagella in demembrated models of chlamydomonas. *The Journal of Cell Biology*, 98(1):97–107, 1984.
- [68] Y. Katsu-Kimura, F. Nakaya, S. A. Baba, and Y. Mogami. Substantial energy expenditure for locomotion in ciliates verified by means of simultaneous measurement of oxygen consumption rate and swimming speed. *Journal of Experimental Biology*, 212(12):1819–1824, 2009.
- [69] T. Kiørboe, H. Jiang, R. J. Gonçalves, L. T. Nielsen, and N. Wadhwa. Flow disturbances generated by feeding and swimming zooplankton. *Proceedings of the National Academy of Sciences*, 111(32):11738–11743, 2014.
- [70] G. S. Klindt and B. M. Friedrich. Flagellar swimmers oscillate between pusher-and puller-type swimming. *Physical Review E*, 92(6):063019, 2015.

- [71] G. S. Klindt, C. Ruloff, C. Wagner, and B. M. Friedrich. Load response of the flagellar beat. *Physical Review Letters*, 117:258101, Dec 2016.
- [72] B. Kralemann, L. Cimponeriu, M. Rosenblum, A. Pikovsky, and R. Mrowka. Phase dynamics of coupled oscillators reconstructed from data. *Physical Review E*, 77(6):066205, 2008.
- [73] A. J. Ladd. Hydrodynamic transport coefficients of random dispersions of hard spheres. *The Journal of Chemical Physics*, 93(5):3484–3494, 1990.
- [74] L. Landau and E. Lifshitz. *Fluid mechanics: Landau and Lifshitz: course of theoretical physics*, volume 6. Elsevier, 2013.
- [75] E. Lauga, W. R. DiLuzio, G. M. Whitesides, and H. A. Stone. Swimming in circles: motion of bacteria near solid boundaries. *Biophysical Journal*, 90(2):400–412, 2006.
- [76] E. Lauga and T. R. Powers. The hydrodynamics of swimming microorganisms. *Reports on Progress in Physics*, 72(9):096601, 2009.
- [77] P. P. Lele, B. G. Hosu, and H. C. Berg. Dynamics of mechanosensing in the bacterial flagellar motor. *Proceedings of the National Academy of Sciences*, 110(29):11839–11844, 2013.
- [78] M. Leoni and T. B. Liverpool. Hydrodynamic synchronization of nonlinear oscillators at low reynolds number. *Physical Review E*, 85:040901, Apr 2012.
- [79] K. C. Leptos, J. S. Guasto, J. P. Gollub, A. I. Pesci, and R. E. Goldstein. Dynamics of enhanced tracer diffusion in suspensions of swimming eukaryotic microorganisms. *Physical Review Letters*, 103(19):198103, 2009.
- [80] K. C. Leptos, K. Y. Wan, M. Polin, I. Tuval, A. I. Pesci, and R. E. Goldstein. Antiphase synchronization in a flagellar-dominance mutant of chlamydomonas. *Physical Review Letters*, 111(15):158101, 2013.
- [81] G. Li and A. M. Ardekani. Collective motion of microorganisms in a viscoelastic fluid. *Physical Review Letters*, 117:118001, Sep 2016.
- [82] C. B. Lindemann. A “geometric clutch” hypothesis to explain oscillations of the axoneme of cilia and flagella. *Journal of Theoretical Biology*, 168(2):175–189, 1994.
- [83] Y. Liu. *Fast multipole boundary element method: theory and applications in engineering*. Cambridge university press, 2009.
- [84] E. Lushi. Stability and dynamics of anisotropically tumbling chemotactic swimmers. *Physical Review E*, 94:022414, Aug 2016.
- [85] R. Ma, G. S. Klindt, I. H. Riedel-Kruse, F. Jülicher, and B. M. Friedrich. Active phase and amplitude fluctuations of flagellar beating. *Physical Review Letters*, 113(4):048101, 2014.

- [86] K. Machin. Wave propagation along flagella. *Journal of Experimental Biology*, 35(4):796–806, 1958.
- [87] W. F. Marshall and S. Nonaka. Cilia: tuning in to the cell’s antenna. *Current Biology*, 16(15):R604–R614, 2006.
- [88] P. Martin, D. Bozovic, Y. Choe, and A. Hudspeth. Spontaneous oscillation by hair bundles of the bullfrog’s sacculus. *The Journal of Neuroscience*, 23(11):4533–4548, 2003.
- [89] G. McFadden, D. Schulze, B. Surek, J. L. Salisbury, and M. Melkonian. Basal body reorientation mediated by a ca^{2+} -modulated contractile protein. *The Journal of Cell Biology*, 105(2):903–912, 1987.
- [90] M. Merkel. personal communication.
- [91] M. Mussler, S. Rafai, P. Peyla, and C. Wagner. Effective viscosity of non-gravitactic *chlamydomonas reinhardtii* microswimmer suspensions. *Europhysics Letters*, 101(5):54004, 2013.
- [92] A. Najafi and R. Golestanian. Simple swimmer at low reynolds number: Three linked spheres. *Physical Review E*, 69(6):062901, 2004.
- [93] N. Naremsatsu, R. Quek, K.-H. Chiam, and Y. Iwadate. Ciliary metachronal wave propagation on the compliant surface of paramecium cells. *Cytoskeleton*, 72(12):633–646, 2015.
- [94] D. Nicastro, C. Schwartz, J. Pierson, R. Gaudette, M. E. Porter, and J. R. McIntosh. The molecular architecture of axonemes revealed by cryoelectron tomography. *Science*, 313(5789):944–948, 2006.
- [95] T. Niedermayer, B. Eckhardt, and P. Lenz. Synchronization, phase locking, and metachronal wave formation in ciliary chains. *Chaos*, 18(3):037128, 2008.
- [96] C. K. Omoto and C. Kung. The pair of central tubules rotates during ciliary beat in paramecium. *Nature*, 279(5713):532–534, 1979.
- [97] N. Osterman and A. Vilfan. Finding the ciliary beating pattern with optimal efficiency. *Proceedings of the National Academy of Sciences*, 108(38):15727–15732, 2011.
- [98] F. Perrin. Mouvement brownien d un ellipsoide (1). *Dispersion dielectrique*, 1934.
- [99] M. Polin, I. Tuval, K. Drescher, J. P. Gollub, and R. E. Goldstein. *Chlamydomonas* swims with two gears in a eukaryotic version of run-and-tumble locomotion. *Science*, 325(5939):487–490, 2009.
- [100] K. Polotzek and B. M. Friedrich. A three-sphere swimmer for flagellar synchronization. *New Journal of Physics*, 15(4):045005, 2013.

- [101] E. M. Purcell. Life at low reynolds number. *American Journal of Physics*, 45(1):3–11, 1977.
- [102] J. Purkinje. Ueber flimmerbewegungen im gehirn. *Archiv fr Anatomie, Physiologie und wissenschaftliche Medizin*, 289, 1836.
- [103] T. Qiu, T.-C. Lee, A. G. Mark, K. I. Morozov, R. Münster, O. Mierka, S. Turek, A. M. Leshansky, and P. Fischer. Swimming by reciprocal motion at low reynolds number. *Nature communications*, 5, 2014.
- [104] G. Quaranta, M.-E. Aubin-Tam, and D. Tam. Hydrodynamics versus intracellular coupling in the synchronization of eukaryotic flagella. *Physical Review Letters*, 115(23):238101, 2015.
- [105] S. Rafai, L. Jibuti, and P. Peyla. Effective viscosity of microswimmer suspensions. *Physical Review Letters*, 104(9):098102, 2010.
- [106] I. Reiten, F. E. Uslu, S. Fore, R. Pelgrims, C. Ringers, C. D. Verdugo, M. Hoffman, P. Lal, K. Kawakami, K. Pekkan, et al. Motile-cilia-mediated flow improves sensitivity and temporal resolution of olfactory computations. *Current Biology*, 2016.
- [107] I. H. Riedel, K. Kruse, and J. Howard. A self-organized vortex array of hydrodynamically entrained sperm cells. *Science*, 309(5732):300–303, 2005.
- [108] I. H. Riedel-Kruse, A. Hilfinger, J. Howard, and F. Jülicher. How molecular motors shape the flagellar beat. *Human Frontier Science Program Journal*, 1(3):192–208, 2007.
- [109] D. L. Ringo. Flagellar motion and fine structure of the flagellar apparatus in chlamydomonas. *The Journal of Cell Biology*, 33(3):543–571, 1967.
- [110] Rothschild. Measurement of sperm activity before artificial insemination, 1949.
- [111] U. Ruffer and W. Nultsch. High-speed cinematographic analysis of the movement of chlamydomonas. *Cell Motility*, 5(3):251–263, 1985.
- [112] D. Saintillan. Extensional rheology of active suspensions. *Physical Review E*, 81(5):056307, 2010.
- [113] J. L. Salisbury and G. L. Floyd. Calcium-induced contraction of the rhizoplast of a quadriflagellate green alga. *Science*, 202(4371):975–977, 1978.
- [114] J. L. Salisbury, M. Sanders, and L. Harpst. Flagellar root contraction and nuclear movement during flagellar regeneration in chlamydomonas reinhardtii. *The Journal of Cell Biology*, 105(4):1799–1805, 1987.
- [115] M. Sanderson and M. Sleight. Ciliary activity of cultured rabbit tracheal epithelium: beat pattern and metachrony. *Journal of Cell Science*, 47(1):331–347, 1981.

-
- [116] P. Sartori. *Effect of curvature and normal forces on motor regulation of cilia*. PhD thesis, Citeseer, 2015.
- [117] P. Sartori, V. F. Geyer, A. Scholich, F. Jülicher, and J. Howard. Dynamic curvature regulation accounts for the symmetric and asymmetric beats of chlamydomonas flagella. *eLife*, 5:e13258, 2016.
- [118] R. Schmitz. Force multipole moments for a spherically symmetric particle in solution. *Physica A: Statistical Mechanics and its Applications*, 102(1):161–178, 1980.
- [119] D. Schulze, H. Robenek, G. I. McFadden, and M. Melkonian. Immunolocalization of a ca^{2+} -modulated contractile protein in the flagellar apparatus of green algae: the nucleus-basal body connector. *European Journal of Cell Biology*, 45(1):51–61, 1987.
- [120] J. W. Shaevitz, J. Y. Lee, and D. A. Fletcher. Spiroplasma swim by a processive change in body helicity. *Cell*, 122(6):941–945, 2005.
- [121] A. Shapere and F. Wilczek. Self-propulsion at low reynolds number. *Physical Review Letters*, 58(20):2051, 1987.
- [122] D. Smith, J. Blake, and E. Gaffney. Fluid mechanics of nodal flow due to embryonic primary cilia. *Journal of The Royal Society Interface*, 5(22):567–573, 2008.
- [123] D. Smith, E. Gaffney, and J. Blake. Modelling mucociliary clearance. *Respiratory Physiology & Neurobiology*, 163(1):178–188, 2008.
- [124] D. Smith, E. Gaffney, J. Blake, and J. Kirkman-Brown. Human sperm accumulation near surfaces: a simulation study. *Journal of Fluid Mechanics*, 621:289–320, 2009.
- [125] K. E. Summers and I. Gibbons. Adenosine triphosphate-induced sliding of tubules in trypsin-treated flagella of sea-urchin sperm. *Proceedings of the National Academy of Sciences*, 68(12):3092–3096, 1971.
- [126] B. E. Taillon, S. A. Adler, J. P. Suhan, and J. W. Jarvik. Mutational analysis of centrin: an ef-hand protein associated with three distinct contractile fibers in the basal body apparatus of chlamydomonas. *The Journal of Cell Biology*, 119(6):1613–1624, 1992.
- [127] G. Taylor. Analysis of the swimming of long and narrow animals. In *Proceedings of the Royal Society of London A: Mathematical, Physical and Engineering Sciences*, volume 214, pages 158–183. The Royal Society, 1952.
- [128] M. Theers and R. G. Winkler. Synchronization of rigid microrotors by time-dependent hydrodynamic interactions. *Physical Review E*, 88(2):023012, 2013.
- [129] M. J. Tipping, N. J. Delalez, R. Lim, R. M. Berry, and J. P. Armitage. Load-dependent assembly of the bacterial flagellar motor. *MBio*, 4(4):e00551–13, 2013.

- [130] N. Uchida and R. Golestanian. Generic conditions for hydrodynamic synchronization. *Physical Review Letters*, 106(5):058104, 2011.
- [131] A. Vilfan and F. Jülicher. Hydrodynamic flow patterns and synchronization of beating cilia. *Physical Review Letters*, 96(5):058102, 2006.
- [132] K. Y. Wan and R. E. Goldstein. Coordinated beating of algal flagella is mediated by basal coupling. *Proceedings of the National Academy of Sciences*, 113(20):E2784–E2793, 2016.
- [133] K. Y. Wan, K. C. Leptos, and R. E. Goldstein. Lag, lock, sync, slip: the many phases of coupled flagella. *Journal of the Royal Society Interface*, 11(94):20131160, 2014.
- [134] S. Werner, J. C. Rink, I. H. Riedel-Kruse, and B. M. Friedrich. Shape mode analysis exposes movement patterns in biology: Flagella and flatworms as case studies. *PloS one*, 9(11):e113083, 2014.
- [135] R. L. Wright, S. A. Adler, J. G. Spanier, and J. W. Jarvik. Nucleus-basal body connector in chlamydomonas: Evidence for a role in basal body segregation and against essential roles in mitosis or in determining cell polarity. *Cell motility and the Cytoskeleton*, 14(4):516–526, 1989.
- [136] R. L. Wright, B. Chojnacki, and J. W. Jarvik. Abnormal basal-body number, location, and orientation in a striated fiber-defective mutant of chlamydomonas reinhardtii. *The Journal of Cell Biology*, 96(6):1697–1707, 1983.
- [137] T. Yagi and R. Kamiya. Vigorous beating of chlamydomonas axonemes lacking central pair/radial spoke structures in the presence of salts and organic compounds. *Cell Motility and the Cytoskeleton*, 46(3):190–199, 2000.
- [138] Y. Yang, J. Elgeti, and G. Gompper. Cooperation of sperm in two dimensions: synchronization, attraction, and aggregation through hydrodynamic interactions. *Physical Review E*, 78(6):061903, 2008.
- [139] A. Zemel, F. Rehfeldt, A. Brown, D. Discher, and S. Safran. Optimal matrix rigidity for stress-fibre polarization in stem cells. *Nature physics*, 6(6):468–473, 2010.
- [140] A. Zöttl and H. Stark. Hydrodynamics determines collective motion and phase behavior of active colloids in quasi-two-dimensional confinement. *Physical Review Letters*, 112(11):118101, 2014.

Versicherung

Hiermit versichere ich, dass ich die vorliegende Arbeit ohne unzulässige Hilfe Dritter und ohne Benutzung anderer als der angegebenen Hilfsmittel angefertigt habe; die aus fremden Quellen direkt oder indirekt übernommenen Gedanken sind als solche kenntlich gemacht.

Arbeit wurde bisher weder im Inland noch im Ausland in gleicher oder ähnlicher Form einer anderen Prüfungsbehörde vorgelegt.

Die Arbeit wurde am Max-Planck-Institut für Physik komplexer Systeme angefertigt und von Prof. Frank Jülicher und Dr. Benjamin M. Friedrich betreut.

Ich erkenne die Promotionsordnung der Fakultät Mathematik und Naturwissenschaften der Technischen Universität Dresden an.

Gary Steven Klindt